Investigation of Electroplating 4D Printed Antenna & Developing 3D Printed Lithium Batteries

by

Muneer I. Barnawi

Submitted in Partial Fulfillment of the Requirements

for the Degree of

Master of Science in Engineering

in the

Chemical Engineering

Program

YOUNGSTOWN STATE UNIVERSITY

May 2022

Investigating Electroplating of 3D Printed Antenna & Developing 3D printed Lithium Batteries

Muneer I. Barnawi

I hereby release this thesis to the public. I understand that this thesis will be made available from the OhioLINK ETD Center and the Maag Library Circulation Desk for public access. I also authorize the University or other individuals to make copies of this thesis as needed for scholarly research.

Signature:

_____

Muneer I Barnawi, Student Date

Approvals:

_____

Dr. Pedro Cortes, Thesis Advisor Date

_____

Dr., *Vamsi Borra* Committee Member Date

_____

Dr. Frank X. Li, Committee Member Date

_____

Dr. Salvatore A. Sanders, Dean of Graduate Studies Date

Abstract

Additive manufacturing (AM) commonly referred to as 3D printing is a method of manufacturing three-dimensional parts in a layer-by-layer fashion. Common materials used in this process are polymers, metals, and ceramics. Nowadays, AM is utilized for more than just traditional structures - it is used to fabricate and create nontraditional designs. Additive manufacturing is associated with various industrial manufacturing processes and innovations including maintenance, repairs, and product design. Among the different applications of this process, the production of 3D printed morphing systems and parts for batteries represents an attractive approach for yielding high-performance structures. Non-metallic morphing components are commonly constituted by shape memory polymers (SMPs), which are actuating materials that can respond to thermal, electrical, or chemical stimuli. Here, SMPs were constructed by incorporating two different blends of photopolymer resins in a Vat Photopolymerization process. The printed SMPs were subsequently electroplated with copper to yield a conductive morphing structure for applications such as sensors, actuating systems, and functional antennas. The present work investigated the adaptability and functionality of the copper-plated 3D printed parts as morphing antennas capable of providing a multi-radio frequency. Additionally, this research program investigated the production and performance of 3D printed LiFePO4 parts via Vat Photo Polymerization to be used as electrodes on additively manufactured energy storage devices. This effort represents a novel approach to further expanding the production of customized batteries.

Acknowledgments

I am extremely grateful and appreciative to the following people who have helped me through this journey.

Thesis advisor for golden opportunity to do these amazing projects

Dr. Pedro Cortes

Committee Members

Dr. Frank X. Li and Dr. Vamsi Borra

Faculties

Dr. Douglas M Price, Holly J. Martin, Dr, Jeanette M Garr, and Byung- Wook Park

Additional Assistance

Electrical Engineering Lab-3100, Material Science Lab 1490, and CMC

Special Thanks

To my parents for their support, my brother, and sisters for being by my side all these times making silly decisions, and my great friends for believing in me and supporting my goals.

Table of Contents

List of Figure

List of Tables

Nomenclature

AM	Additive Manufacturing
ASTM	American Society for Testing and Materials
CNT	Carbon Nanotube
CFR	Carbon Fiber Reinforced
DLP	Digital Light Processing
DMA	Dynamic Mechanical Analysis
DSC	Differential Scanning Calorimetry
EDS	Energy Dispersive X-ray Spectroscopy
FFF	Fused Filament Fabrication
HFSS	High-Frequency Simulation Software
IPA	Isopropyl Alcohol
ISO	International Organization for Standardization
LED	Light Emitting Diode
PE	Polyethylene
SEM	Scanning Electron Microscope
SLA	Stereolithography
SLS	Selective Laser Sintering
SMA	Sub-Miniature Version A

SMP Shape Memory Polymer

SPCs Shape Memory Composites

SRC Shape Recovery Cycle

Tg Glass Transition Temperature

UV Ultraviolet

VNA Virtual Network Analyzer

XRD X-ray Diffraction

1 Introduction

Smart materials are also called intelligent materials and are designed to respond to external stimuli like light, magnetic field, electrical current, mechanical stress, moisture,

and chemical signal [1]. Those features position smart materials to play a leading role in scientific applications including solving engineering problems with high efficiency and providing a new opportunity to create customizable products [2]. For example, smart materials have been studied for suppressing the vibration of aircraft rotor blades via shape changes [3].

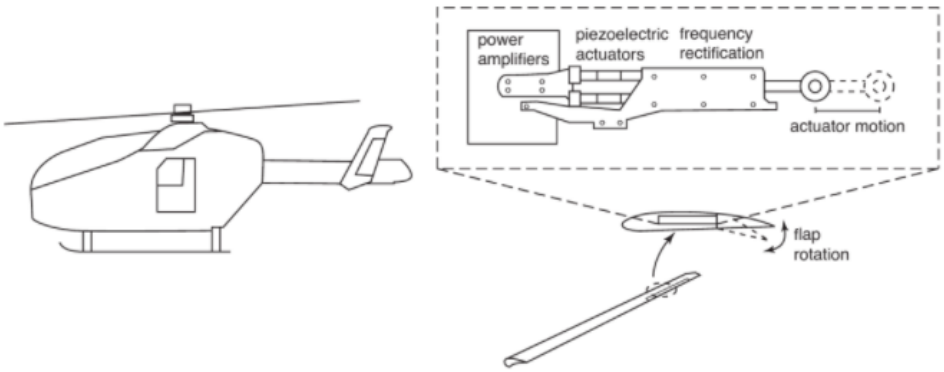

Figure 1: Active rotors blades concepts [3]

1.1 Shape Memory Polymer

A Shape Memory Polymer (SMP) is a smart material that can change its structure by responding to an external thermal or electrical stimulus. SMPs possess the ability to return from a deformed state to the original shape. Shape memory polymers can offer space and weight savings compared to common traditional materials [4,5]. The smart behavior and structure allow SMPs to be involved in significant science and engineering applications such as actuators, Micro Electro Mechanical Systems (MEMSs), active and passive controls, self-repair (healing), space systems, intelligent medical devices, and automobiles[6].

One attractive application for SMPs is in the electronics field. Shape memory polymers carry noteworthy features such as morphological behavior and adaptive architecture which makes SMPs a favorable material in the electronic industry. 3D printed shape memory polymers are composed of photo-initiators, methacrylate semi-crystalline,

and inhibitors. The fabricated SMPs were printed by an inkjet printer, and a silver nanoparticle ink was subsequently added to the surface of the polymer to act as the electrical interconnection [7]. Following a thermal activation, the designed and the printed circuit closed allowing an electrical connection to be taken place across the system and lighting an LED (see figures 1-1).

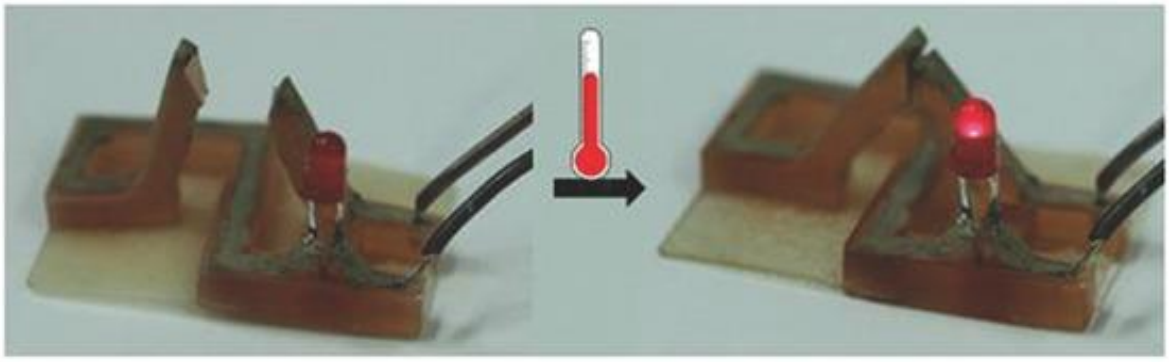

Figure 1-1: Heat-activated 3D Printed shape memory polymer [7].

An interesting application of SMP is in the robotic industries where shape memory foams are utilized to provide initial soft pretension in gripping. The shape of memory foams can harden by cooling, making an adaptive grip. Starting at this, the materials have been widespread usage, for example, sport wears as helmets and the building industry as foam with heat to seal window frames [8,9]. In the same field and application, shape-memory is used in McKibben artificial muscle to drive robotic joints. A McKibben actuator can function as a device moving only in two states; un-actuated and actuated. The transition between the two states is managed by air pressure. By developing the device and introducing the shape memory polymers, temperature control was introduced which could be an additional control mechanism. The two-parameter (temperature and pressure) means the actuator can exhibit more states. Figure (1-2) shows five states transitions for the SMP Mckibben artificial muscle {S1, …… S5}. It can be observed, that by controlling the temperature and the pressure the actuator can be transitioned from state S1 to S4 [10].

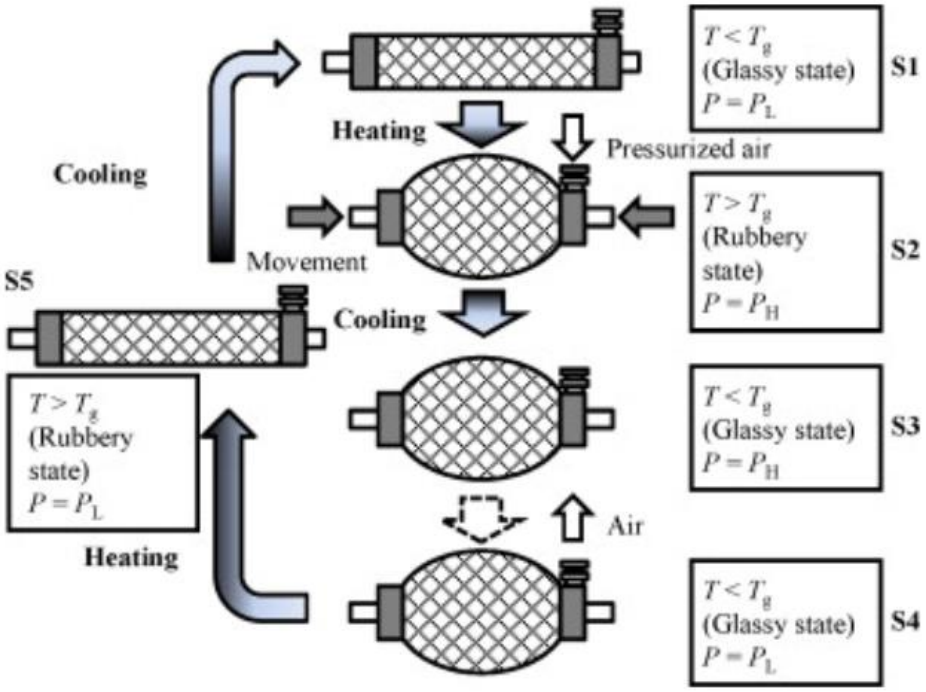

Figure 1-2: Schematic representation of McKibben artificial muscle that uses SMP [10]

1.2 Shape Memory Polymer Composites (SMPCs)

Shape memory polymers are composites of more than one material with unique chemical, mechanical, thermal, and physical properties; those materials are merged to create a material with properties unlike the individual elements [11]. A major attempt to create smart composites has been led by the aerospace industry as a light actuator, and structural parts [12]. A prototype of a self-deployable structure made of carbon-fiber-reinforced (CFR) based SMP is shown in figures 1-3 [13].

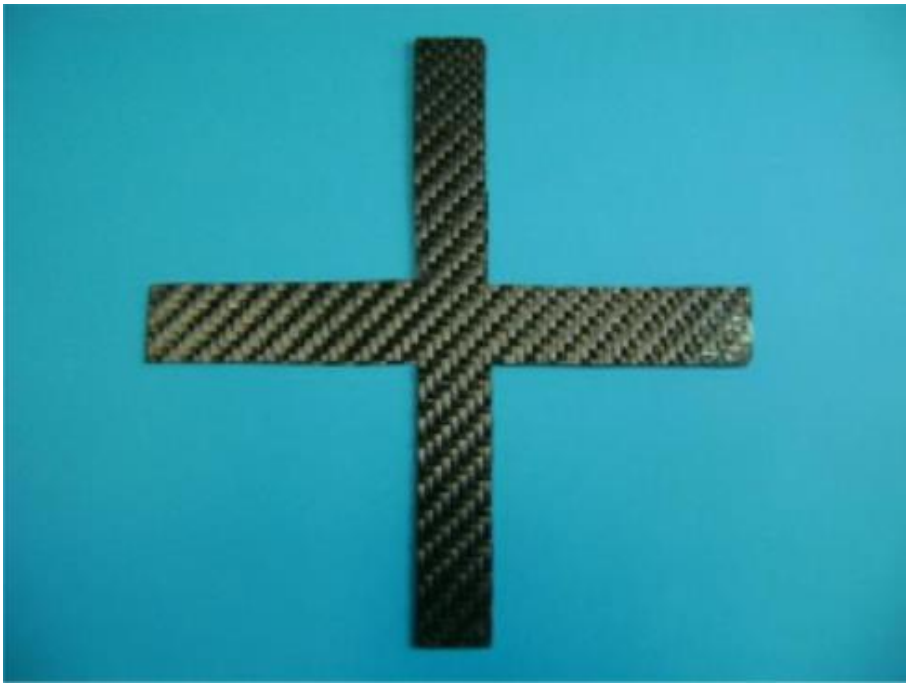

Figure 1-3: Prototype of deployable carbon fiber reinforced SMP. reinforced [13].

A composite system with high recovery and fixity capabilities can be utilized in the biomedical field. Various cardiac occlude devices are designed with composite materials that can be biodegradable, customized, programmed, and controlled by different stimuli [14].

1.3 Metalizing 3D printed Parts

Polymer metallization is an advanced step to make polymers conducive to fabricating electrically functional components. Various remarkable works have focused on the integration of conductive metals and 3D-printed polymers. One approach that has been widely examined to produce 3D printing of conductive polymers is the addition of carbon nanotubes (CNTs) to a polymer blend [15–17]. However, the approach of mixing CNTs and polymer results in poor conductance. The performance of the CNTs and polymer composites results in a variable value of electrical conductivity ranging from 1.6×10^{-2} to 81 S/m [18].

Another approach to fabricating conductive 3D printed polymers is via conductive metal deposition onto the surface. The electroless technique has been investigated by multiple researchers. The deposition of copper into the surface of the part creates a thin layer of metal ions [19,20]. An interesting result accomplished by Lee et al [21] showed that the incorporation of metal electrodeposition onto the surface of a polymer part resulted in a high conductivity value of 3.8×10^5 S/cm. A similar approach was performed by using electroplating bath techniques to deposit copper onto the surface of the 3D printed parts. This technique is a process of adding a metal layer and it is used in Jewelry and electronic manufacturing, where the electrical current applied between the two electrodes - anode and cathode - is in contact with a liquid electrolyte bath. To accommodate the electroplating process, the surface of the 3D printed polymer must first be modified by inducing a semi-conductive state by adding or coating it with some form of conductive ink on the surface. The addition of a semi-conductive filament followed by an electroplating copper process was investigated by Angel et al [22].

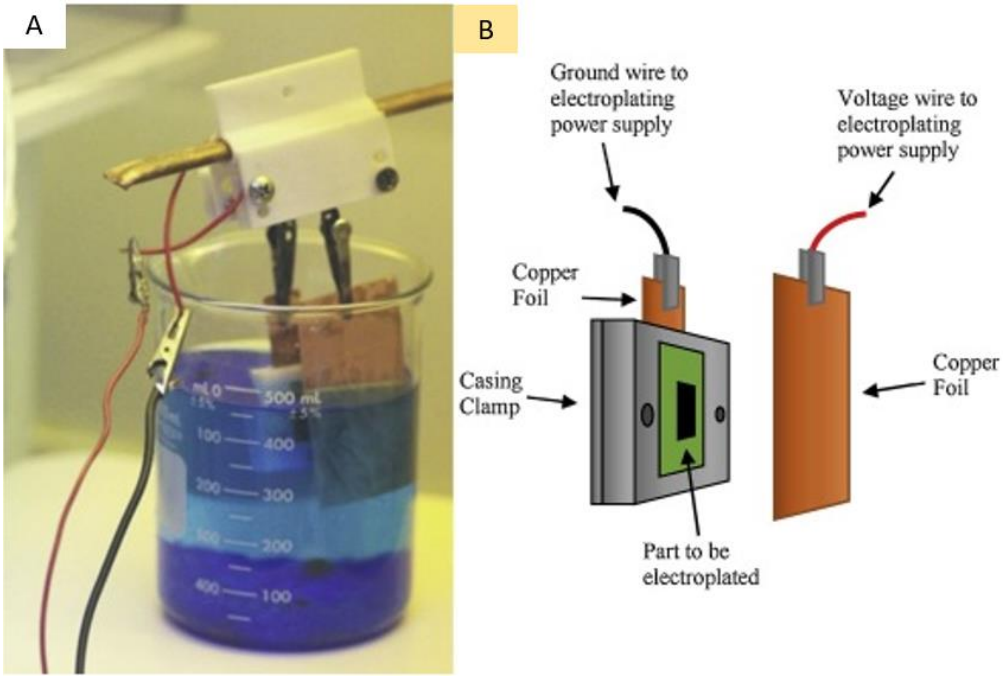

Figure 1-4: Standard copper sulfate bath: (a) group for fabrication of microscale inductors used for copper-plating (b)[22].

1.3.1 Application of Metalized 3D printed Parts/Shape Memory Polymer

The development of electrically conductive 3D shape-memory structures based on an electrodeposition process allows the production of devices with morphological and complex geometries that can have applications in the biomedical and aerospace field. As mentioned before, one main area of interest for shape-memory materials is the electrical industry [23]. Figure 1.6 shows metalized 3D printed parts, which were developed to act as functional sensing microdevices in the field of MEMS [19].

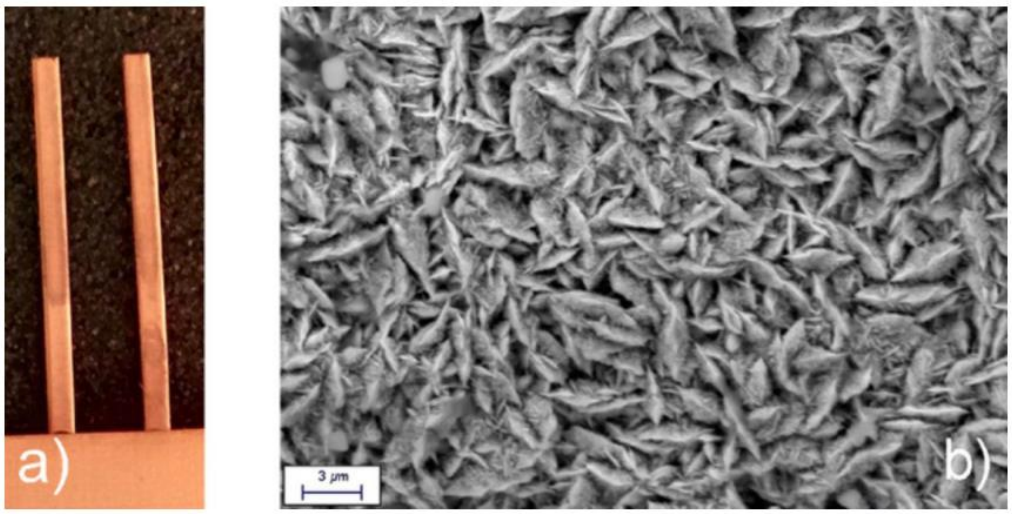

Figure 1-5: (a)Visual appearance of two Cu-coated cantilevers (b) SEM microphotography of the Co as plated (1000 X magnification)[19].

1.4 Lithium-Ion Battery

The demand for high-performance rechargeable batteries attracted significant attention to power energy as an energy storage device for the growing market of electrical vehicles, portable electronics, and grid-level management systems [24]. The interesting rechargeable power led to an extensive increase in the rresearchfiled regarding lithium-ion batteries (LIB). In addition to that governments around the globe are now more conscious about creating green energy storage technologies such as solar and wind. Figure (1-6) shows that research into batteries had significantly increased from 2010 to 2017 exceeding the percentage rate of increase of overall world publication to 260% growth, equivalent to 119 188 new publications (based on the search query on the Web of Science online database) [25].

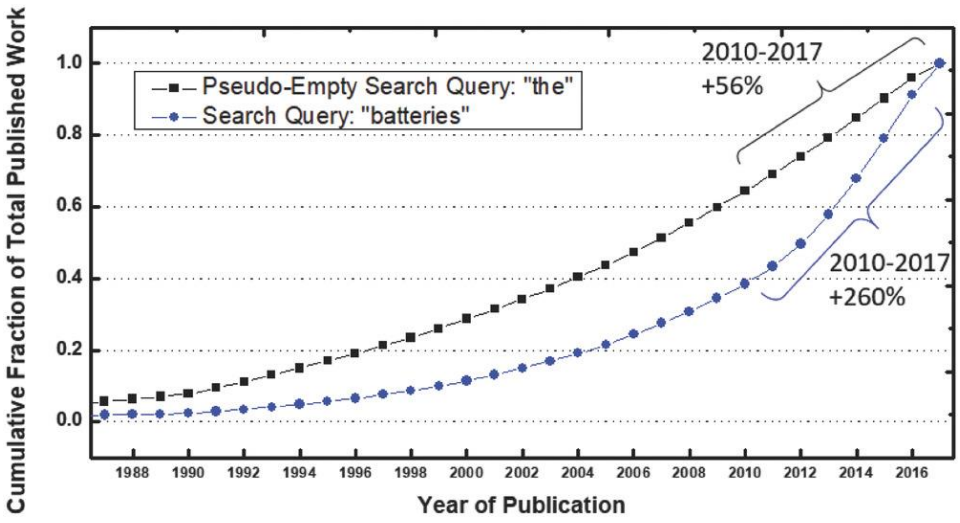

Figure 1-6: Comparison of literature growth from 1987 to 2017 between search query "batteries" (blue circles) and pseudo-empty search query "the" (black squares) in the field of search "topic," utilizing the website Web of Science accessed [25].

The main structural component of a rechargeable battery includes two electrodes with different electrochemical potentials that present as anode and cathode, a separator to prevent electrical shorting between electrodes, and an electrolyte that transfer the ion between the electrodes resulting in the charge and discharge of the ionic batteries see figure (1-7) demonstrate the component of the Li-ion battery [24,26].

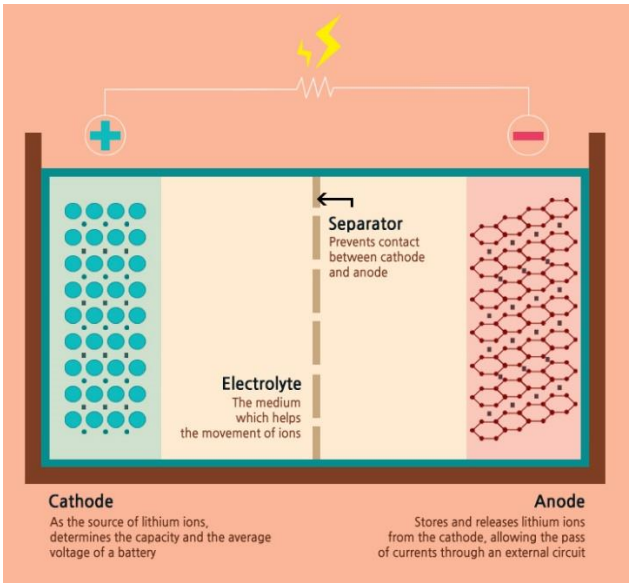

Figure 1-7: The four components of the Lithium-Ion Battery[26]

1.5 Application of lithium Battery.

The availability of lithium-ion batteries in various sizes and shapes with high energy density and low self-discharge trended them to be a perfect option for power supplies. In addition, lithium-ion batteries offer a wide spectrum of power solutions from portable energy solutions to energy storage solutions. Due to their electrochemical storage feature, lithium-ion batteries are commonly used in many applications. For instance, as emergency power backup for computers, phones, and medical technology, where they provide immediate power sources. Additionally, lithium-ion battery is used in electrical vehicles, where vehicles are fully dependent on rechargeable ion battery cell, limiting the need for oil resources[27,28].

Figure 1-8: demonstration of lithium-ion battery in electric vehicle [29]

The advantages of rechargeable Li-ion batteries offer over nickel-based systems including high specific energy, energy density, and lower power system life cycle cost, make Li-ion a favorable option for NASA space missions. NASA and the US Air Force recognize the advanced benefit of Li-ion technology to be part of their future aerospace

systems. NASA plans to utilize Li-ion batteries in future applications such as the planetary lander low earth orbit and planetary orbiters. Mars 2003 lander and Mars Microsats incorporate Li-ion batteries as baseline [30,31]. The main feature that these missions need for batteries to accomplish is to operate at sub-zero temperature (down to -30°C) at a stable charge/discharge rate.

Figure 1-9: Prototypes of Li-ion cells fabricated under NASA–DoD consortium [30]

1.6 Motivation for Thesis

Advanced methods of constructing material utilizing 3D printing or additive manufacturing have been developing rapidly. 3D printing shows the potential as an effective technique. Additive manufacturing shows multiple advantages over traditional manufacturing, particularly in fabricating complex geometries, reducing cost, and allowing for incorporating a diversity of materials. Unlike common materials, shape memory

polymer experiences non-static material properties that are used for actuation and sensing applications in various industries. Metalizing 3D printed parts, specifically shape memory polymer, will enormously expand the electrical applications of shape memory as sensing and functional systems. Similarly, the study of additive manufacturing for producing battery parts using Vat Photopolymerization represents an approach that can be expanded into the production of conformable and high-performance energy device systems.

1.7 Objectives

This research has investigated the metalizing process of 3D printed shape memory polymers via electroplating techniques for fabricating morphological functional antennas. Chemical and electrical characterization analyses were applied to examine the copper quality. Additionally, this work has studied the creation and performance of 3D printed lithium iron phosphates electrodes for additively manufactured batteries utilizing a Vat Photo Polymerization technique.

The specific goals of this research work are:

- Metalizing 3D printed shape memory polymers via electroplating techniques.
- Selectivity metalizing designed traces in 3D printed shape memory polymers.
- Production of lithium battery electrode parts using vat photopolymerization.
- Electrochemical and physical characterization of the 3D printed parts.

1.8 Organization

This thesis will be presented in the following order:

1. Chapter 1. The present chapter addresses a brief review of shape memory polymers and their properties, and applications in shape memory polymers for sensors, actuating structures, and functional antennas. It also provides an overview of 3D-printed lithium batteries.
2. Chapter 2: Presents the background of shape memory polymers, electroplating, additive manufacturing techniques, and 3D printed LiFePO4 batteries.

3. Chapter 3: Presents the experimental setup followed in this work.
4. Chapter 4: Discusses the results obtained in this research program
5. Chapter 5: Addressed the conclusions drawn in this study.

2.0 Literature Review

Additive manufacturing has shown Progress on the production of complex geometries for various scientific and engineering applications. This chapter addresses the background of 3D printed shape memory polymers and their mechanical and thermal properties, their 3D printing techniques, and their applications. Similarly, this chapter discusses the foundations of electroplating to induce a conductive phase on insulative materials. Furthermore, this literature review discusses the production of lithium iron phosphate via 3D printing, as well as the sintering techniques, and characterization

2.1 Shape Memory Polymer

Shape memory polymers were initially investigated in 1941 by Vernon [32]. However, the importance of SMPs was not fully known until the 1960s, when crosslinking polyethylene (PE) was used to create a heat-shrinkable responsive film and tubes. In the 80s, further investigation on shape memory polymers resulted in an improvement in their high recovery deformation features and shape fixity properties. Unlike shape memory alloys, the effect of shape memory polymers is not developed by heat but also by light, and chemistry[33].

Shape memory polymers are a class of smart materials that exhibit adaptive configurational features following thermo-mechanical activations. SMPs are commonly manufactured on their permanent shape and following an activation step, their shape can be modified into a temporary configuration. This temporary

configuration can be fixed if the system is allowed to be under its Tg while keeping a mechanical constrain. After the shape memory polymer is thermally heated above the transition temperature, it will return to the original shape if mechanical constraints are not applied [34]. Figure 2.1 displays the shape memory effect mechanism of SMP following a thermo-mechanical cycle.

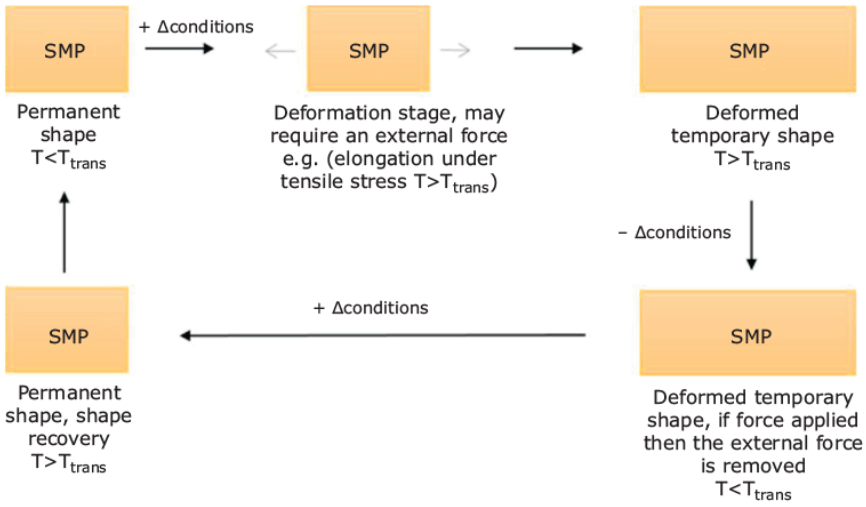

Figure 2-1: General SME mechanism of SMPs [32].

Shape memory polymers are of great interest in various industries, for instance, biomedical aerospace, and microelectronics. Indeed, shape memory polymers have attracted considerable attention in the medical field by developing the Trellix Embolic Coil which includes a shape memory polymer porous embolic scaffold, that provides significant advantages in peripheral vascular embolization and neurovascular conditions[35].

2.2 Shape Memory Properties

Shape memory effects of SMPs can be triggered by multiple stimuli such as light, electricity, pH, magnetism, and humidity. The most common stimulus is the thermal-induced activation, where above its Tg, the SMP displays a glassy-rubbery change which allows for its deformation into a temporary shape. In constant, the

recovery of its permanent shape from the temporary state seems to be attributed to an entropy mechanism[36] See figure 2-2. The SME of SMPS seems to be strongly related to its crosslinking mechanism[37]. For instance, an SMP network was achieved by crosslinking a polydimethylsiloxane (PDMS) polymer with dense carboxylate groups (100 mol %) (PDMS-COOH) with a small quantity of poly (ethylene glycol) diglycidyl ether (PEGDGE) [38]. The developed SMP(PDMS-COOH) exhibited a morphological and actuating behavior at 37°C with a shape memory recovery ratio of 98.06%.

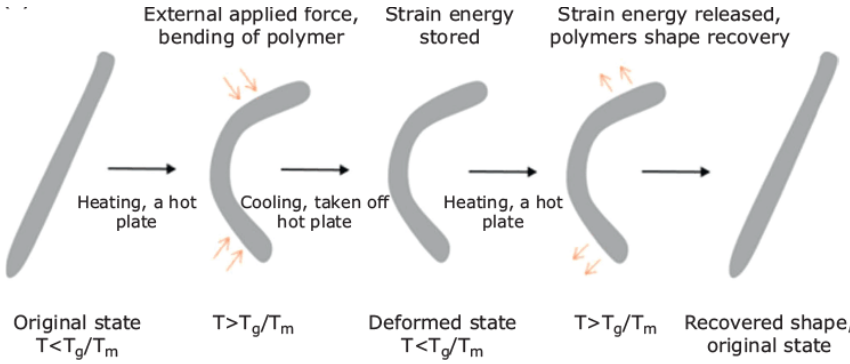

Figure 2-2: Schematic of thermally- responsive SMP [32]

Another effective stimulus applied to SMPs is the light-induced shape memory effect. A light-activated process utilizes photochemical (photo-crosslinking) or photothermal triggers. The light-activated SMPs use photo absorber particles that convert light to heat, and as a result, the temperature will increase in the SMPs. It is possible to manage the response of SMPs by adding conductive material to increase the thermal conductivity [39]. It is also possible to produce multi-stimuli-responsive SMPs by adding material that actuates to different wavelengths of light [40]. Figure 2-3 shows a light-activated SMP.

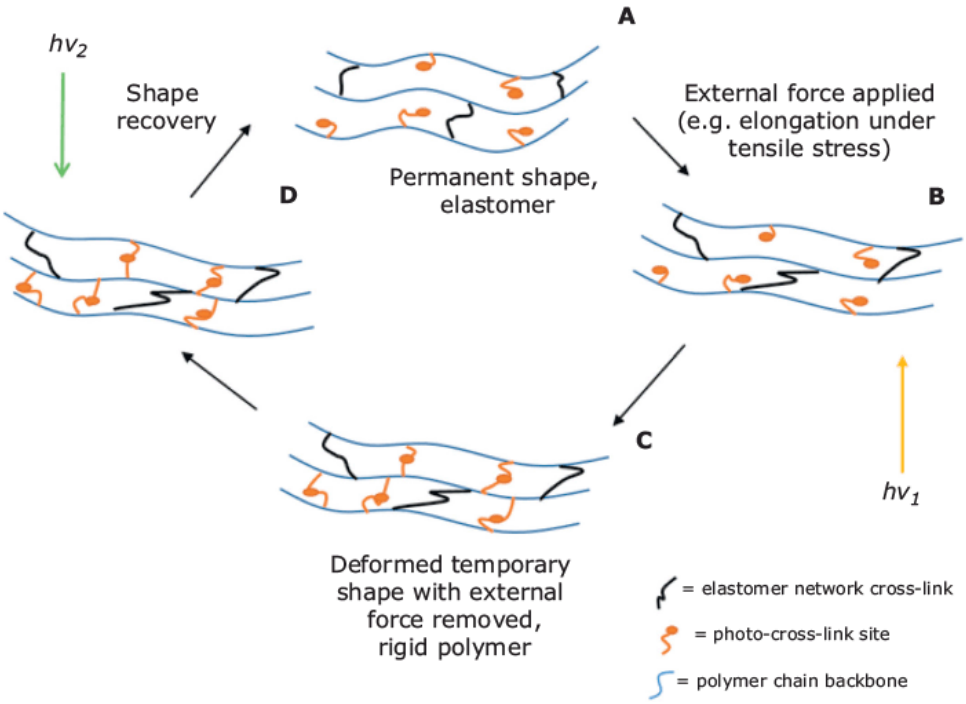

Figure 2-3: A schematics of the SME of SMP stimulated by light [32].

An interesting stimulated polymer is an electrically-induced shape memory polymer. Various electrically conductive materials have been incorporated such as carbon nanotubes (CNTs) [41], silver nanowires, metals, and Fe3O4 nanoparticles [42,43]. The incorporation of shape memory polyurethane (SMPU) and Ag nanowires NWs in bilayer structure has shown electrical conductivity and flexibility. The Ag NWs are distributed on the top surface of the polyurethane, forming a conductive percolating network layer (200Ω sq^{-1}) after a 12% stretching [44]. However, the material loses electrical conductivity because of an increase in elongation. When the material is both permanent or temporary and connected to the circuit, the voltage of 1.5 V has been applied to activate a LED (Light-emitting diode) [45].

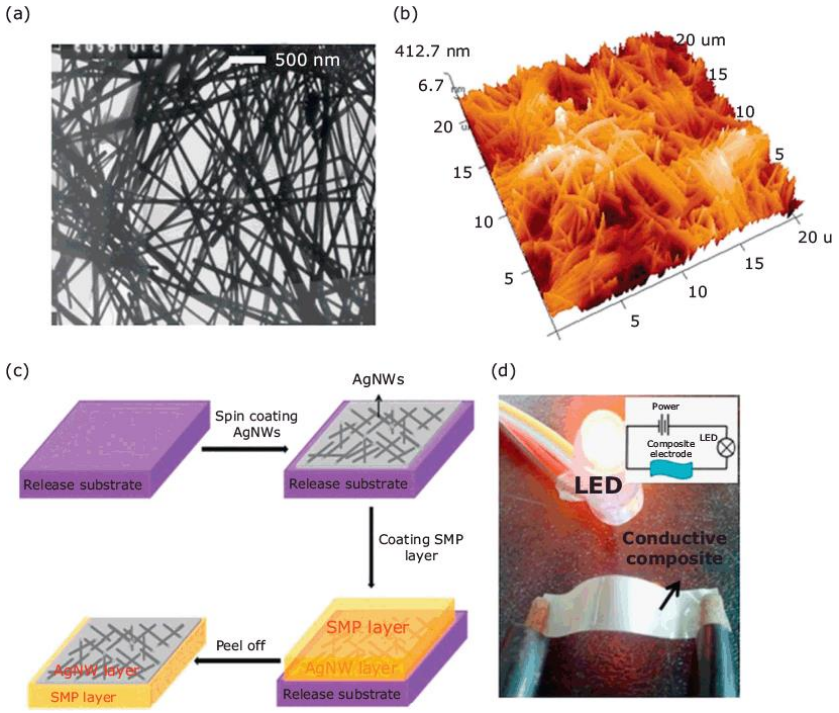

Figure 2-3: Inclusion of metallic phases to produce conductive SMP system (a) Transmission electron microscopy (TEM) image of Ag NWs, (b) atomic force microscopy (AFM) image of Ag NWs, (c) schematic illustration of the composites fabrication process, and (d) the LED turned on as voltages were applied to the composite (the inset shows the circuit connecting with the composites) [44].

2.2.1 Mechanical Properties

SMPs are multi stimulus controlled smart materials, which have potential features for use as a morphological application. SMPs experience large strain in their deformation steps, resisting aerodynamic loads in the glassy state. SMPs undergoes both brittle and rubbery state during morphological transition. Pure SMPs were prepared for the stress versus strain test at seven selected temperatures. It has been shown that by increasing the temperature the strength decreases considerably (see figure 2-4). In contrast, its strain at failure increases several orders of magnitude.

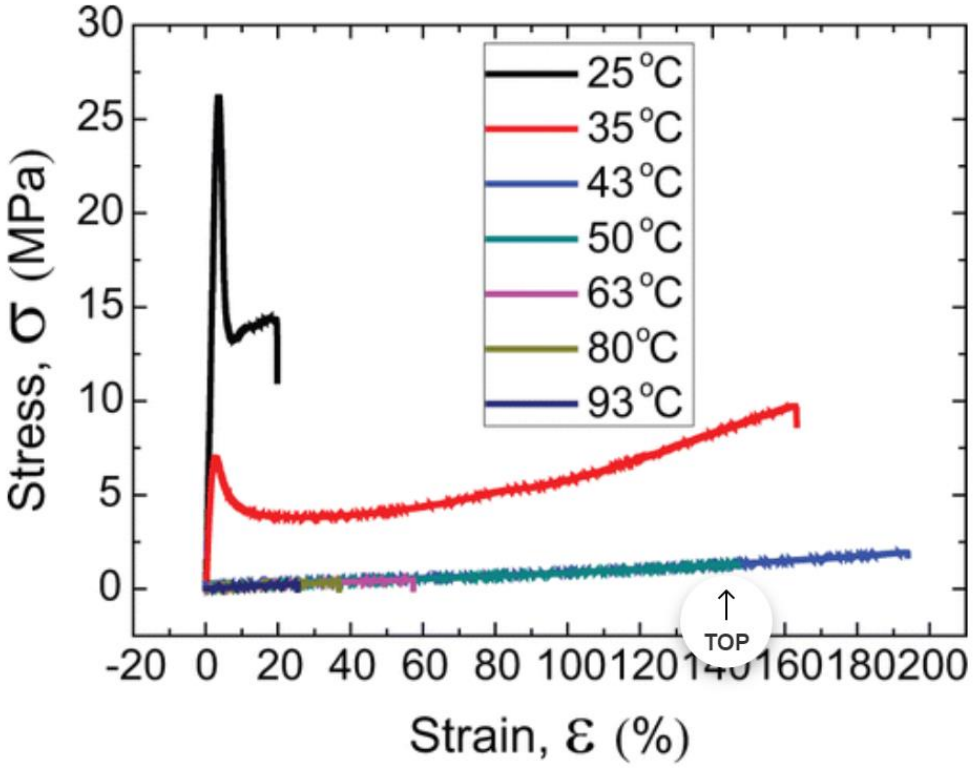

Figure 2-4: the stress-strain curve of pure SMPs at different temperatures[46]

Therefore, during the transition between temporary and permanent states, they tear along micro-crack created by tension. Due to these disadvantages, SMPs could experience some failures during the operation. To fix and enhance this disadvantage an elastic fiber comprising 20% spandex and 80% nylon SMPs was mixed with thermoset styrene-based SMPs to enhance the mechanical properties of composites. With the addition of elastic fiber, Young's modulus and strength of SMPs at high temperature were enhanced and the tear strength of pure SMP at room temperature was also improved. Figure (2.5) shows a Dynamic mechanical analysis test applied for styrene SMPS and elastic fiber with 0%,20%, and 40% volume fiber fractions that were fabricated for experiments[46]. The modulus decreases from 1800-1400MPa to 30 -10 MPa at 60°C for all fiber fractions.

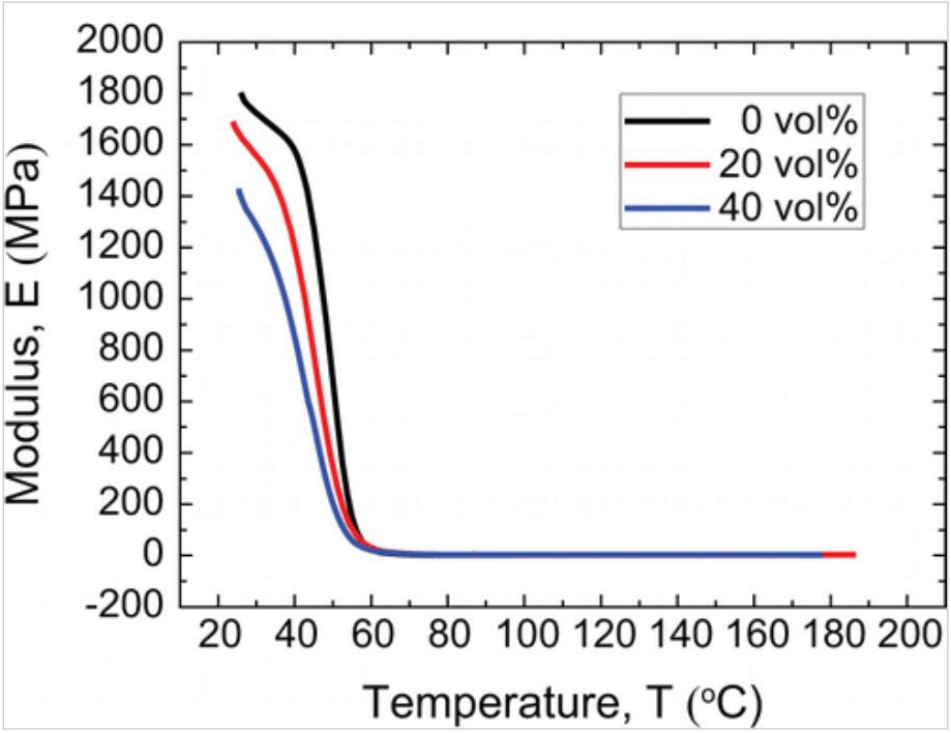

Figure 2-5 curves of storage modulus of SMPs vs temperature with different fiber volume fractions.

Shape memory polymer base with silicon carbide (SiC) nanoparticulate reinforcements was tested for mechanical tests. The Modulus versus temperature curve from DMA testing was conducted for both base resin and a 20% SiC reinforced resin. For SMP base resin and the 20% weight fraction reinforced resin the loss modulus started to decrease around 60°C. The storage modulus started to drop around 25°C and the rate of decrease of the storage modulus increased as the temperature reaches 60°C. The beginning of the tan delta curve appears at around 40°C for both materials. The peak of the tan delta curve or the peak for the modulus curve are used to identify the glass transition. From the peak of the tan delta curve, the glass transition of unreinforced SMP material was found to be 75.5°C (see Figure 2-6 a), whereas the glass transition for the 20% reinforced was 68.2°C (see Figure 2-6 b).

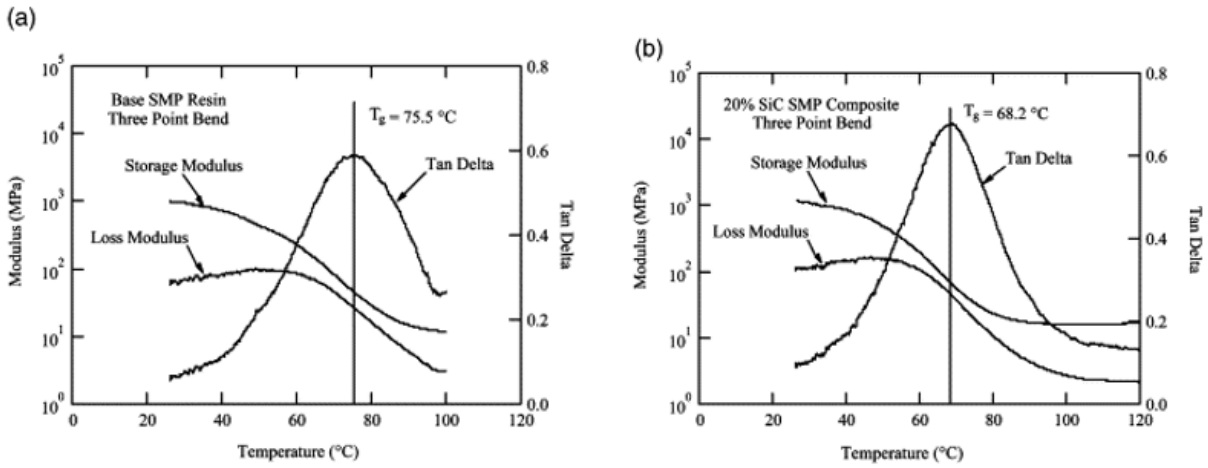

Figure 2-6: Modulus as a function of temperature from DMA testing for (a) the base resin and (b) a 20% SiC reinforced resin

2.2.2 Thermal Properties

Thermal mechanisms are key components to evaluate the shape memory effect. To investigate the thermal properties of SMPs, thermo-mechanical cycles are applied to SMP samples. As stated before, Appling a heat source to SMP samples allows to transition from the glassy to rubbery behaviors, where the SPMs can deform into a new temporary shape.

Thermal crosslinking is one main parameter structured in different SMPs systems, which affects the molecular morphology and shape memory effect (SME). Figure 2-7 display a PU (SMP) mechanism which is chemically crosslinked. Here, when the PU is initially created, it forms the primary crosslinking net points that initiate the permanent shape. Heating the PU above the glass transition temperature reduces the stress of the polymer. The addition of external force causes the polymer to inherit a temporary shape. Once the desired temporary shape is targeted, the crosslinking phase is cooled below the glass transition temperature to freeze the crosslink. When heat is applied again into the PU (without mechanical constraints), the crosslinks return to their initial state [32]. This mechanism is similar to that described in the pho-crosslinked process.

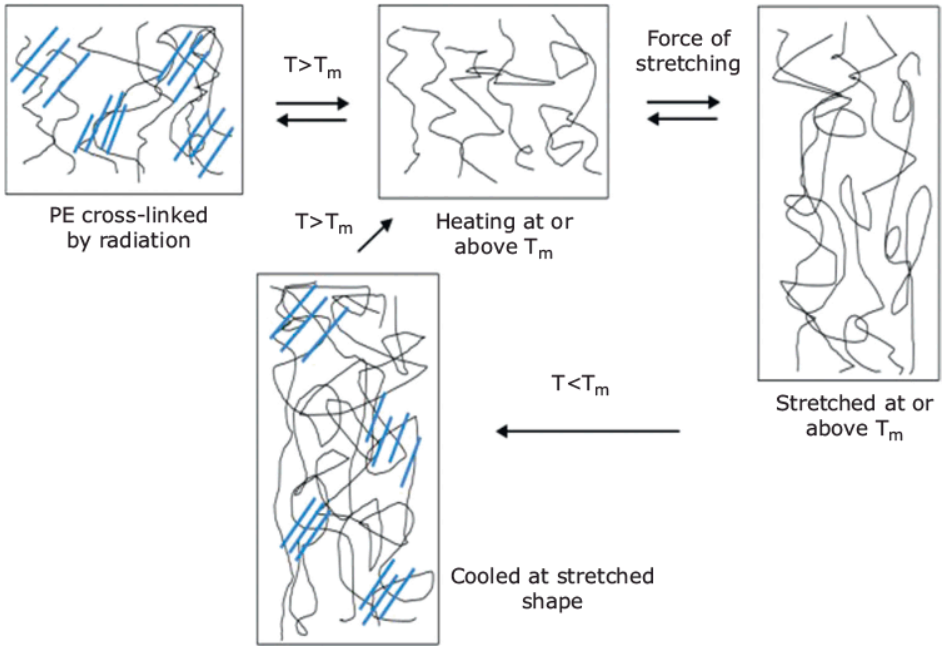

Figure 2-7 Crosslinking SMPE and molecular model of the mechanism of thermally-induced SME [32].

Figure (2-8) shows 3D plots of the SMP cycle. The SMPs start to deform under elevated loading above the transition temperature (Tg). The deformation step is followed by a cooling rate under a constant load. Once the SPM is cooled, the load is removed and the fixed shape (temporary shape) is observed. The SMP obtains the original shape by heating the SMP again without any additional load [32].

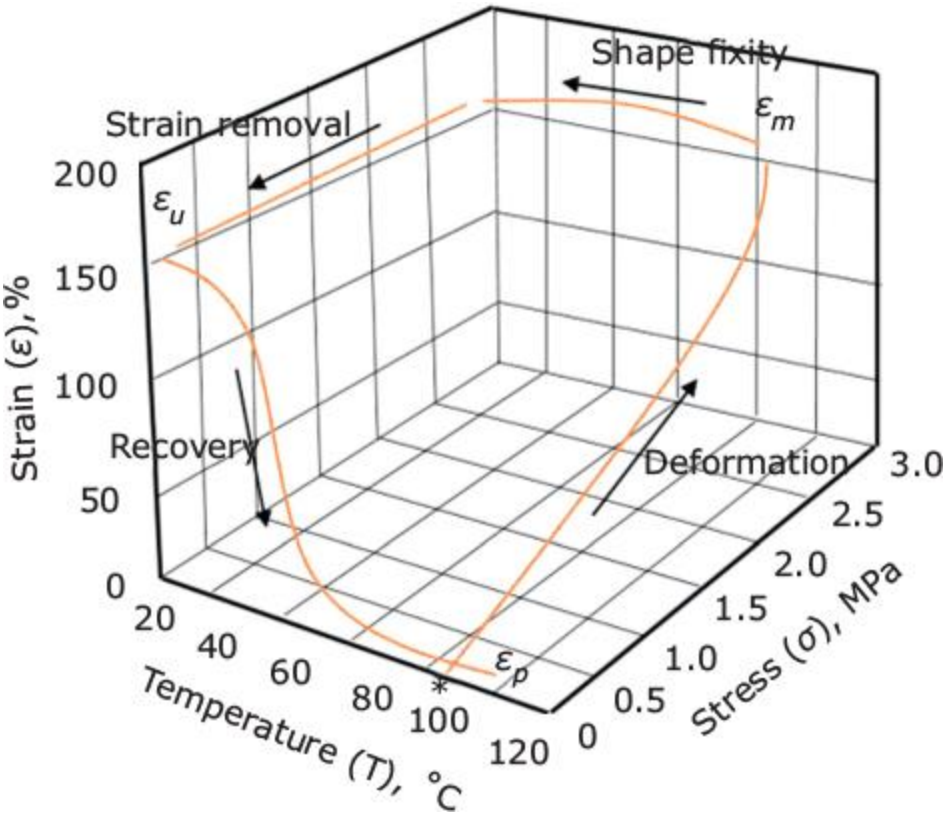

Figure 2-8 3D plot of an SMP through a thermomechanical shape memory cycle [32].

2.2.3 Biocompatibility of Shape Memory Polymer

SMP has shown suitable functionality and capability to actuate which makes them attractive systems in many industries such as aerospace, electrical and medical on drug delivery applications. Bio-SMPs are utilized in medical applications due to their non-toxicity, biodegradability, and biocompatibility [47]. Bio-SMP is approached in biomedical industries as medical devices that have direct contact with interbody organs, tissues, and cells. Therefore, SMPs have been widely investigated for the interface within natural tissues. Bio-SMP can be produced naturally or synthetically to satisfy certain criteria such as bio functionality, biostability, and biocompatibility during implantation. Biocompatibility refers to the ability of the material to perform a desired and appropriate function concerning a medical therapy without any undesirable systemic effects on the beneficiary of the therapy [48]. In

general, biocompatible polymers are plastic that is tolerated by living organisms [49]. Much research and investigations are conducted to study biomedical SMPs and their applications in the medical field [50]. Lendlein [51] has introduced much information about the potential of Bio-SMPs applied in implants, surgical instruments and extracorporeal devices in the biomedical applications Lendlein also introduced the first commercial biocompatible polyurethane (SMP). Few Bio PU were created by Mitsubishi Heavy Industries, Ltd (Nagoya, Japan) [52].

An attractive way of introducing biocompatibility of SMP is through scaffolds with electrical properties and biomimetic structures with promising engineering applications for nerve tissue. SMP polyurethane, which consists of organic poly(Ɛ-caprolactone) PCL segments with inorganic polydimethylsiloxane (PDMS), has been synthesized. The incorporation of carbon fiber with polymers was later introduced and the addition of carbon nanofibers was followed. The study shows that adding carbon nanotubes to nanofibers increases the fiber diameter from 339 ± 76 nm to 619 ± 138 nm, decreased resistivity from 3.6 GΩ/mm to 1.8 kΩ/mm, and decreased the crystallinity from 33 to 25%. All polymers (PCL/PDMS)-carbon fiber composites experienced satisfactory shape fixity ratios of >82% and shape recovery ratios of >90% after 5 thermal-mechanical cycles at a temperature of 45°C (table 1). Tables1 also shows the combination of poly (PLC/PDMS) with CNTs/carbon black (based on carbon ratio P5, P5C05, P5C1, and P5C2) which could be used for the creation of smart 4D printing structures The performance of the SMP with the addition of different ratio of CNTs/carbon black composite is shown in table1 [53].

Table 1: shape recovery ratio (Rr) and shape fixity ratio (Rf) of the nanofibers[53].

Fibers	Polymer:carbon (w/w)		Cycle 1	Cycle 2	Cycle 3	Cycle 4	Cycle 5
P5	N.A.	R_f (%)	84.9	84.9	85.0	85.1	85.1
		R_r (%)	91.6	94.9	97.1	97.5	99.6
P5C05	5:0.5	R_f (%)	82.6	83.3	82.7	82.6	82.8
		R_r (%)	90.2	94.2	96.3	96.5	96.7
P5C1	5:1	R_f (%)	87.6	87.9	88.2	88.3	88.3
		R_r (%)	88.3	93.8	95.7	92.6	99.2
P5C2	5:2	R_f (%)	84.4	84.5	84.8	85.2	85.0
		R_r (%)	90.4	93.6	94.4	96.6	97.2

PC12 cells were incorporated into poly(PCL/PDMS urethane) and poly(PCL/PDMS urethane)/ carbon nanofiber to promote bio-cell to bio-cell interaction. The proliferation of PC12 with SMP was studied over 9 days. Cells on P5 showed the highest cell proliferation, indicating good biocompatibility. P5C2 showed the lowest cell proliferation rate, indicating that a high content of carbon black might be toxic to nerve cells as shown in Figure 2-9 [53].

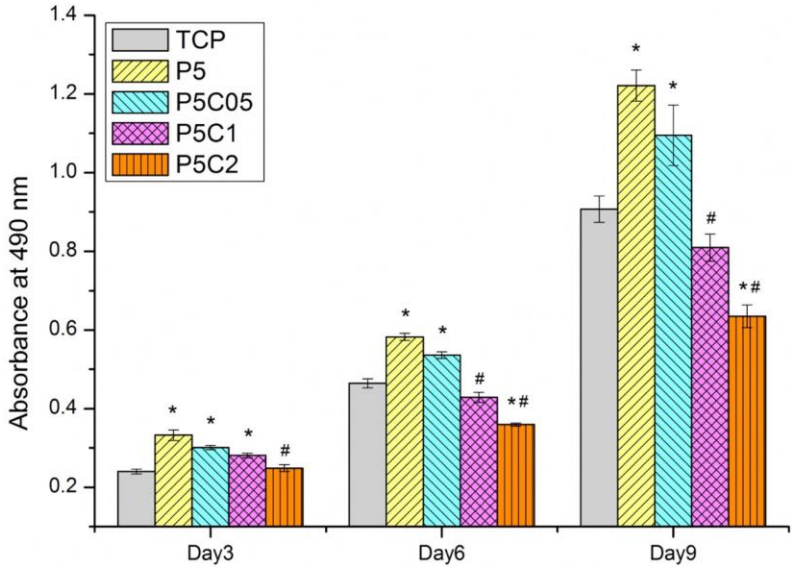

Figure 2-9: Proliferation of PC12 cells on the shape memory nanofibers, obtained by MTS. *$p < 0.05$ compared to TCP at each time point; #$p < 0.05$ compared to P5 nanofibers at each time point [53].

2.3 Additive Manufacturing Shape Memory Polymer.

Additive manufacturing (AM) of shape memory polymers is an innovative way of creating smart materials that can be used in different industries for their unique functionality [54]. Utilizing the advanced technology of additive manufacturing or 3D printing has the advantage of producing a part with complex geometries, low cost, and diversity of material [55]. 3D printing techniques have been demonstrated for multi-materials such as metal, ceramic, and plastic [56]. Additive manufacturing of SMPs occurs by integrating 2 or more materials to create self-sensing and lightweight structures [57]. Additive manufacturing techniques for creating SMPs include vat photopolymerization (VPP), which consists of digital light processing (DLP) and stereolithography (SLA), and fused filament fabrication (FFF) [58]. Additive manufacturing is developing rapidly-the global revenue in the additive manufacturing sector. It was estimated to be $12 billion in 2020 and is expected to reach $78-$100 billion by 2028 [59]. Therefore, the SMP technology has the opportunity to be highly influenced by the surge in additive manufacturing.

2.3.1 Vat Photopolymerization (SLA, DLP)

3D printing or additive manufacturing was first discovered over 30 years ago by Charles Hull. In 1986, the term stereolithography (SLA) was coined in his patent which explained the method of creating very thin solid objects layer by layer using a photosensitive material and ultraviolet (UV) laser light for curing [60]. Nowadays, additive manufacturing is used closely with computer design software to fabricate and build complex objects. 3D printing has applications in various industries like dental, biomedical, automotive, and food [61,62]. 3D printing has found a niche industry like transferring medical treatment from one size to custom sizing, and from generalized medicines to personalized [63]. The American Society for Testing and Material (ASTM) divides 3D printing technology into seven classes: vat photopolymerization, powder bed fusion, material jetting, binder jetting, material extrusion, directed energy deposition, and sheet lamination. DLP and SLA printing fall under the vat polymerization (VPP) category and offer high printing resolution [64]. Vat photopolymerization is used to describe 3D printing technologies that utilize computer-controlled photopolymerization to create a solid object from a vat of liquid resin. VPP processes include stereolithography (SLA), continuous light interface production (CLIP), digital light processing (DPL), and two-photon polymerization (2PP) [65].

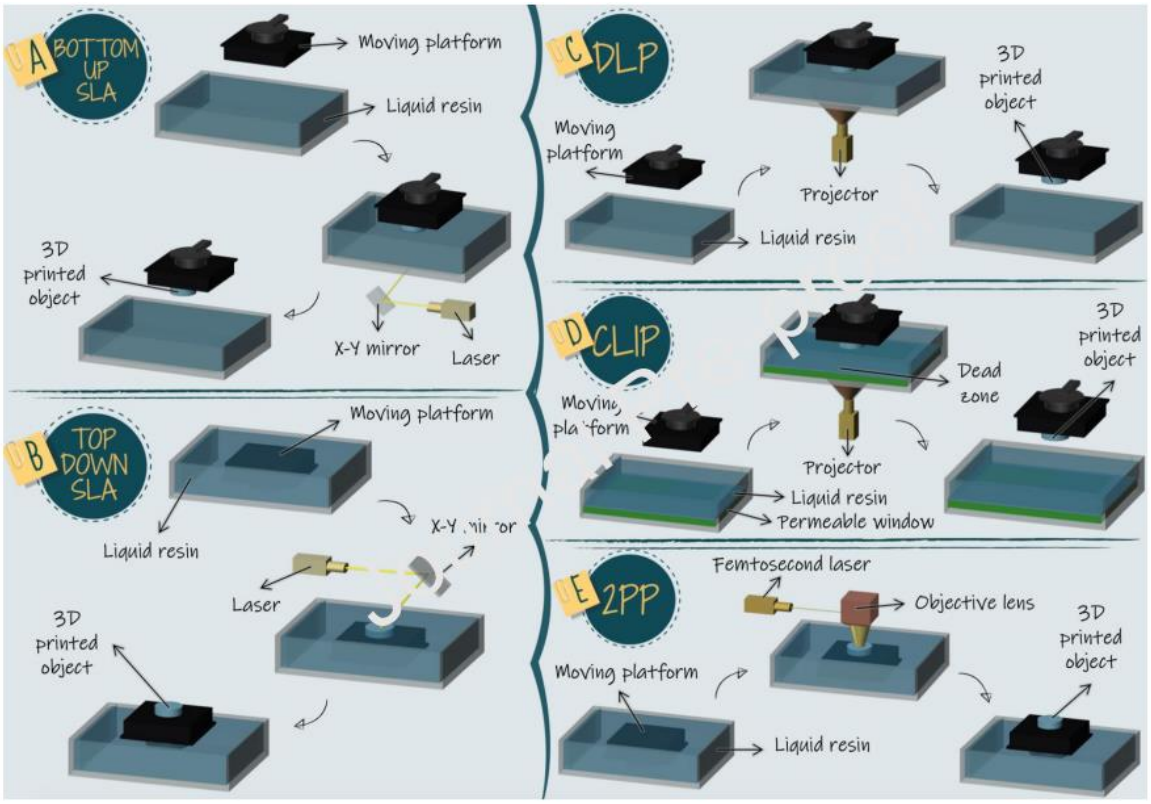

Figure 2-10: Schematic representation of a (A) bottom-up SLA, (B) top-down SLA, (C) DLP, (D) CLIP and (E) 2PP 3D printing [65].

Shape memory polymers have shown an increase in research and development in recent years. Many 3D printing technologies are used to create shape memory polymers like stereolithography (SLA), selective laser sintering (SLS), and fused filament fabrication (FFF). Those printing techniques are slicing the computer-aided designed model into layers which are next printed. During the past few years, there were an increase in research and development conducted on combining both printing and SMPs technologies, which results in technologies called 4D printing. Figure (2.11) shows the increase in popularity among the scientific community by searching "3d print* shape memory" and "shape memory polymer. On the other hand, research on SMP and 3D printed shape memory polymers still increasing [66].

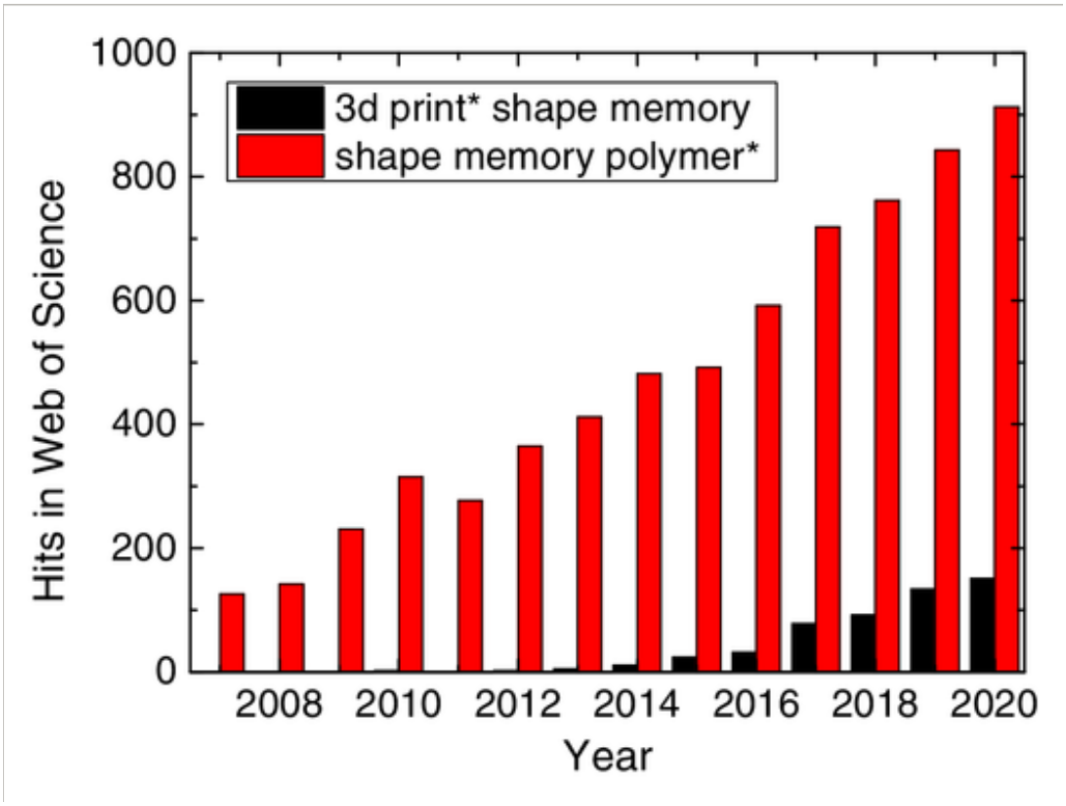

Figure 2-11: Results in the Web of Science, searching for "3d print* shape memory" and "shape memory polymer" [66].

Some attempts have been made by Randchenko et al [66] to develop material for 3D printing by the SLA technique. His material consists of cycloaliphatic epoxy-functionalized ionic liquid with one and two imidazolium units. To increase and improve the adhesion of the crosslinking rate, a thermoacid generator-diaryliodonium hexafluoroantimonate was used, which leads to a poly-ionic liquid network that shows a rubbery state. From the presence of cycloaliphatic epoxy-functionalized ionic liquid, all networks undergo and showed shape memory properties with attractive shape maintenance at the temporary shape and recovery properties

Miao et al [66] have a combination of photolithography and PLA to produce hierarchical micro-pattern using smart soybean oil epoxidized acrylate ink for bone marrow mesenchymal stem cell growth and alignment. The printed scaffolds could be

triggered to self-assemble into a rolling structure by expression in ethanol which caused a cross-link density gradient due to the photolithographic process.

2.3.2 Fused Deposition Modeling

In 1989 S.Crump et al [67–69] patented and invented a new 3D printing method called Fused Deposition Modeling (FDM), also called fused filament fabrication (FFF). FFF is one of the most known 3D printing techniques in additive manufacturing due to its ability to print complex objects with outstanding thermal and chemical resistance and excellent strength. FFF is influenced by various printing parameters which control the part of the printing accuracy [67]. FFF is a technology that allows rapid and precise development of fabricating functional components by layers, formed by extrusion of plastic filament that is melted through a heated nozzle to form parts [70]. With the FFF process, materials are deposited in a layer-by-layer configuration and are solidified immediately the following extrusion from the nozzle[71]. FFF printing requires the printhead to move in the X, Y, and Z direction above the build platform to build CAD-designed 3D objects as shown in figure 2.12 [72,73].

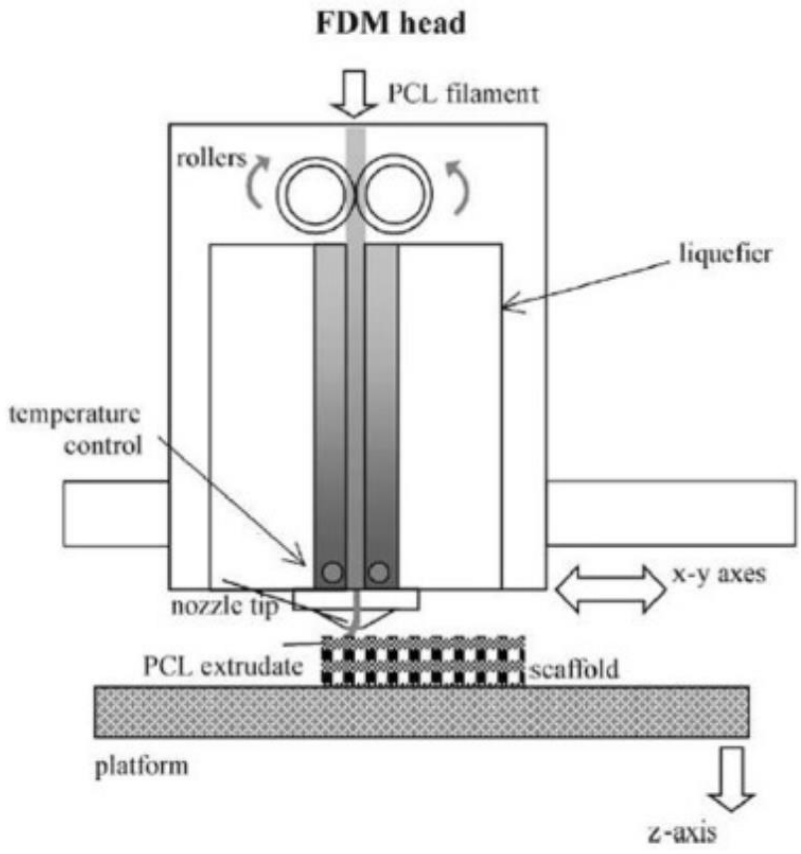

Figure 2-12: Schematic of the FFF additive manufacturing process[74].

Yue et al [75] studied the 3D printing of cellulose nanofiber reinforced poly-hydroxybutyrate / poly(ε-caprolactone) / iron oxide (PHB/PCL/Fe_3O_4) magneto-responsive shape memory polymer composites with attractive mechanical properties. The combination of 3D printing technology and shape memory polymer composites represents a great opportunity for customized and intelligent products. The magneto-responsive shape memory polymer was developed with balanced toughness and strength by adding Fe_3O_4 and cellulose nanofibers (CNFs) to a PHB/PCL (80:20) composites as reinforcing materials. SEM analysis was applied to investigate the micro-morphology of PHB/PCL blends and composites with different Fe_3O_4 and CNFs contents (Figure 2-13).

In Figure 2.13(a), it can be observed how the PCL is diffused in the PHB matrix in the form of spherical droplets with gaps between the PHB phase and PCL phase due to the weak interfacial between PLC and PHB. Figure 2.13 (b) shows that the Fe_3O_4 particles are evenly diffused in the PLC/PHB blend. The SEM image also shows interspaces between the PCL/PHB blend and Fe_3O_4, which explains the weak inter-boding. Figure2.13(c) shows large aggregates of Fe_3O_4 (JF15%)which are noted by the red arrow. Figure2.13 (d&e) shows the addition of low content of CNFs which did not affect the diffusion of Fe_3O_4 in the matrix of JF10%C0.5% and JF10%C0.75% samples. However, Figure 2.13 (f) shows that when the CNF (cellulose nanofibers) weight fraction was 1%, larger Fe_3O_4 aggregates were observed compared to the sample JF15%. This could be caused by the increase in hydrogen bonding force between Fe_3O_4 and CNFs during the ultrasonic treatment process.

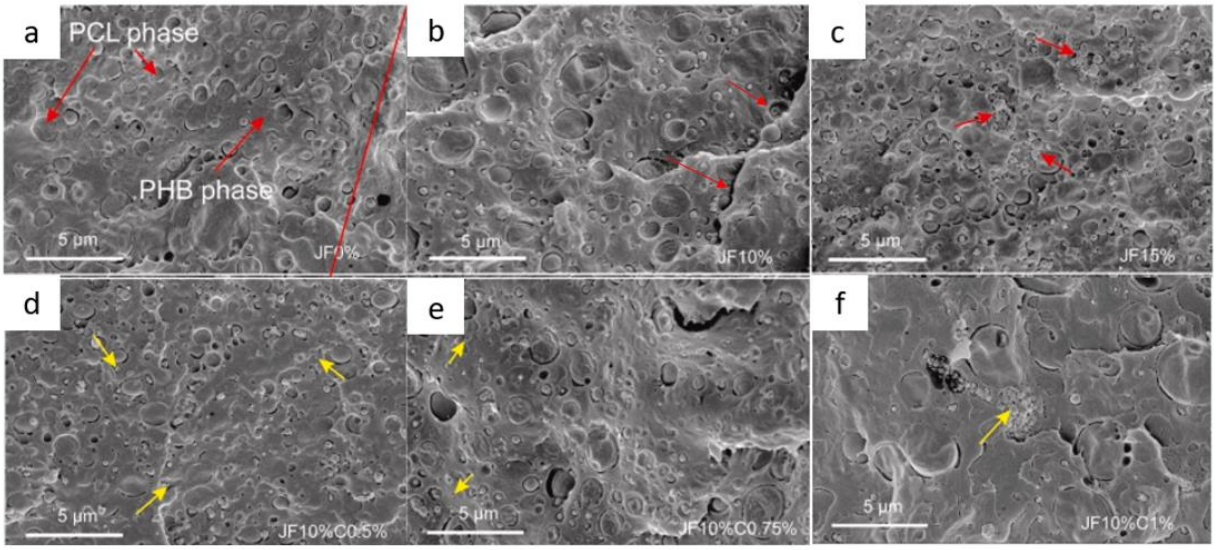

Figure 2-13: SEM images of composites with different Fe_3O_4 and CNFs contents. (a) Neat PHB/PCL blends (The proportion of PCL is 20 wt%). (b) (c) the composites with 10 wt%, and 15 wt% Fe_3O_4 respectively. (d) (e) (f) Composites with 10 wt% Fe_3O_4 with CNFs contents of 0.5 wt%, 0.75 wt%, and 1 wt% [75].

Tensile tests were applied to CNFs/Fe3O4-based PHB/PCL composites. It can be observed that the addition of Fe_3O_4 increases the tensile strength and elastic modulus of the PHB/PCL blend. The tensile strength of JF10%(37.82MP) increased by 12.92%

more than the neat blend (33.71 MPa) as shown in figure 2.14 (a). It can be caused due to the reinforced interaction between uniformly-diffusion Fe_3O_4 particles and matrix that increase the maximum stress and reduce the stress concentration. Figure 2.14 (b) shows the addition of CNF composite to the 10 wt. % Fe_3O_4 composites increase the tensile strength of the Fe_3O_4. In contrast, figure 2.14 (c) shows that the elongation at the break decreases by increasing the amount of Fe3O4 from 278.7% to 10.07%. However, Figure 2.14 (d) shows an enhancement in the Elongation at the break of the JF10% composite with the addition of C0.5% from 22.82% to 60.79%. Figure 2.14 (e) shows the Elastic Modulus increase from 849.7 MPa to 1044.9MPa with a proportional increase of Fe_3O_4. it is also shown an increase in the Elastic Modulus with increasing of CNFs to the JF10wt% from 982.4 MPa to 1011.9 MPa as shown in figure 2.14 (f) [75].

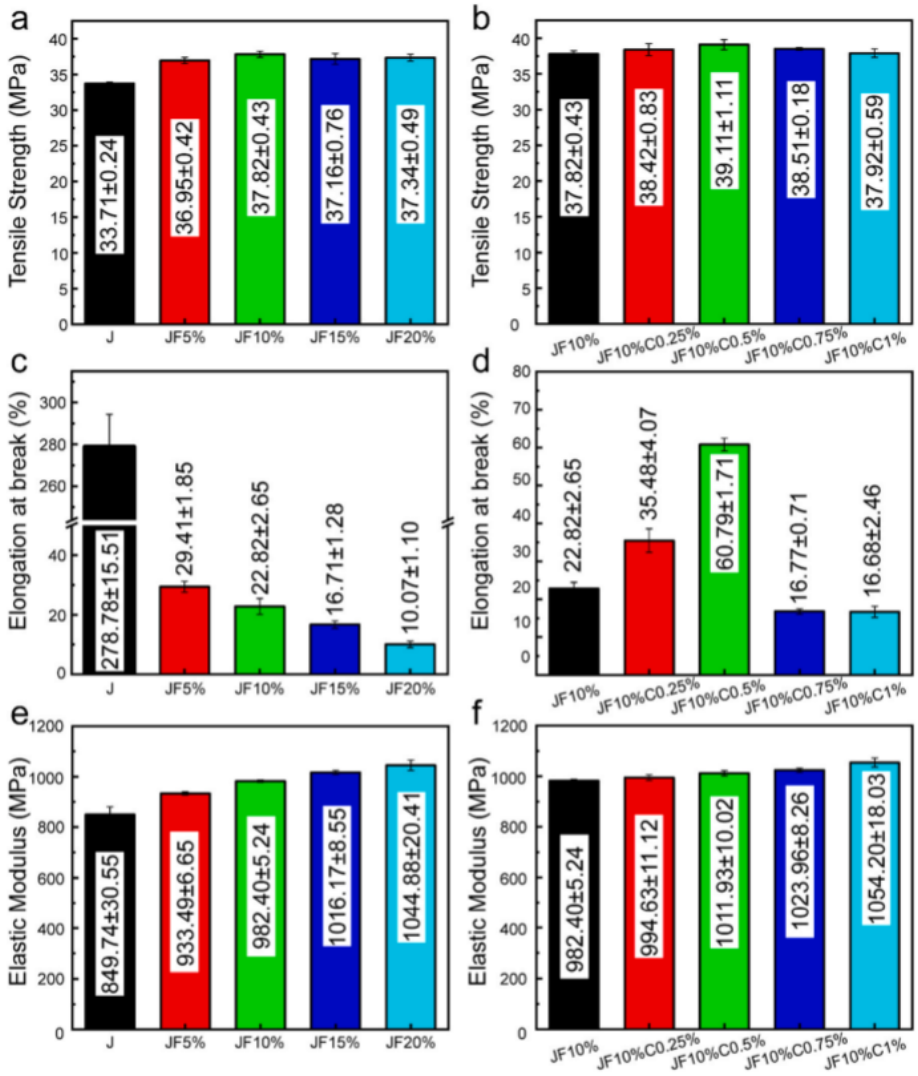

Figure 2-14: (a) (b) Tensile strength, (c) (d) elongation at break, (e) (f) elastic modulus of the composites with different Fe3O4 and CNFs contents, (g) Stress-strain curves of the JF10% and JF10%C0.5% samples [75].

Figure 2.15 shows the magnetic field triggering the shape recovery behavior (instantaneous shape and thermal distribution) of the JF 10% and JF10%C0.5% samples through the shape recovery. It is observed that the increase of the temperature of the sample induced by a magnetic field and the temperature of the edge is lower than the temperature of the inside due to the temperature dissipation. In this work, all samples were placed in a temporary U- shape position above a magnetic induction coil

to ensure equal magnetic field strength. The sample JF10% shows a faster shape recovery time (24s) whereas the sample of JF10%C0.5% shows a slower shape recovery (35s). they suggested that the CNFs reduce the degree of chain entanglement of the blend molecules, which reduces the elastic energy [75].

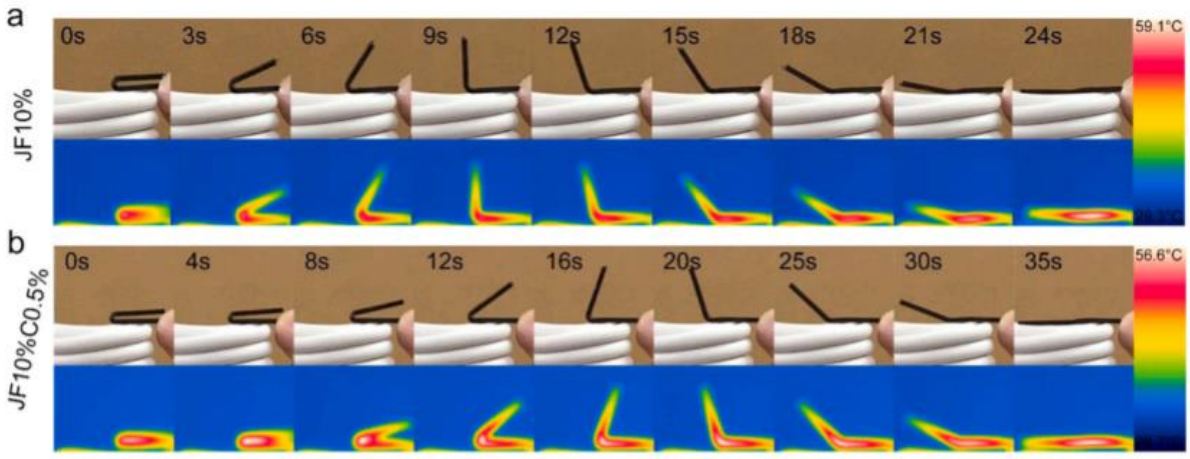

Figure 2-15: (a and b) Magnetic field triggering the shape recovery behavior (the instantaneous shapes and thermal distribution) of the JF10% and JF10%C0.5% [75].

2.4 Application of 3D printed Shape Memory Polymer

Because shape memory polymer can respond to various stimuli such as temperature, pH, and light, the incorporation of SMP and additive manufacturing and 3D printing creates opportunities for functional SMP to be fabricated in distinct sizes and complex structures. Those features will expand the application of SMP in different filed such as aerospace, medical, and electronics.

A successful application of 4D printed shape memory polymers in the biomedical field is as an intravascular stent. An intravascular stent is a tube that supports the walls of the blood vessels. The application of SMPs in the biomedical field has the advantage of low bio-toxicity and biodegradability, which helps to overcome a lot of difficult problems. Therefore, the technology of 4D printing has become increasingly popular, utilizing different printing methods such as DIW, FFF, and SLA. Wei et al [76] created an SMP that consisted of magnetic Fe_3O_4 nanoparticles

and PLA which could be deformed by magnetic stimuli. The direct-writing technique was utilized to create the spiral intravascular stent structure. The vascular stent was self-expandable and was stimulated by the magnetic field. This SMP could also completely deform in 10 seconds (Figure 2.16). To overcome cardiovascular diseases such as vascular stenosis in coronary heart disease, self-expandable vascular stents can be used. Once the stent is triggered by the external magnetic field, the stent enlarges to support the stenosis of the vascular. As a result of the stenosis, the vascular stent will allow the blood to circulate normally. Magnetically-stimulated SMP materials and 4D printing technologies are particularly useful in the biomedical industry. The technology is opening the door for remote-controlled medical devices and new possibilities for minimally invasive surgery.

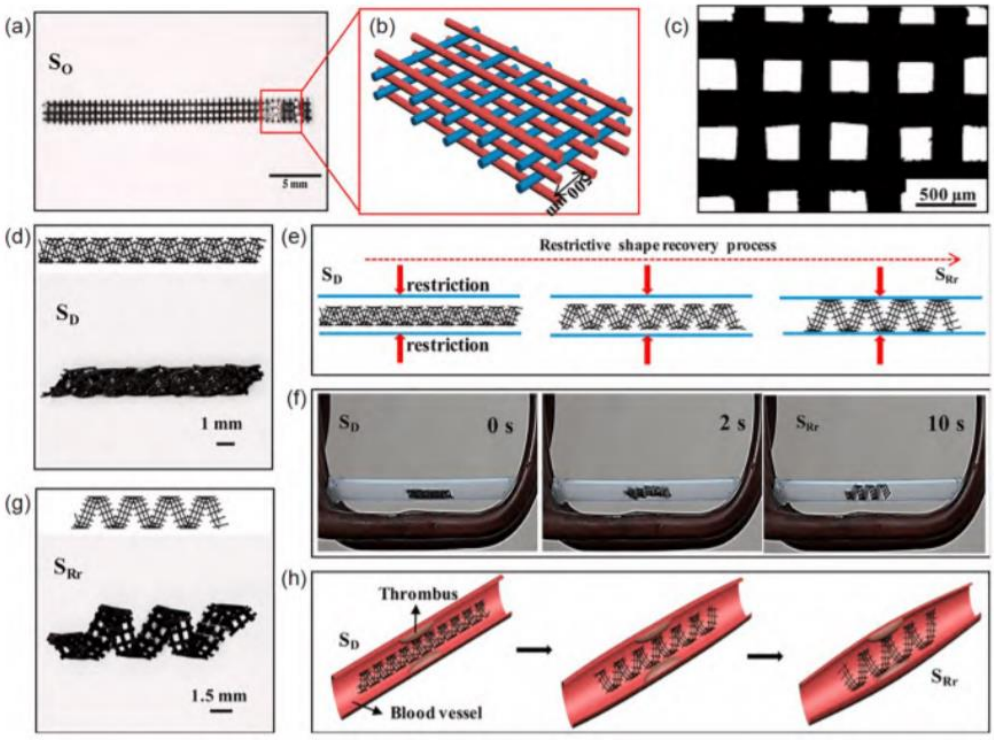

Figure 2-16: DW printing of a 4D scaffold by PLA/Fe3O4 ink and its potential biomedical application: (a) optical image of the multilayer scaffold; (b) schematic diagram of the detailed structure of the scaffold; (c) top view of the optical image of the printed scaffold; (d) deformation shape of the printed scaffold; (e) schematic of the restrictive shape recovery process; (f) demonstration of the restrictive shape recovery process triggered by a 30 kHz alternating magnetic field; (g) recovery

shape under restrictive conditions; (h) potential application of the 4D scaffold as an intravascular stent [76].

Bio-SMP can be used in endoscopic surgery as a surgical suture. In general, sutures are may damage the cell of the skin, if they were not stitched very properly or if the threads were too tight. Indeed, if threads are too loose, they will not be functionally effective. SMP with self-tightening can help overcome those problems. In the position of SMP, a suture made of SMPs can be stitched loosely in its temporary state and then come into contact with body temperature or transition temperature (Tg), it can be tightened accordingly. SMP sutures will help reduce the skin damage risks. SMPs sutures with biodegradable and biocompatible features would be more promising for wound closing devices. Lendlein [47] has placed effort into developing biodegradable SMPs surgical sutures. They presented hydrolyzable ester linkages into the polymer structures so they cleave under physiological conditions. The degradation can be managed by varying the composition and mass content of the precursor macrodiols. The polymer should lose mass linearly in vitro, causing a continuous release of degradation products leading to less risk of inflammatory response. In the in vivo, it was observed that the wound was closed and the knot was tightened when the temperature increased to 41 °C (see Figure 2-17).

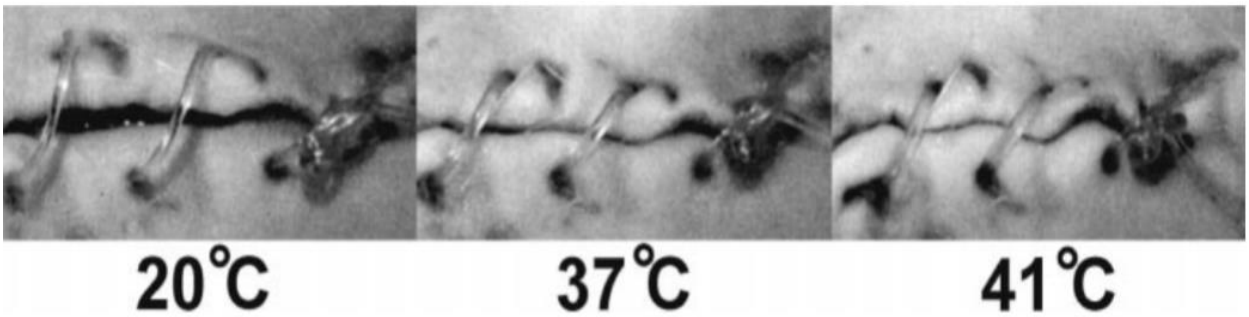

Figure 2-17: Degradable shape-memory suture for wound closure. The photo series from the animal experiment shows (left to right) the shrinkage of the fiber while the temperature increases [47].

2.5 Lithium Battery

The supply of environmentally sustainable energy has become one of the most scientific challenges facing humanity in the 21st century. Environmental security, energy security, and economic security can all be merged in introducing the energy issue within the next few decades [77]. Over the past decades, more scientific research has focused on energy demand and environmental issues related to fossil energy and renewable energy such as solar, hydroelectricity, or wind to replace the traditional fossil fuels [78]. Meanwhile, the sustainable energy supply and electrical energy system are capable of capturing the energy generated now and supplying it when it's needed to reduce the imbalance between energy production and demand could contribute to a low cost [79,80]. Because of the electrical energy system, high energy density, power density, and life cycle, lithium batteries, an electrochemical device used as a rechargeable battery, are reported the most important storage device [81]. Lithium was discovered by the Swedish chemist Arfwedson [82] in 1817 during the analysis of the mineral petalite (LiAlSi4O10). Lithium was later isolated by Brande Davy [83] through the electrolysis of lithium oxide in 1821. A century later Lewis [84] started to research and explore lithium electrochemical properties, considering lithium's attractive physical properties such as high specific capacity (3860 mAh g^{-1}), low potential (- 3.04 V vs SHE), and low density (0.534 g c-3). In 1958 Harris [85] investigated the solubility of lithium in different non-aqueous electrolytes including cyclic esters (carbonate and ϒ- butyrolactone), and inorganic lithium salt (LiClO4) dissolved in propylene carbonate (PC). Harris detected the formation of a passivation layer that was able of preventing a chemical reaction between electrolyte and lithium while allowing the lithium-ion to cross, which led to the studies of the stability of lithium-ion batteries and the commercialization of primary lithium batteries. The non-aqueous 3V lithium-ion batteries have been available commercially as a cathode in the market since the 1960s, including lithium-sulfur dioxide (Li/SO2) in 1969, lithium – polycarbon monofluoride (Li/(CFN))n manufactured by Matstushita in 1973 and so

many other lithium batteries that give the birth to rechargeable to lithium-ion batteries [86–88]. The prototype lithium-ion battery was developed by the work of Akira Yoshino in 1985 based on masterful research by M. Stanley Whittingham, Rachild Yazamni, and Koichi Mizaushuma between the 1970s-1980s [89–91]. Sony corporation and the Asahi Kasei team are the first to release the commercial lithium-ion battery introduced by lithium cobalt dioxide that was modified somewhere from Goodenough's earlier work. This development of Sony battery was modified over years bringing more battery technologies. The past years have shown growth in the benefit of lithium-ion batteries in several industries such as cellphones, laptops, aerospace, electronics, micro- electrochemical system, and electrical vehicles (Blomgren GE and Reddy MV).

2.5.1 3D printed battery

Additive manufacturing has shown a significant interest in fabricating 3d printed battery electrodes, which is a promising, efficient, and controllable technique in fabricating high complex battery architectures [92]. Several additive manufacturing techniques we incorporated in the designing and manufacturing of lithium battery parts. Research done by Yinhua and his team [93] developed a patterned stretchable electrode using Direct Ink Write (DIW) printing technology using highly viscous electrode ink including incorporation of lithium iron phosphate (LiFePO4) or lithium titanate oxide (Li4Ti5O12) nanoparticles with, multi-walled carbon nanotubes (MWCNT's) and poly(vinylidene fluoride) (PVDF) dissolved in n-methyl-2-pyrrolidone. The inks were extruded precisely onto a polyimide sheet based on pre-designed shapes see figures (2-18 a&b). The electrode exhibited a decrease in viscosity when the share rate increased. The high result of viscosity is 10^4 around the shear rate of 0.015 s^{-1} for electrodes which display the printability and shape ability. It was marked that the DIW 3D printing technology enables high accuracy, low cost, and effective printing process. After completing the printing process the designed electrode was left to dry and lifted from the polyimide substrate to stand free figures (2-18 c).

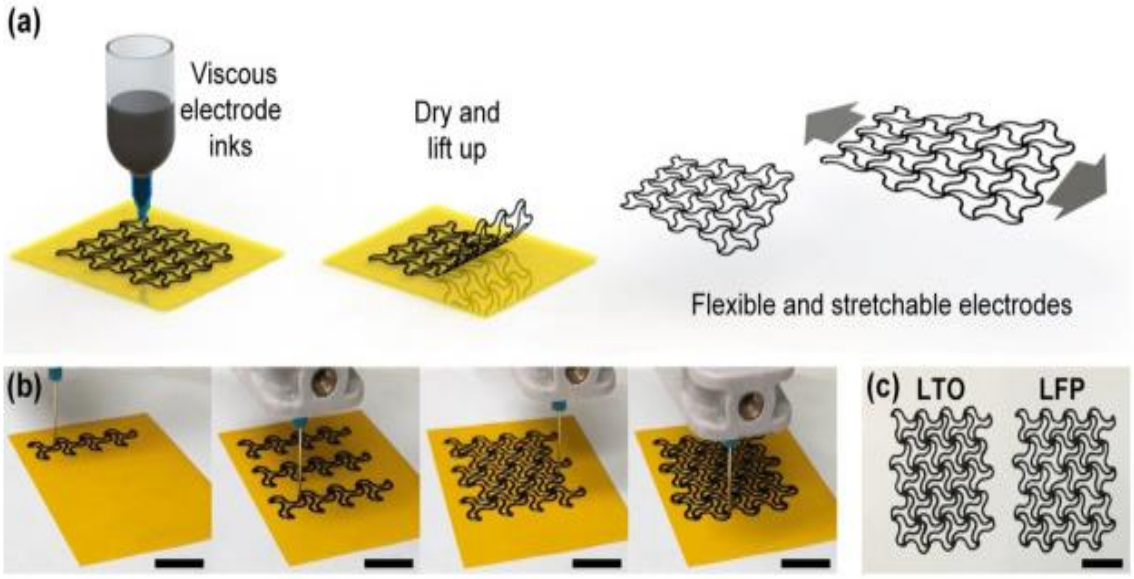

Figure: 2-18 Patterned stretchable electrodes fabricated by 3D DIW printing. (a) The fabrication processes. (b) Optical photos at different steps during the printing process. (c) Optical photos of the as-made stretchable LTO and LFP electrodes. The scale bar is 1 cm [93].

Ragones et al [94] used a similar approach using on a 3D FFF 3D printer where LiFePO4 based film is the cathode and Li4Ti5O12 film is the anode. Also, the anode and cathode current collectors and ion-conducting membrane or solid electrolyte are fabricated concurrently, therefore qualifying free form-factor batteries. By utilizing the FFF techniques, the electrode networks might be designed according to the application shape. See figure (2.19).

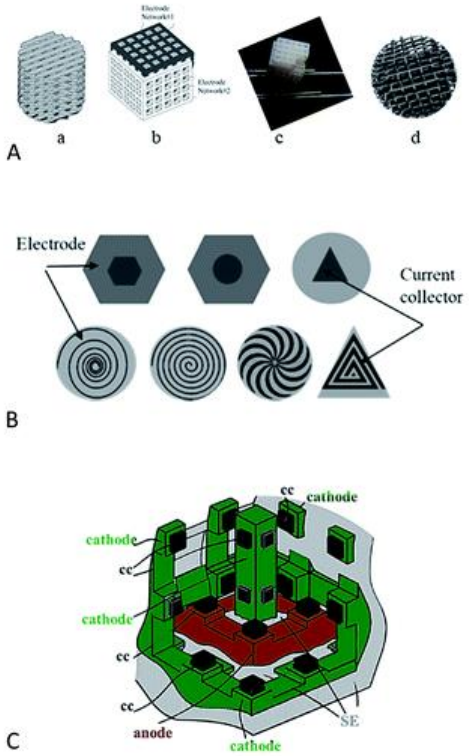

Figure 2-19 : (A) Schematics (a and b) and 3D printed models (c and d) of the interlaced electrodes networks. (B) Schematics of the cross-sectional views of core-shell electrodes. (C) Pictorial view of a 3D battery [94].

2.5.2 Electrical Performance of 3D printed Batteries

Yinhua et al [93] introduced the electrochemical performance of the 3D printed electrode in the undeformed state utilizing the DIW printing technology. Materials and components used to develop the battery are LiFePO4, Li4Ti5O12, MWCNT's, and PVDF dissolved in n-methyl-2-pyrrolidone solution. Figure 2-20 (a) shows the voltage profile discharge/charge of the printed Li4Ti5O12 electrodes in the voltage of 1.0_2.5 V at 0.3 C (1 C = 170 mAh g^{-1}) in comparison with conventional slurry-cast Li4Ti5O12 electrode using copper foil. It is observed that the 3D printed Li4Ti5O12 electrode can distribute a discharge capacity of 166.1 mAh g^{-1} at the initial delivery and then a discharge capacity of 139.7 mAh g^{-1} after 50 cycles, compared to the conventional slurry-cast electrode. The capacity loss can be accredited to the

development of solid electrolytes on the surface of the Li4Ti5O12 electrode and a side reaction between the liquid electrolyte and Li4Ti5O12 nanoparticles. The curve also presents a steady discharge/ charge voltage of around 1.53 V and 1.61 V. The rated capacity of the Li4Ti5O12 electrode and the related discharge/charge voltage profile are also introduced in figure 2-20 (b). Due to the conductivity of the MWCNT's on the 3D printed Li4Ti5O12 and the slurry-cast Li4Ti5O12 electrodes exhibited good rate capability. It was observed a decrease in the discharge capacity of the Li4Ti5O12 electrode from 137.0 to 129.0 to 117.0 mAh g^{-1} when the current rate increased from 0.3 C to 0.6 C and 1.0 C as shown in figure (2-20b). The printed Li4Ti5O12 electrode showed great stability after 50 cycles and maintained a capacity of 136.4 mAh g^{-1} and high efficiency of 99.4% at a rate of 0.3 C (see Figure 2-20 c). Comparing Li4Ti5O12 electrode and LiFePO4 electrode, LiFePO4 electrode exhibits higher voltage profile rage between 2.0_ 4.0 V at 0.3 C (1 C = 170 mAh g^{-1}), showing charge/discharge capacities of 157.8 and 154.5 mAh g^{-1}, corresponding to the slurry-cast LiFePO4 electrode. The curve shows long and steady discharge/ charge voltage around 3.35V and 3.48 V for both the first and 50^{th} cycle correspondingly see figure 2-20 (d). when the current rate increases from 0.3 C to 1C, the 3D LiFePO4 electrodes exhibit a good rate capacity that dropped 7% (see Figure 2-20 e). LiFePO4 electrodes performed better cycling where the discharge capacity reaches 99.6% after 50 cycles. It can be observed that the electrochemical properties of the 3D printed electrodes prove reasonable stability compared to the conventional slurry-cast electrodes as shown in figure 2-20 (f).

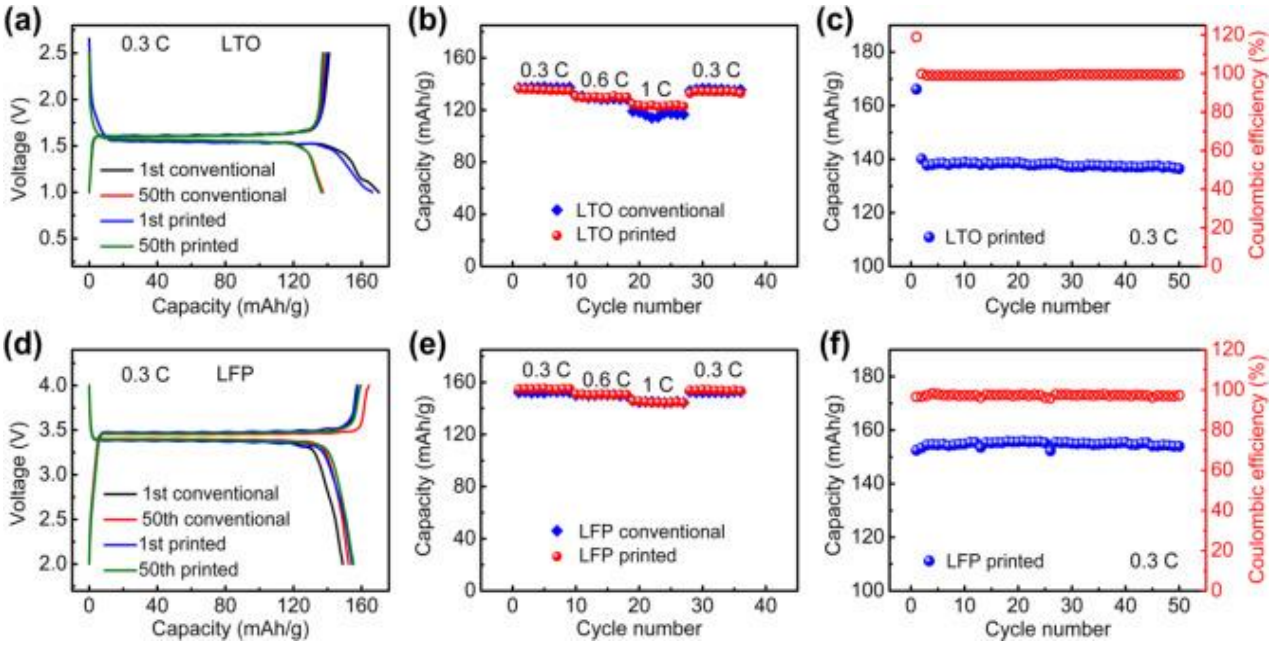

Figure 2-20: Electrochemical performance of the printed stretchable electrodes. (a) Discharge/charge voltage profile of the printed LTO electrode compared with conventional slurry-cast LTO electrodes at 0.3 C. (b) Rate capability of the printed LTO electrodes compared with conventional slurry-cast LTO electrodes. (c) Cycling performance of the printed LTO electrodes at 0.3 C. (d) Discharge/charge voltage profile of the printed LFP electrode compared with conventional slurry-cast LFP electrodes at 0.3 C. (e) Rate capability of the printed LFP electrodes compared with conventional slurry-cast LFP electrodes. (f) Cycling performance of the printed LFP electrodes at 0.3 C.

2.5.3 Advantages and Disadvantages of 3D printed Battery

Additive manufacturing is becoming a global trend in the production field. The demand for additive manufacturing is expanding due to significant revolutionary benefits [95]. 3D printed batteries also known as 3D printed electrochemical energy systems (EES) have recently drawn considerable interest due to the improved electrochemical performance providing areal energy densities and power densities by incorporating the freeform control of complex geometry, offering 3D printing batteries a unique advantage. Indeed, the 3D printing technology allows the fabrication of lightweight and flexible EES to be integrated into wearable electronics [96,97]. At the present, traditional technologies still cannot be implemented on flexible devices [98].

On the other hand, Additive manufacturing has some disadvantages in fabricating EES such as a low processing rate due to low resolution and the slow UV laser beam scanning. Another 3D printing technique used to develop an EES is FFF 3D printing. The first downside of developing batteries using the FFF technique is the inability to produce batteries with high resolution due to the layering method of FFF technology, there are many rigid edges on the surface of the printed batteries which require additional finishing methods such as polishing [99].

2.5.4 Application of 3D printed Battery

Lithium-ion batteries have revolutionized renewable energy sources. The revolution started in the 1970s during the oil crisis when societies were looking for alternative energy sources to replace fossil fuels. Considerable investigations have been conducted since then, testing varied materials to discover the most sufficient approach and application for lithium-ion batteries. Lithium-ion batteries are commonly used for electrical vehicles and portable electronics such as laptops, computers, cell phones, and smartwatches. 3D printed electrodes can be explored in the application of flexible wearable sensors. Here a 3D printed lithium metal battery-based sulfur cathode (Li-S battery) is designed and manufactured using DWI techniques. The cathode is first prepared by mixing graphene, silica oxide (SiO2), and a phenol-formaldehyde (PF) resin paste which is used as the writing ink. The 3D printed cathode exhibits an active material loading of about 10.2 mg cm^2, an initial capacity of 967.9 mAh g^{-1}, and a cycle lifespan of 500 cycles with 505.4 mAh g^{-1} capacity at a current density of 0.2 C. The battery case was 3D printed utilizing the fused-deposition model technique (FDM). The battery lighted up the light-emitting diode (LED) lamp successfully, which indicates the functionality of the additive manufacturing and 3D printing technologies in providing a promising solution with low cost for wearable electronics [100].

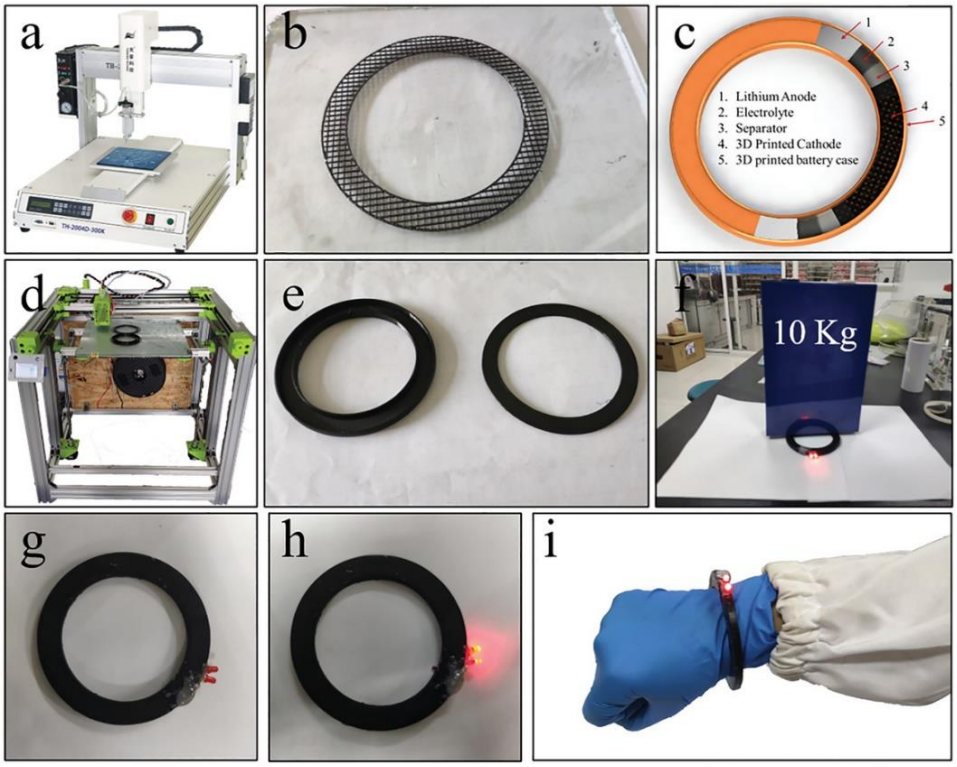

Figure 2-21: Schematic diagram of the fabrication of 3D printed Li-S bracelet battery. a) Direct ink writing 3D printer. b) 3D printed cathode. c) Assembly diagram of bracelet battery. d) Fused deposition 3D printer. e) 3D printed battery case. f) Bracelet battery at a pressure of about 10 kg. g–i) Bracelet batteries with lights on and off, and bracelet battery on the wrist [100].

Wenjie () 3D printed, multilayer graphite (GT) and silicon monoxide (SiO) anode, and lithium nickel manganese oxide (LNMO) cathode to create a lithium-ion battery. The LNMO plane shape cathode was fabricated utilizing direct ink writing technology. Then, the 3D printed battery case was 3D printed using fused deposition modeling technology. the battery case was made of a shell and groove and a lid that can be inserted inside the groove. The heterotypic battery was finally assembled. And sealed with silicone. Two electric wires were drawn; between the cathode and anode, before the plane was fully assembled. The plane shape battery was then used as a power supply for a LED light. Figure 2-22 shows the process followed by Wenjie [x]. For the future demonstration of the structural energy storage, two 3D printed plan shape

batteries were placed in the rear wings of an airplane model. Here the two-plane shape batteries were used as an electrical power supply, showing the combination of structural loading and energy storage [101].

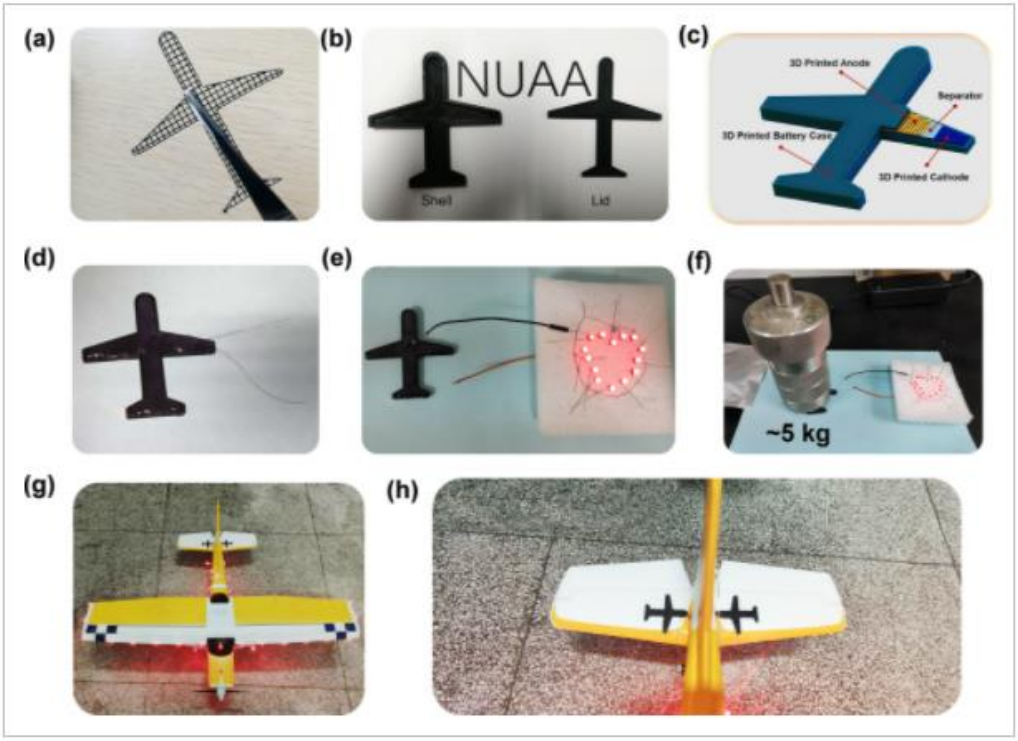

Figure 2-22: Model plane used to incorporate a printed battery a) The 3D LNMO cathode. b) The 3D printed battery case by using a fused deposition 3D printer. c) The inner structure diagram of the 3D plane battery. d) The photo of the assembled 3D plane battery. e, f) The 3D plane battery with LED lights at a weight of about 5 kg. g, h) Two 3D plane-shape batteries assembled on aircraft models, providing electrical power for the aircraft lighting system [101].

3.0 Experimental Approach

This thesis introduces the investigation of metalizing fabricated 3D printed shape memory polymer antenna via electroplating technique. The project utilized additive manufacturing, SLA vat photopolymerization technology, and the help of features and parameters, material mixing adjustment to obtain the optimal printing of SPMs. Later, SMPs are utilized to fabricate antennas. The fabricated SMP antennas undergo ideal mechanical, electrical, and chemical characterization.

Likewise, the development of the 3D-printed lithium-ion battery was investigated in this paper. The battery was printed and post-processed using DLP 3D technology and lithium iron phosphate materials. Following the creation of the LiFePO4 electrode, the electrode was sintered and characterized to navigate the optimal battery performance.

3.1 Materials

3.1.1 Shape Memory Polymer

A commercially available Clear photopolymer resin (RS-F2-GPCL-04) manufactured by Formlabs was utilized as the base material for this investigation. The system displayed a brittle behavior at room temperature, with low recovery fixity as demonstrated by Cersoli et al [102] [103]. To reduce the brittleness of the Clear resin materials, Elastic photopolymer resin (RS-F2-ELCL-01), was also manufactured by Formlabs and blended with Clear resin to modify its brittle behavior. Five resin mixtures with different mass fraction ratios of Elastic materials in the range from 0 (100% Clear resin) to 0.4 (60% Clear resin, 40% Elastic) were mixed with a laboratory stand mixer for 5 minutes and placed in an ultrasonic device at 40°C for 60 minutes. The Clear-Elastic resin blend was then printed using a Form2 SLA 3D printer (Formlab printer). The profile for the printed part was prepared using the SolidWorks computer designing software. The printer was operated on "open mode" and had a layer height of 100 um. After the printing process was completed, the printed parts were washed in isopropyl alcohol (IPA) for ten minutes and then placed in an ultraviolet curing chamber made by Formlabs at 60°C for 20 minutes. Furthermore, the copper dispositioning begins by soaking the 3D printed SMPs in a bath of isopropyl alcohol (240g) and graphite powder (1.5g) mix for 24 hours. The parts are removed and set aside to dry. In the case of selective copper deposition, the desired section of the 3D printed SMPs is coated with a Graphite Conductive Ink base, commercially available, purchased from Working Ink, UK [104]. In the case of full-parts copper deposition, the 3D printed parts are fully coated with Graphite Conductive Ink. Then, the graphite-coated part is placed in an electroplating solution to deposit copper in the

coated area. The electroplating solution consists of 7g of H2SO4, 40g of copper sulfate, and 200 ml of deionized water. The 3D printed SMPs part is connected to a DC power supply at 0.2 V and 0.1 A for 2 hours or until the part is fully copper-coated. Figure 3-1 shows a schematic electroplating process used in this work. Figure 3-2 shows the dispositioning copper steps followed in this research program.

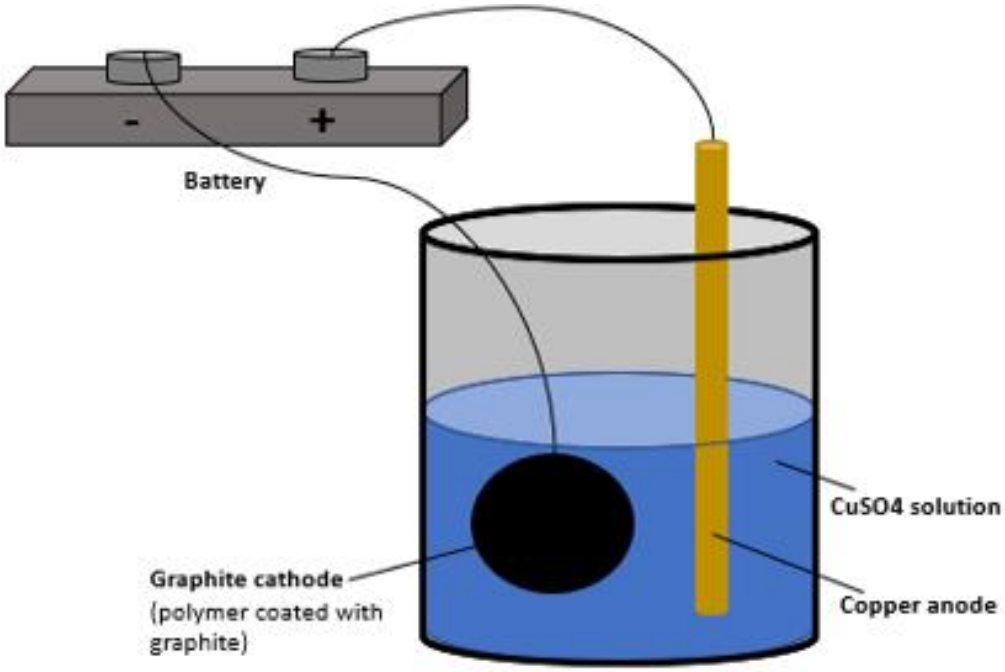

Figure 3-1: demonstration of the electroplating process.

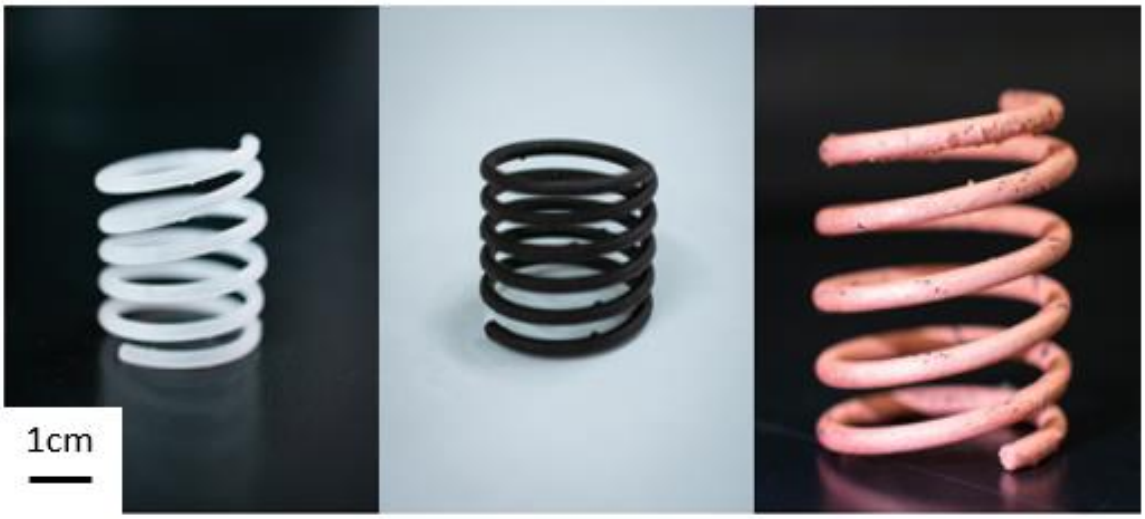

Figure 3-2: 3D printed parts used in the work for investigating the copper electroplating process in both selective and complete methods. The as-printed shape memory polymer (left), the conductive coating applied only to a spiral pattern on the part (middle), and the copper traces after electroplating the ink (right).

For this thesis, both a dipole and helical antenna were 3D printed using the Clear-Elastic resin blend (80%w Clear -20%w Elastic). This ratio was selected based on a previous work performed by Cersoli et al [102], who studied thermal and mechanical analysis of this blend. The dipole antenna was selectively coppered, whereas the helical antenna was completely copper-coated (see Figure 3-3).

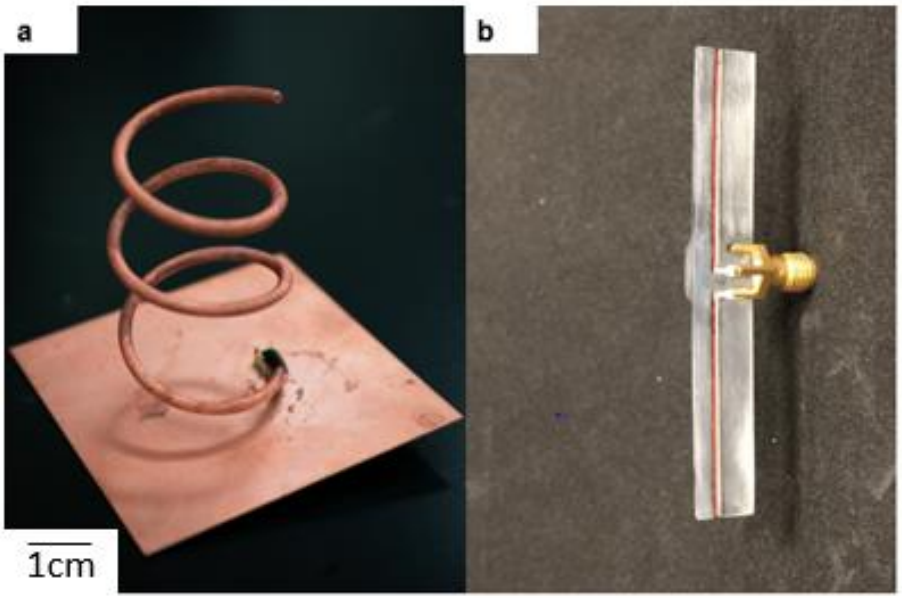

Figure 3-3: copper-plated SMPs antenna (a) complete surface. (b) selective copper plated trace.

3.1.2 3D Printed Battery

Considering the development of lithium-ion batteries, a photopolymer UV curing Genesis resin, manufactured by Tethon 3D, was used as a base material [105,106]. To develop an electrochemical energy storage system, a lithium iron phosphate (LiFePO4) powder (particle size 1.5 μm) and Conductive Graphite (TIMCAL KS-6) (particle size 3.4 μm) were purchased from MSE Supplies and were blended to 3D printing resin [107]. The cathode resin consisted of a ratio of 60g of the Genesis resin, 36.36g of LiFePO4, and 3.64g of Conductive Graphite. The anode resin consisted of 90% Genesis resin and 10% Conductive Graphite. Both electrodes were mixed for 10 minutes using a laboratory stand mixer and were placed in a rolling machine for 24 hours at room temperature. Next, this mixture of battery electrodes was printed on the Admaflex DLP (Digital Light Processing) printer. The electrodes were printed in a disc shape using a layer thickness of 10 μm. The 3D-printed disc shapes were designed using the SolidWorks software (see Figure 3-4).

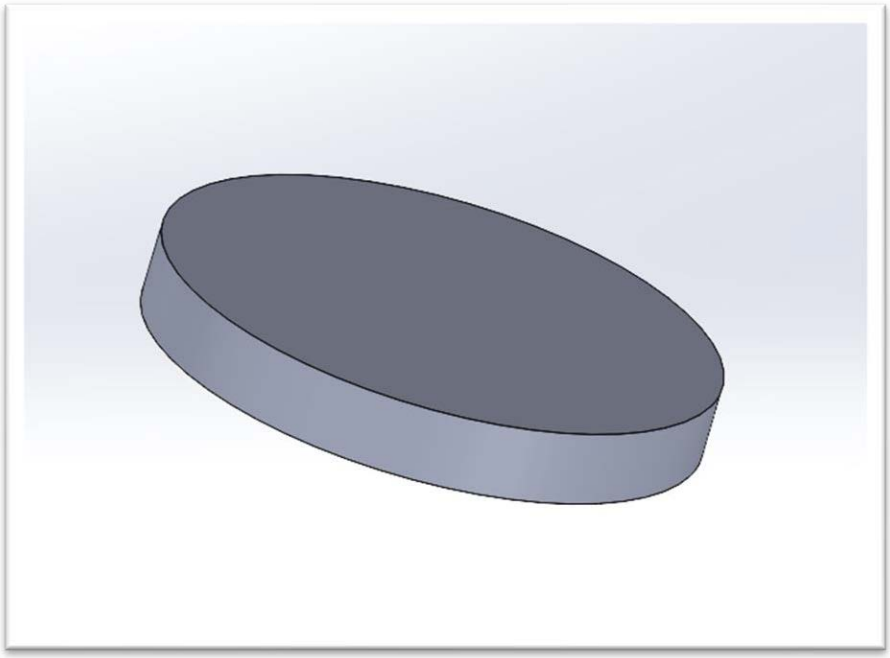

Figure 3-4: Lithium Iron Phosphate SolidWorks Design.

The Admaflex-130 printing parameters were adjusted accordingly to conduct a precise printing process for differently sized 3D-printed parts. Once the electrodes were printed and removed from the build platform, they were cleaned using 75% alcohol wipes and water. Subsequently, the printed discs were weighed, and dimensions were taken.

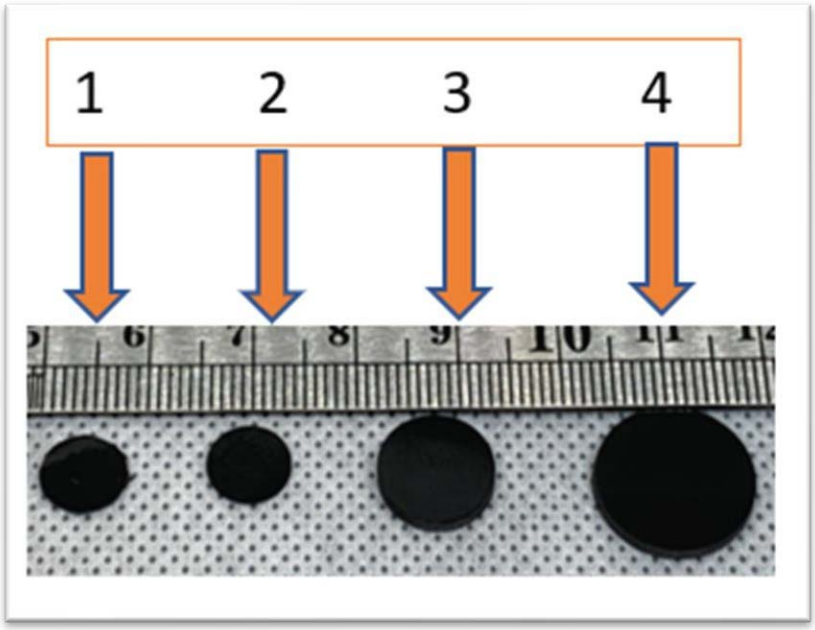

Figure 3-5: 3D printed green state disc-shaped electrodes.

The electrodes were placed into a programable tube furnace and sintered to form a solid mass of materials and to enhance the mechanical, thermal, and electrical properties through heat. The sintering profile involves a ramp of 0.96°C/min up to 150°C, followed by a hearing ramp of 0.0387°C/min up to 320°C. At 320°C, the furnace dwelled for four hours. After this dwelling temperature, the furnace was ramped at a rate of 0.99°C/min up to 400 °C and kept at this temperature for 10 hrs. Then, it was ramped at 1.02°C/min up to 500°C and then at a rate of 2.1°C/min up to 850 °C, where it was kept for 2 hours. Finally, the furnace was left to cool down naturally to room temperature (Figure 3-6 shows the post-thermal profile used on the printed parts).

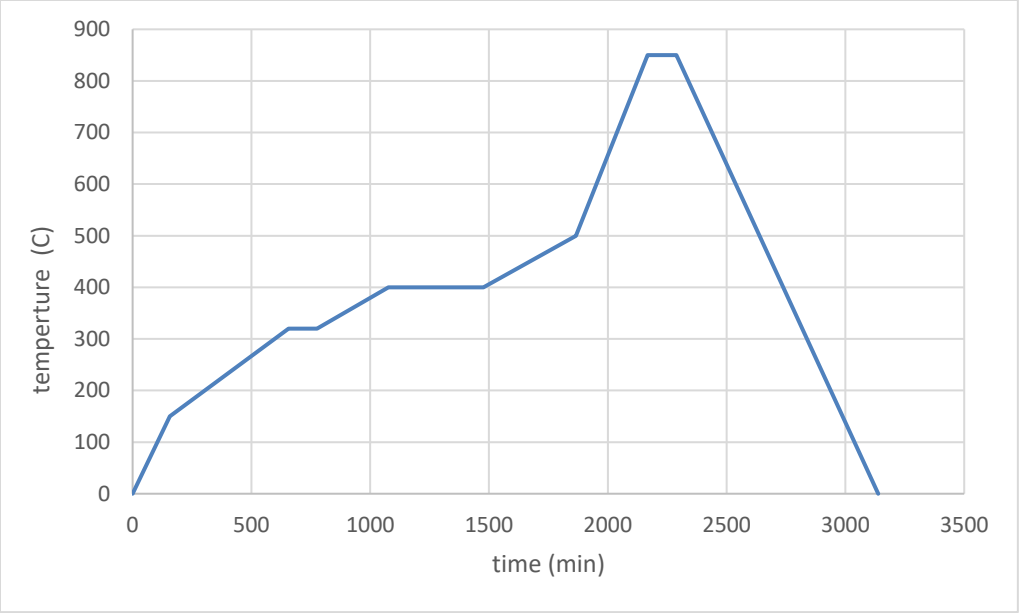

Figure 3-6: Sintering profile for DLP battery electrodes printed on Admaflex-130.

The electrodes were weighed and measured after sintering for shrinkage studies. Table (2) shows the shrinkage of four samples printed in different thicknesses, diameters, and weights. The 3D-printed LiFePO4 samples experienced shrinkage of 12-25% on the thickness coordination and 16-27.5 % on the diameter coordination. Also, the LiFePO4 experienced 47.9-62.4 % weight loss during the sintering process. Furthermore, advanced thermal and chemical characterization techniques were performed to evaluate the electrodes' quality. Finally, electrodes were assembled into a cell and tested for electrochemical energy and cycling using Gamry-interface 5000E coordination.

Table 2: Geometrical and electrical evaluation of the printed LiFePO4 material.

	Sample 1				Sample 2				Sample 3				Sample 4			
	Before	After	Shrinkage (%)	Weight lost(%)	Before	After	Shrinkage(%)	Weight lost(%)	Before	After	Shrinkage(%)	Weight lost(%)	Before	After	Shrinkage(%)	Weight lost(%)
Thinckness (mm)	0.2	0.15	25		0.6	0.44	26.6		2	1.76	12		2.1	1.77	15.7	
Diameter (mm)	8.02	6.7	16.4		8.03	5.82	27.5		8.03	6.26	22.04		12.38	10.36	16.3	
Weight (g)	0.0173	0.009	X	47.9	0.046	0.017	X	62.4	0.156	0.055	X	65	0.3819	0.1707	X	55.3

3.2 4 Point Probs Test

A four-point probe test was applied to the copper-coated 3D-printed SMPs to measure the sheet resistance. The part was placed on a platform of the Niko Eclipse ME600 inspection microscope. Four probes with equal spaces were placed in contact with copper-coated SMPs. ADC current was applied to the part using a Signatone S-300 4-point probes device, here, the current was applied to the printed electrode between the outer two probes, and a digital multimeter Keithley 2410 SMU measured the voltage difference between the inner two probes. The following equation was used to determine the sheet resistance of the copper coated SMPs

$$\rho S = \frac{V}{I} 4.534\ [\Omega.\text{sq}] \qquad (1)$$

The battery electrodes also were tested for sheet resistance. Four-point probes were applied to the 3D-printed electrodes. The electrodes were positioned on the platform of the Signatone S-300 4-point probe device. The sheet resistance of the battery electrode was calculated using equation (1).

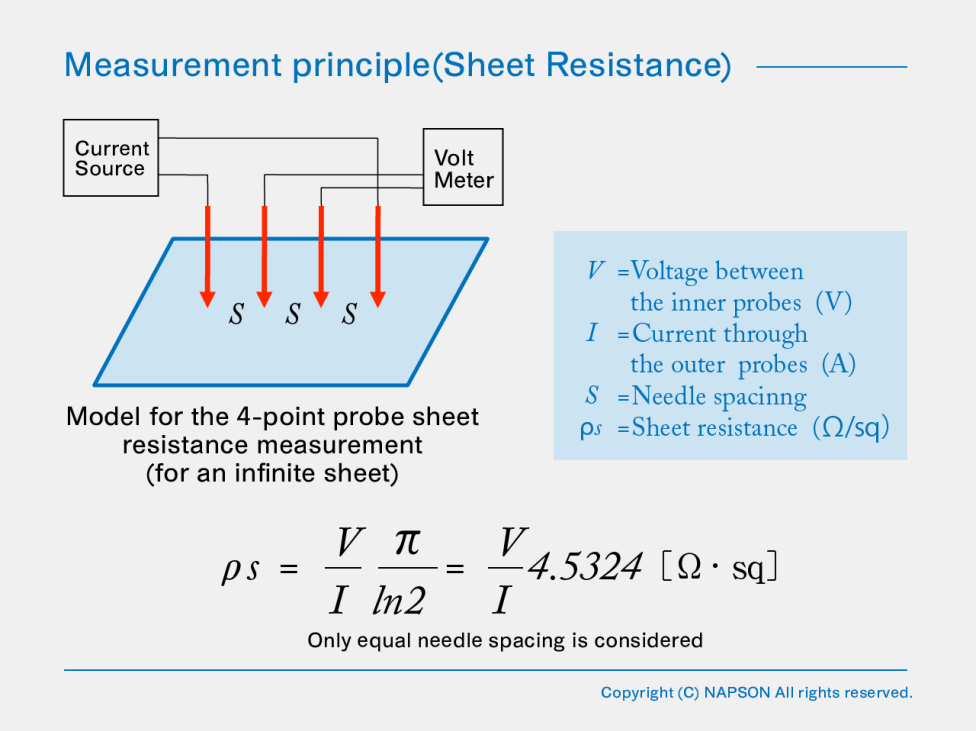

Figure 3-7: Schematic of sheet resistance measuring principle [108].

3.3 Optical Microscope

The copper-plated SMPs underwent a surface evaluation test using advanced optical microscopy. A rectangular copper-plated SMPs was placed on the microscope's platform to create magnified images to get a closer view of the copper layers.

The 3D-printed electrodes were set on a platform of a digital microscope (Keyence VHX-5000). Images with various magnifications were taken before and after the sintering process.

3.4 Scanning Electron Microscopy (SEM)

An SEM instrument was used to produce a large magnification image using an electron beam source. An electron beam is produced at the top of the microscope by the electron gun source. The electrons follow a vertical direction throughout aligned lenses. The beam travels through the electromagnetic field and lenses, which forces the beam toward the substrate. The beam hits the substrate and electrons, and X-rays are ejected from the substrate. A detector collects the backscattered and secondary electrons and converts

them to various signals containing information that then sends them to a screen to produce an image (see Figure3-8) [109].

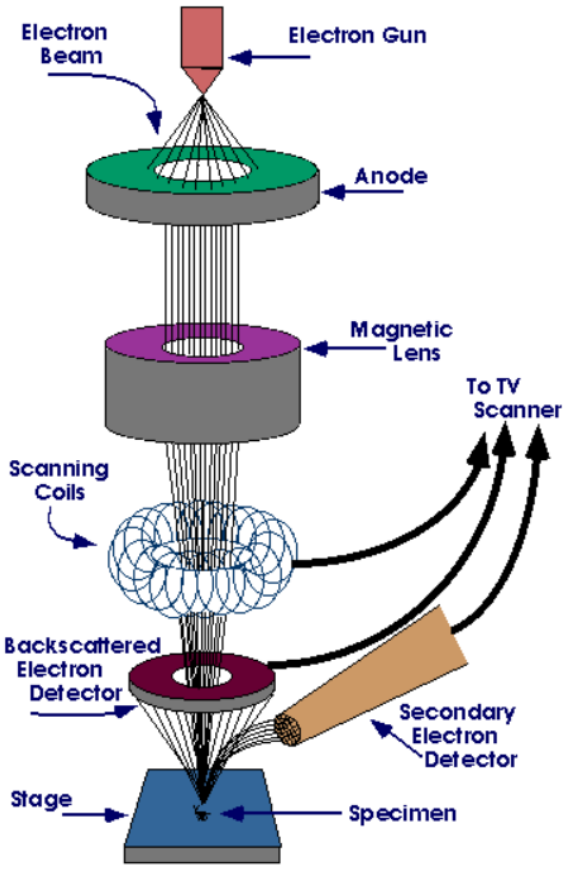

Figure 3-8: Schematic of SEM mechanism [109].

To investigate the microstructure and the chemistry of copperplated SMPs, a Scanning Electron Microscopy (SEM) analysis was utilized. The graphite coated SMPs was investigated under an SEM (Keysight technology 8500 FE-SEM) to evaluate the graphite adhesion onto the surface of the SMP substrate. Once the graphite-coated SMPs substrate is copper-coated using the electrolysis techniques, the surface of the copper-coated SMPs was evaluated using SEM analysis to determine the copper's topography and composition (see Figure 3-9).

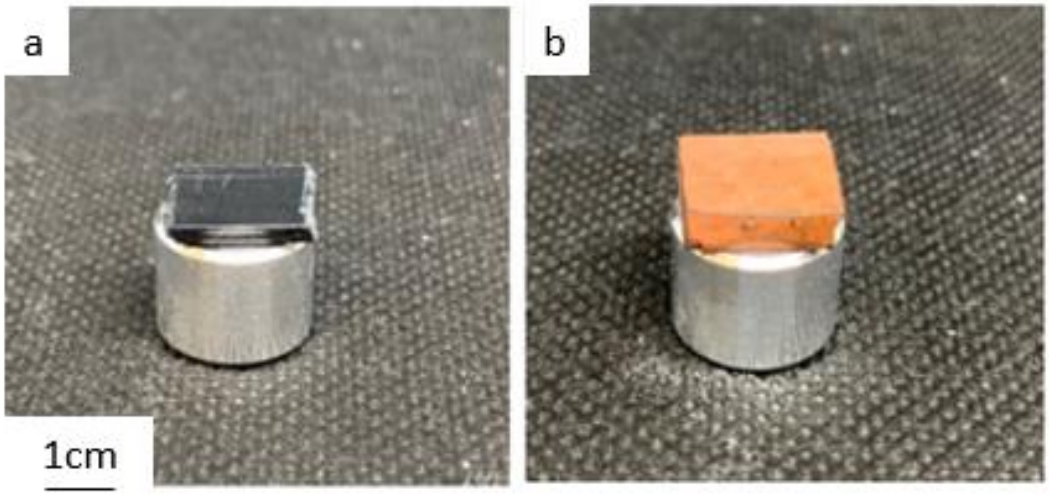

Figure 3-9: Sample used on an SEM analysis (a) graphite conductive ink coated and (b) copper-plated shape-memory substrate in the SEM's holder.

As stated, the 3D-printed electrodes were observed under SEM in both the green and sintered states to evaluate the printing quality. In the case of the green state, the electrodes were prepared by attaching the copper film to the surface of the electrodes (see Figure 3-10 a&b). The sintered electrodes were placed on sample holders and scanned to investigate the microstructure of solid electrodes (see Figure c&d).

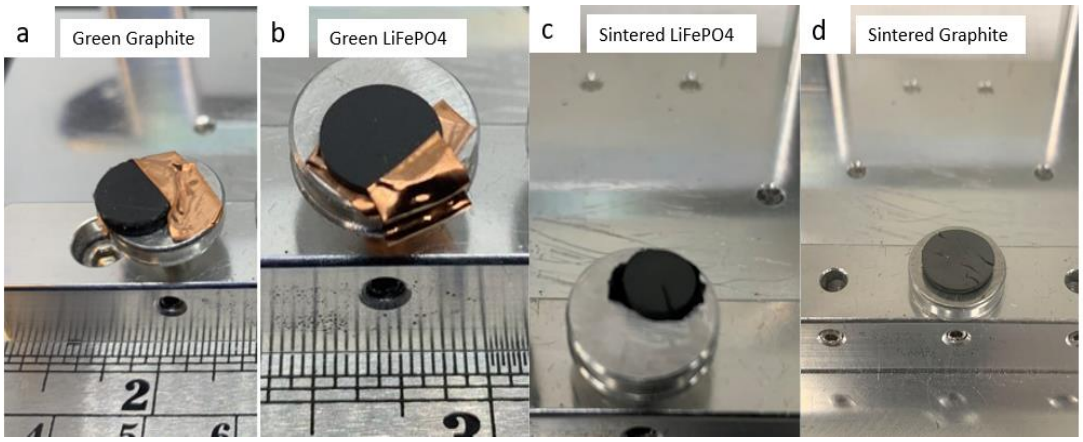

Figure 3-10: green state (a) graphite anode and (b) lithium iron phosphate placed in the SEM holder. Sintered (c) lithium iron phosphate cathode (d) conductive graphite anode placed in the SEM holder.

3.5 Energy Dispersive Spectroscopy (EDS), Thermogravimetric analysis (TGA), and X-Ray Diffraction (XRD)

Energy dispersive X-ray (ESD) techniques were performed on the copper-plated 3D SMPs for elemental and chemical characterization using a Keysight technology 8500 FE-SEM. The SMPs sample was prepared and positioned in an EDS holder. Here, an energy of 12 keV EDS source was used on the samples. The EDS measures the energy and electron beam intensity distribution of X-ray signals hitting the surface of the sample [110]. Elements were selected from the periodic table to detect and identify elemental counts.

The battery electrodes were also subjected to an EDS analysis to quantify their composition. Additionally, the lithium-ion phosphate was subjected to a charging and discharging process. A leading energy value of 5 keV was dispersed into the graphite electrode sample

The 3D printed battery electrodes underwent a thermal decomposition analysis using thermogravimetric analysis (Hi-Rec TGA-2950 instrument) in nitrogen. The TGA temperature was programmed to reach up to 1000°C following a ramping rate of 10°C/min and a dwelling time of 5min at 1000°C. From this test, the number of inorganic solids on the electrode was calculated based on a mass balance.

To identify the crystalline phase of the 3D printed electrodes, X-ray diffraction (XRD) analysis was implemented in a Rigaku MiniFlex). Here, the sintered LiFePO4 and graphite were grinded to a micron and nanoparticles size powder using mortar and pestle. Then, the electrode powder was placed into an XRD powder holder (see Figure 3-11). Finally, the electrodes were analyzed for 12 hours to identify the crystalline phase present in the electrodes and compare the resulting information to the received material.

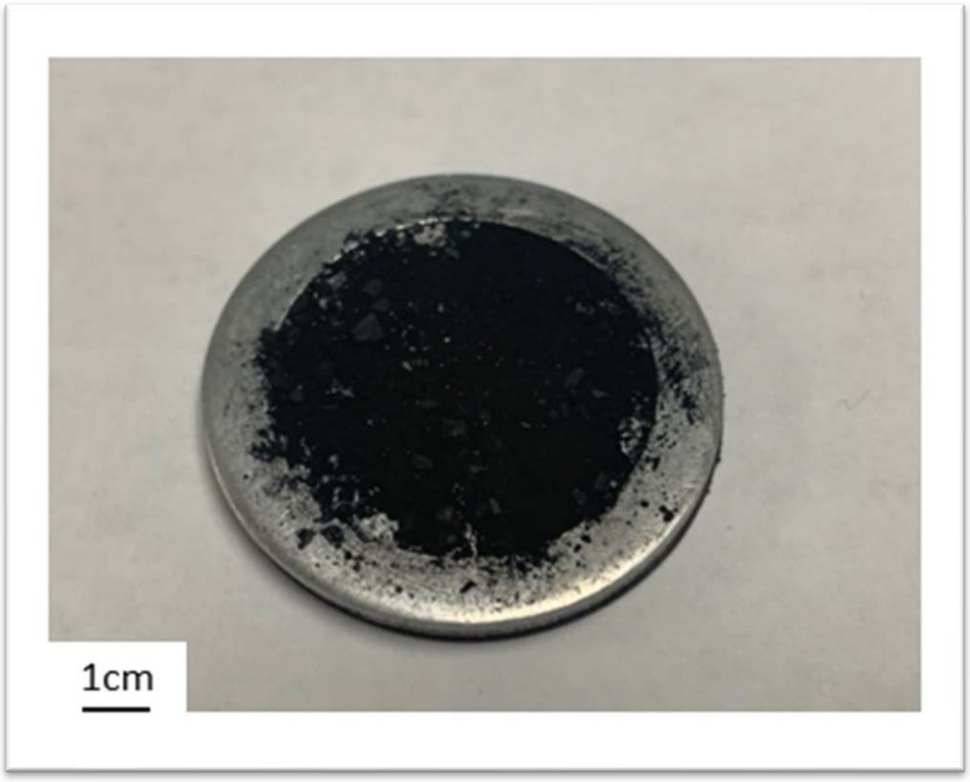

Figure 3-11: shows a grinded sintered LiFePO4 substrate in an XRD powder holder.

3.6 Characterization Methodology

3.6.1 High-Frequency Simulation Software (HFSS) For Shape Memory Polymer

To first examine the functionality of the fabricated 3-D printed antennas. The copper-plated dipole and helical antennas were tested using a Vector Network Analyzer (VNA) to measure their gain over frequency range by elucidating their S_{11} parameter under 1-port analysis. The 3D- printed antennas were connected to a 50-ohm coaxial SMA connector attached to VNA. The printed antenna was subsequently simulated using the High-Frequency Simulation Software (HFSS). Here the antenna was simulated in its permanent and temporary shape following a thermo-mechanical cycle.

3.6.2 Battery Cycling

To determine the electrochemical energy performance of the battery electrode, a cyclic charge/discharge test was conducted using the Interface 5000E from Gramry Instrument). The 3D printed lithium iron phosphate and graphite discs were inserted into the electrode holder. Then, the holders were connected to electrochemical cells. An electrolyte lithium hexafluorophosphate was poured into the cell using a glove bag. The glove bag was connected to an argon gas tank to avoid electrolyte chemical reactions. LiFePO4 was considered as the working electrode, whereas graphite was the counter electrode (see figure 3-12). Additionally, the electrodes were tested in a full and half-cell configuration by incorporating a reference electrode (Saturated Calomel Electrode). Gamry instrument Framwork was utilized to monitor and control electrodes' static charge/discharge settings.

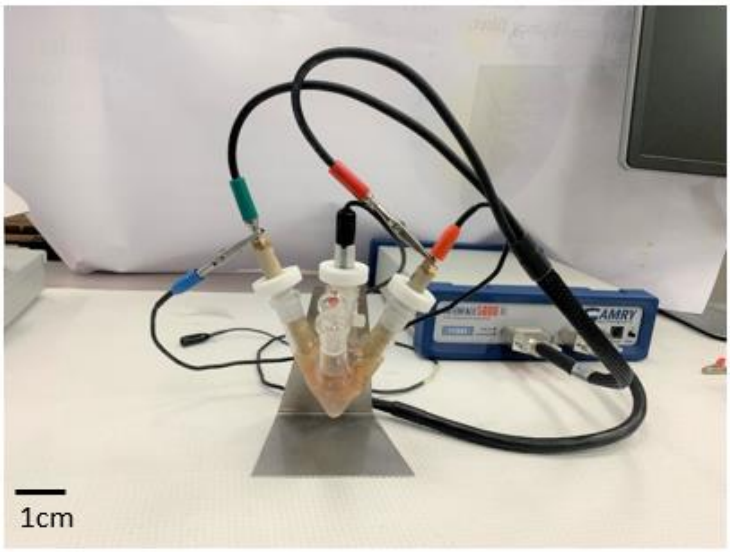

Figure 3-12: Photo of the electrochemical cell used in this work.

4.0 Results and Discussion

This section presents the electrical, physical, and chemical results obtained on the copper-plated SMPs as well as on the printed electrodes, in addition, this section will discuss the functionality of the fabricated 3D printed dipole and helical antennas. Furthermore, this section discusses the battery electrode outcomes encountered in this work.

4.1 Shape Memory Polymer

4.1.1 *Electrical characterization of plates materials*

To determine the sheet resistance and the bulk resistivity of the thin layer of copper-plated SMPs, a 4-point probes test was here used. The 4-probes were placed at an equal adjusted distance on the surface of the copper-plated substrate. Gradually, a current flow between 10-100 mA was applied to the substrate to measure the sheet resistance using equation (3-1). It was found that the copper-plated SMPs exhibited a sheet resistance of 0.2845 Ω/sq. Additionally, the SEM analysis showed that the thickness of the copper coated on the SMP surface was around ~1μm (see Figure 4-1). The SMPs exhibited a bulk resistivity of 2.845×10^{-7} Ω·m for the copper layer which compared to a pure copper bulk resistivity of 1.71×10^{-8} Ω.m [111].

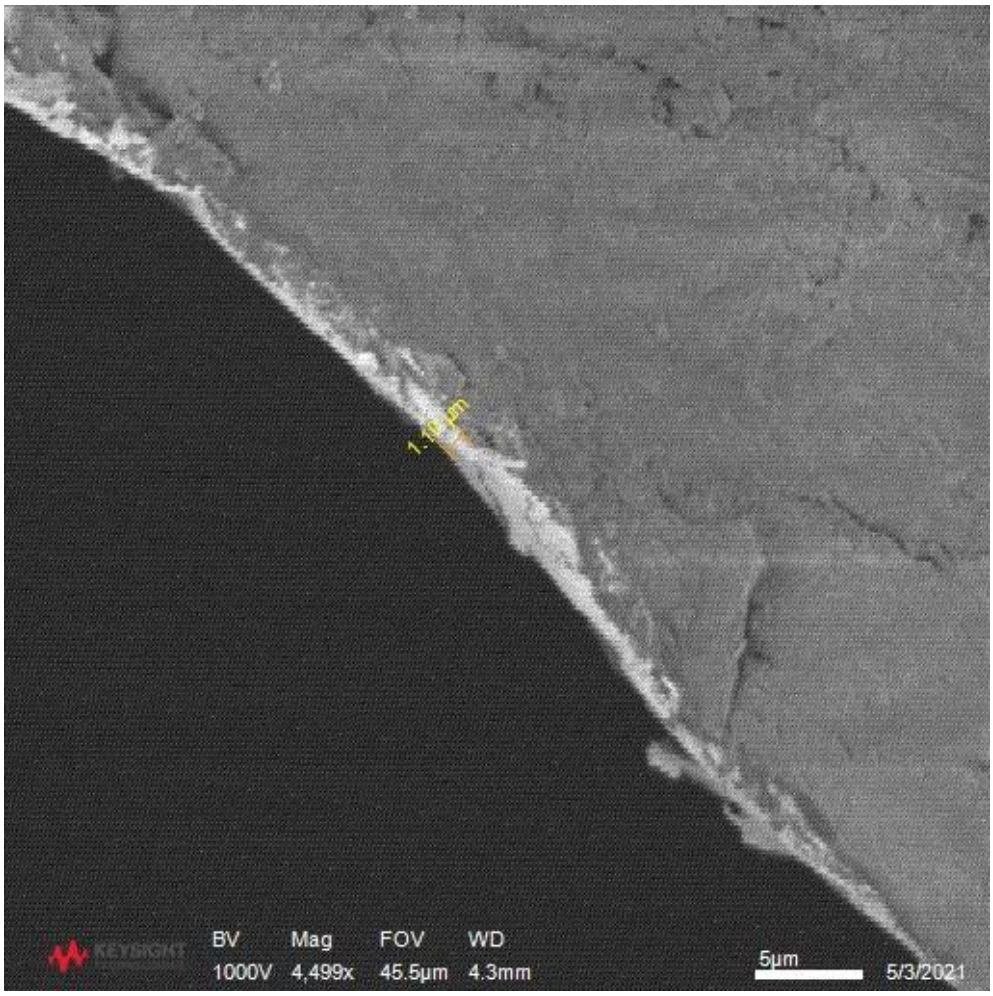

Figure 4-1: SEM image of the cross-section of the copper-plated SMPs.

4.1.2 Optical Microscope

After the printing, the SMPs were soaked in a bath of isopropyl alcohol and graphite powder for 24 hours, and the constructed SMPs were coated with liquid graphite conductive ink on the surface. Optical images show the conductive ink with adequate wetting and coverage on the surface (see Figure 4-2).

Figure 4-2: Optical image for the graphite-coated SMPs.

4.1.3 SEM

A high magnification SEM image was conducted on the graphite-coated SMP. The image shows the graphite ink particles filling the porous surface of the SMPs, which assists the copper plating process. (see Figure 4-3).

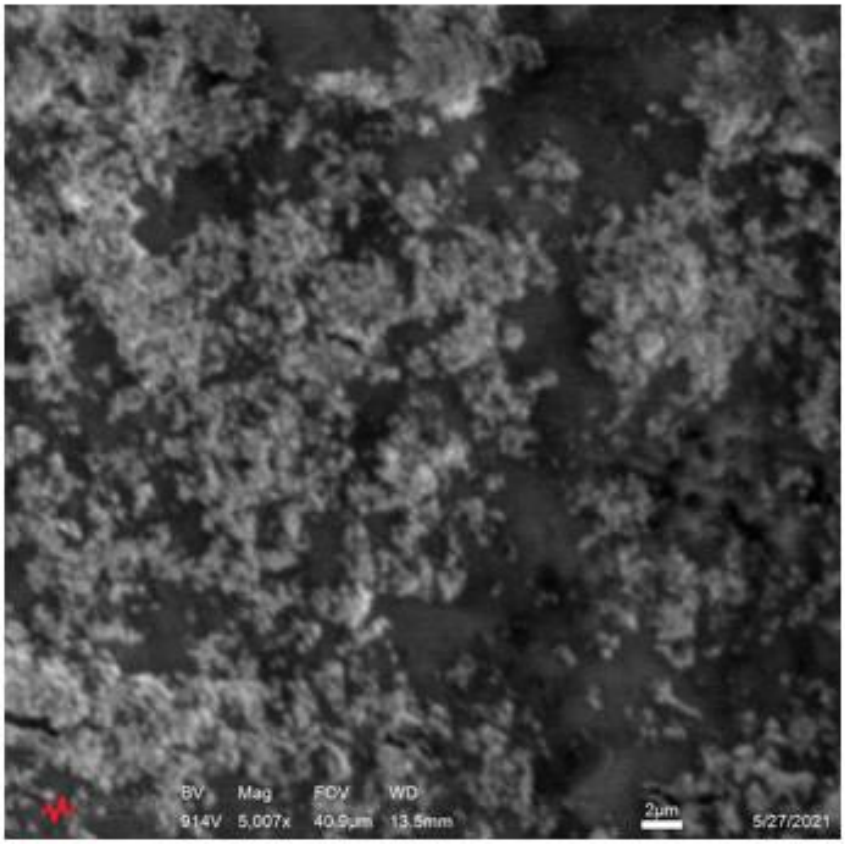

Figure 4-3: SEM image of the graphite-coated SMPs.

To evaluate the quality of the surface structure of the copper layer, an SEM analysis was performed. SEM micrographs were taken of the copper-plated SMPs. It was observed that spherical copper particles of different sizes (indicated by red arrows) were accumulated upon the surface of the graphite-coated SMP to form a copper layer (see Figure 4-4).

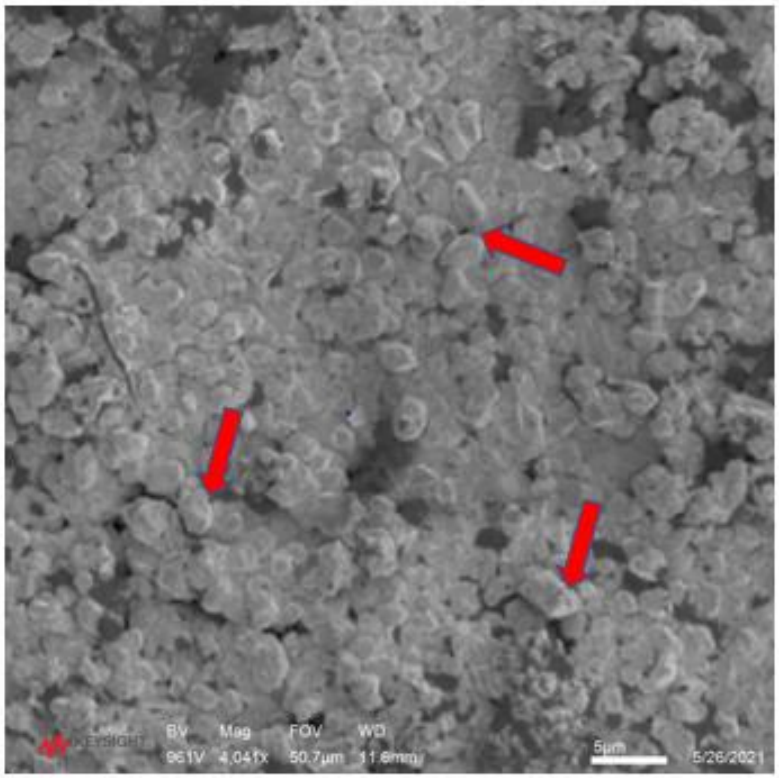

Figure 4-4: SEM image at high magnification of the copper-plated SMPs.

4.1.4 EDS

Energy-dispersive X-ray microanalysis (EDS) was used on different areas of the copper-plated SMPs substrate to confirm the existence of the copper element on the surface of SMPs. The ESD analysis shows approximately 92.5% of copper on the printed parts with the remaining 7% being carbon and oxygen. (See Figure 4-5).

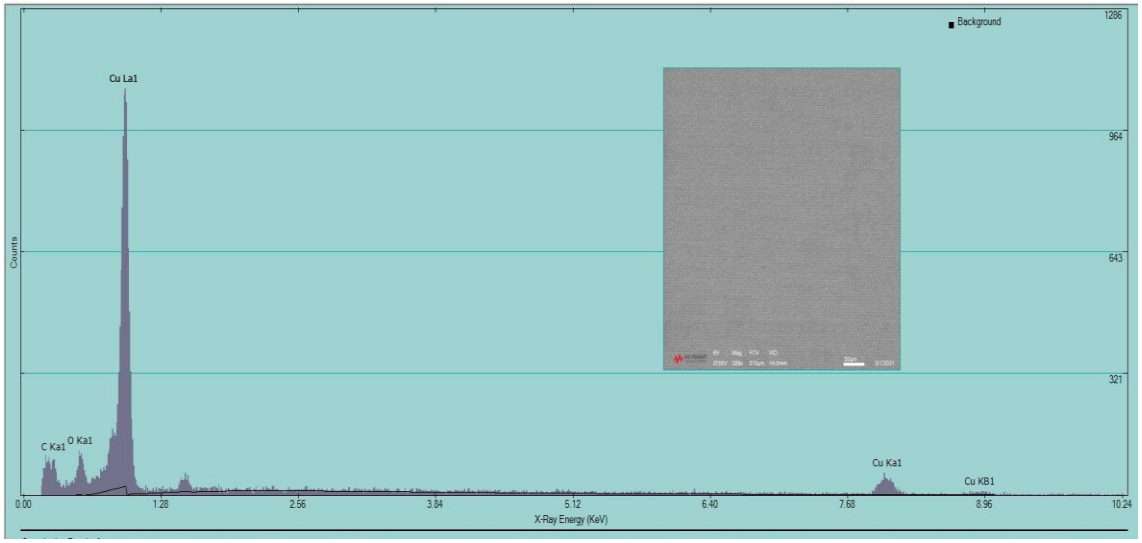

Figure 4-5: EDS of the copperplated SMP substrate.

4.1.5 Functional Antennas

To examine the functionality of metallization of 3D printed SMPs, A dipole antenna was 3D printed and copper-plated via electrolysis technique. First, a dipole was fabricated using the SLA printing technique. Second, the fabricated antenna's trace was selectively copper plated utilizing the electrolysis technique. The antenna was deformed into a semicircle with different radiuses (R=12.7mm and R=19.1mm) to examine the morphological behaviors of the metalized SMPs (see Figure 4-6). Following the production of the dipole system, a helical system was manufactured, copper-coated, and tested.

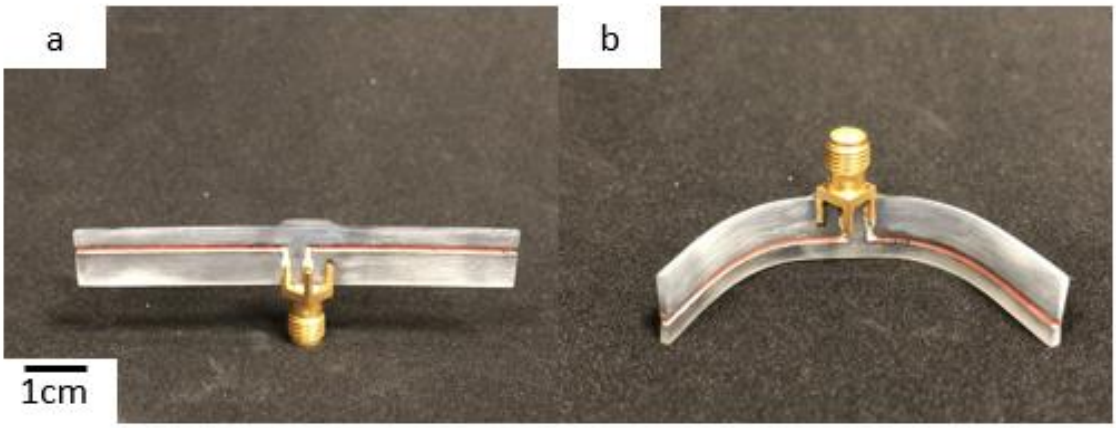

Figure 4-6: Selectively copper plated antenna (a) the dipole antenna in a straight configuration and (b) the dipole antenna in semicircle configuration.

Here the fabricated antenna was connected to a coaxial connector using a flat sheet of copper as a ground plane. The antenna was heated to enter the rubbery phase and deformed and cooled to keep it in the temporary shape. (see Figure 4-7). The additional thermal process resulted in the antenna returning to its original state. A VNA testing was carried out on the antenna in the permanent and temporary shape.

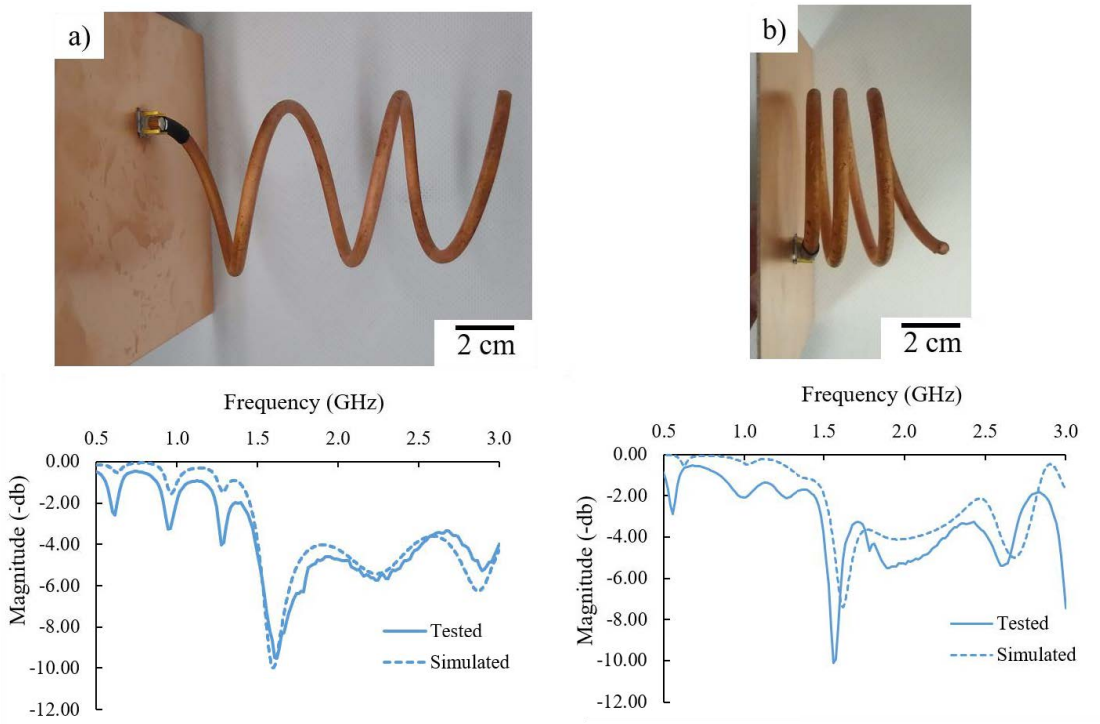

Figure 4-7: Copper-plated SMP helical antenna. (a) the helical antenna with the full length of 100 mm (b) compressed helical antenna with a length of 40 mm. The S11 parameter plots vs simulation are shown below each helical antenna.

The helical antenna was also simulated and compared to the measured S_{11} parameters. The antenna is modeled as a bulk copper surface, 30 micrometers thick surrounding a dielectric core. Though the thickness of the conductive coating in the simulation is several skin depths for bulk copper at 1.5 GHz, significant inaccuracy in resonant frequency was not observed in the temporary part geometry of figure 4-7a. A narrowing of the resonance peak was observed at 1.6 GHz and a more uniform rejection was observed below 1.5 GHz. Inaccuracy in the return loss of the fixed antenna of figure 4-7b can be attributed to slight variations in the geometry of the simulation relative to the final part. This can cause a mismatch in the attenuation of the current distribution at the feed point between the simulated and tested cases.

4.2 3D Printed Battery Components

4.2.1 4 Point Probs

A four-point probe was employed on the battery electrodes to determine the sheet resistance. Regarding the LiFePO4/C (cathode), a current between $5x10^{-6}$_ $1x10^{-4}$ A was applied to measure the voltage of the LiFePO4/C (see Figure 4-8). It was found that the sheet resistance of the LiFePO4 disc is $2.7x10^{-4}$ Ω/sq. Knowing the thickness of the LiFePO4 sample is $8.8x10^{-4}$m, it resulted in a bulk resistivity of $2.376x10^{-7}$Ω.m, which represents a value 101.01 lower than the reported on LFePO4/Carbon (101.10 Ω.m) by 99.9% [112]. Indeed, it is worth mentioning that the bulk resistivity reported by 99.9% is based on a system containing 10 % of carbon.

A 4 four-point probe testing was also performed on the graphite (anode) to measure its sheet resistance. Here, a current of $5x10^{-6}$_$1x10^{-4}$A was used between the probes to measure the voltage (see Figure 4-9). The sheet resistance of the graphite disc was calculated to be $9.41x10^{1}$ Ω/sq. The thickness of the graphite electrode is $8.2x10^{-4}$m, which results in a bulk resistivity of $7.49x10^{-2}$Ω.m, which does not compare favorably to the bulk resistivity of natural graphite is $9x10^{-6}$Ω.m [113].

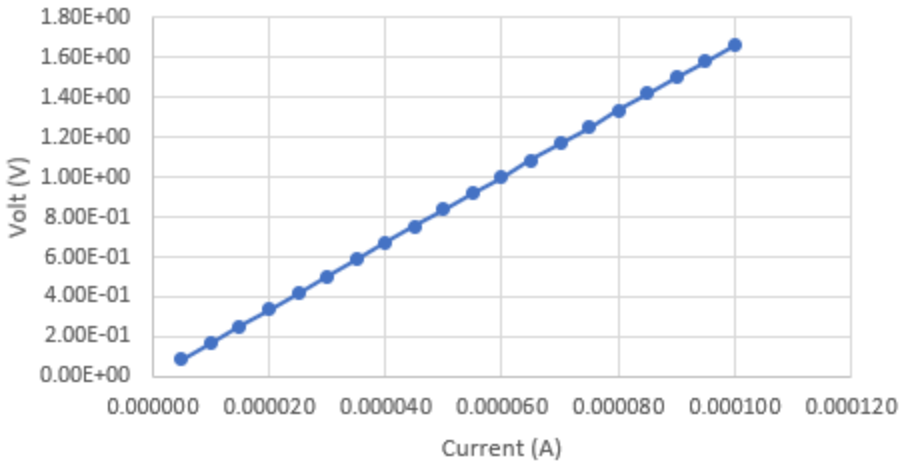

Figure 4-8: The current vs volt of LiFePO4 sample to measure sheet resistivity.

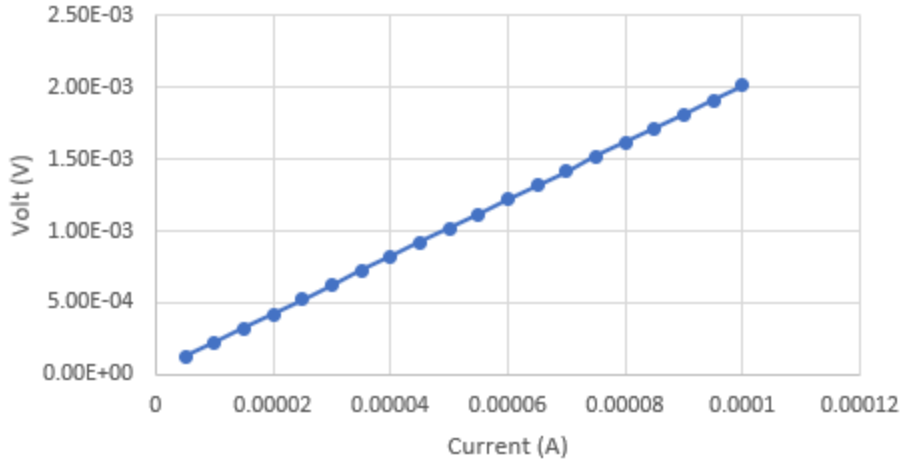

Figure 4-9: The current vs volt of LiFePO4 sample to measure sheet resistivity.

4.2.2 Optical Microscope

An optical microscope analysis was performed on the surface of the electrode in the green state, and after sintering it to characterize their surface details. The optical images were at various magnifications. The optical images show a successful printing process of the battery electrode discs (see figure 4-10a). The optical images show a smooth surface of the green state LiFePO4 (cathode). Figure 4-10 also shows the optical images of the graphite (anode) in the green state. The graphite exhibited a fine surface after the printing process.

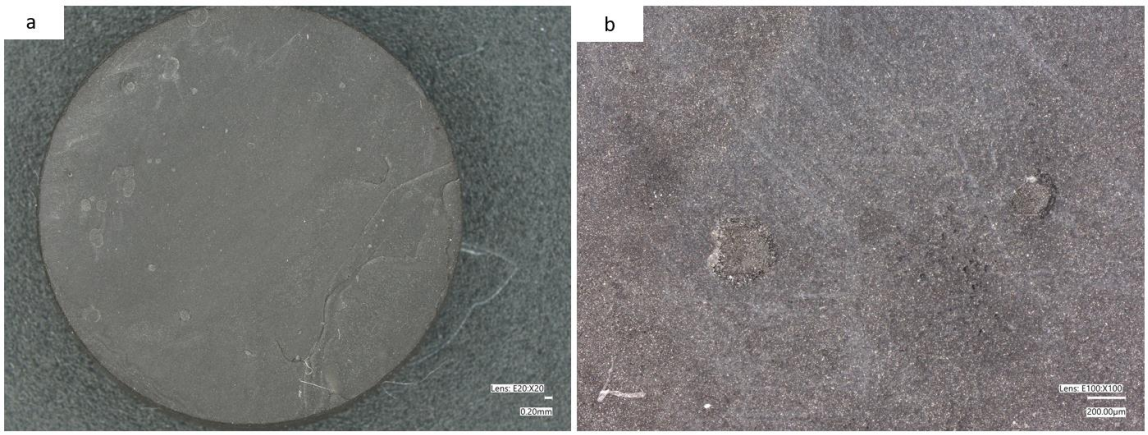

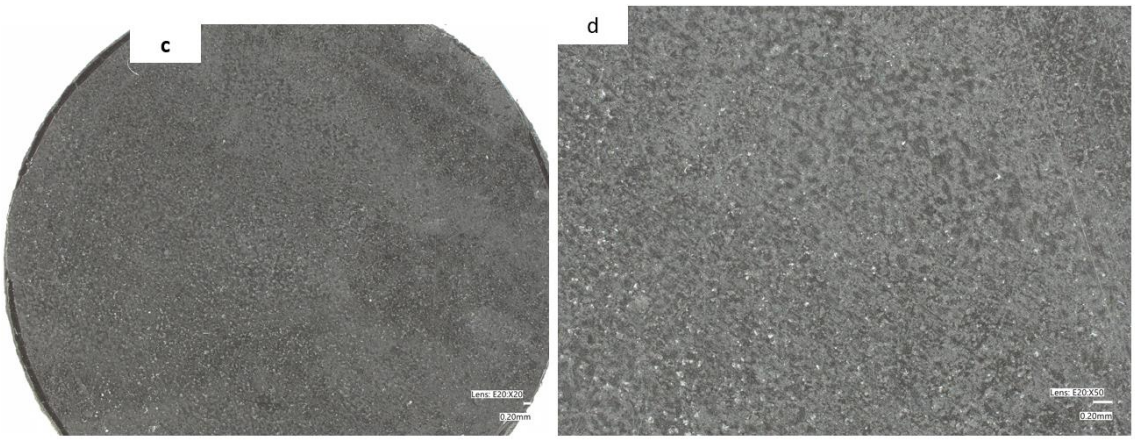

Figure 4-10: Optical images of LiFePO4 (cathode) in the green state (a) low magnification and (b) high magnification. Optical images of graphite (anode) in the green state (c) low magnification and (d) high magnification

An optical analysis was also applied to the electrode samples after the sintering process. Figures 4-11a&b) show large cracks across the sample (indicated by the yellow and blue arrows) which are associated with the coefficient of thermal expansion and shrinking mechanisms of the parts during the thermal treatment. The side of LiFePO4 was also observed after performing the sintering process indicated by the blue arrow (see Figure 4-11b). It is worth mentioning that although the parts displayed large cracks, they were mechanically strong. Similarly, the sintered graphite electrode was observed under the optical microscope. The sintered graphite electrode exhibited long cracks propagated in various locations indicated by the red arrow (see Figure 4-11 c&d).

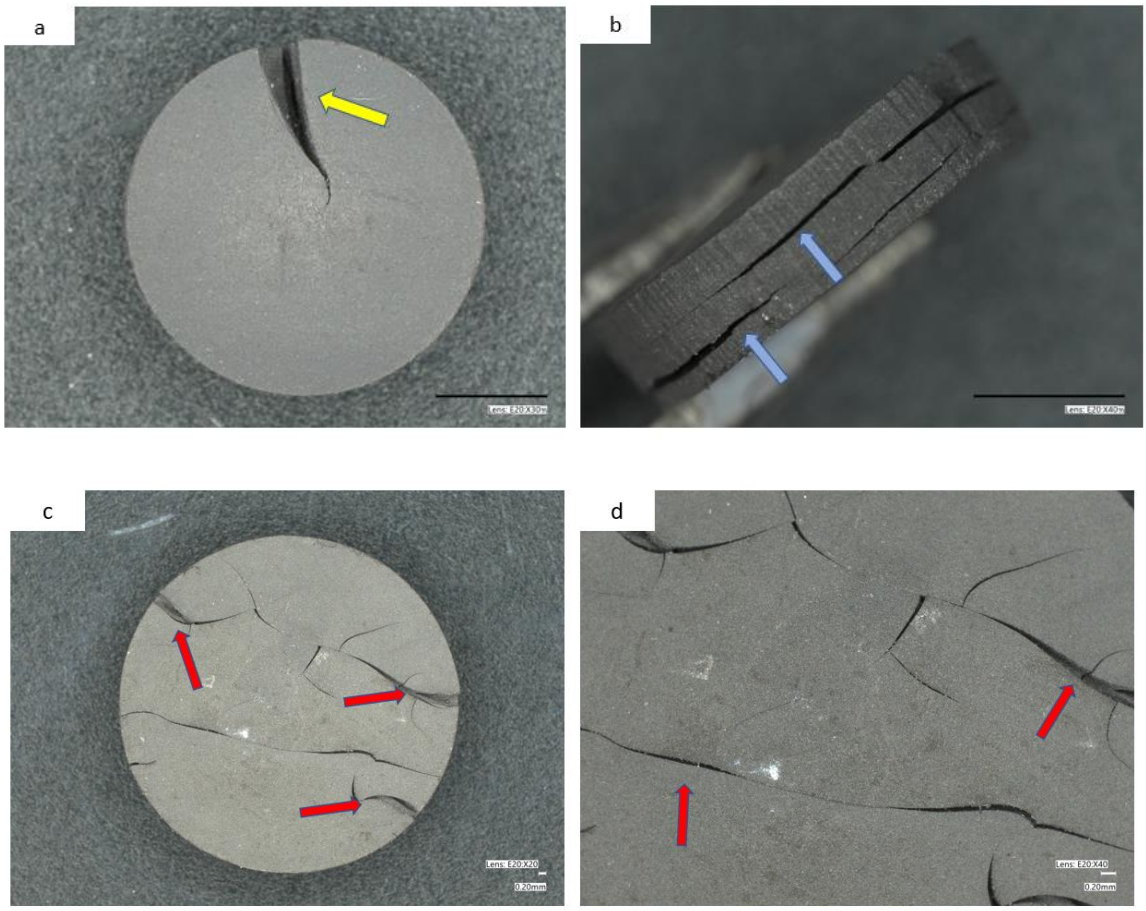

Figure 4-11: Optical images of the sintered samples. LiFePO4 (cathode) (a) surface and (b) side images. Graphite (c) surface and (d) side view.

4.2.3 TGA

The 3-D printed electrodes were investigated using a TGA (Thermogravimetric analysis) to measure the change in the physical-chemical properties of electrodes at elevated temperatures (see figure 4-12). The TGA was utilized to measure the decomposition weight loss (%) of an electrode blend consisting of Lithium (36.36g), Graphite (3.64g), and Genesis resin (60g) versus temperature. Three samples were run for statistical analysis. The TGA showed that the Genesis rein started to decompose at a temperature of about 200°C, and remained to drop until it was mostly decomposed at 500°C. At 850°C, which is the dwelling temperature for the actual sintering process,

59.28% of the sample was decomposed (associated with the Genesis resin). This resulted in a residue of40.82% which represents the remaining LiFePO4+ Graphite (solid) phase. The residual 0.82% solid could be related to the deposition of carbon from the Genesis resin. Similarly, the genesis resin and graphite (anode) blend underwent a TGA analysis. The fabricated anode resin consisted of graphite powder (10 %) and genesis resin (90%). The TGA shows a remaining active graphite material weight of 10.92%.

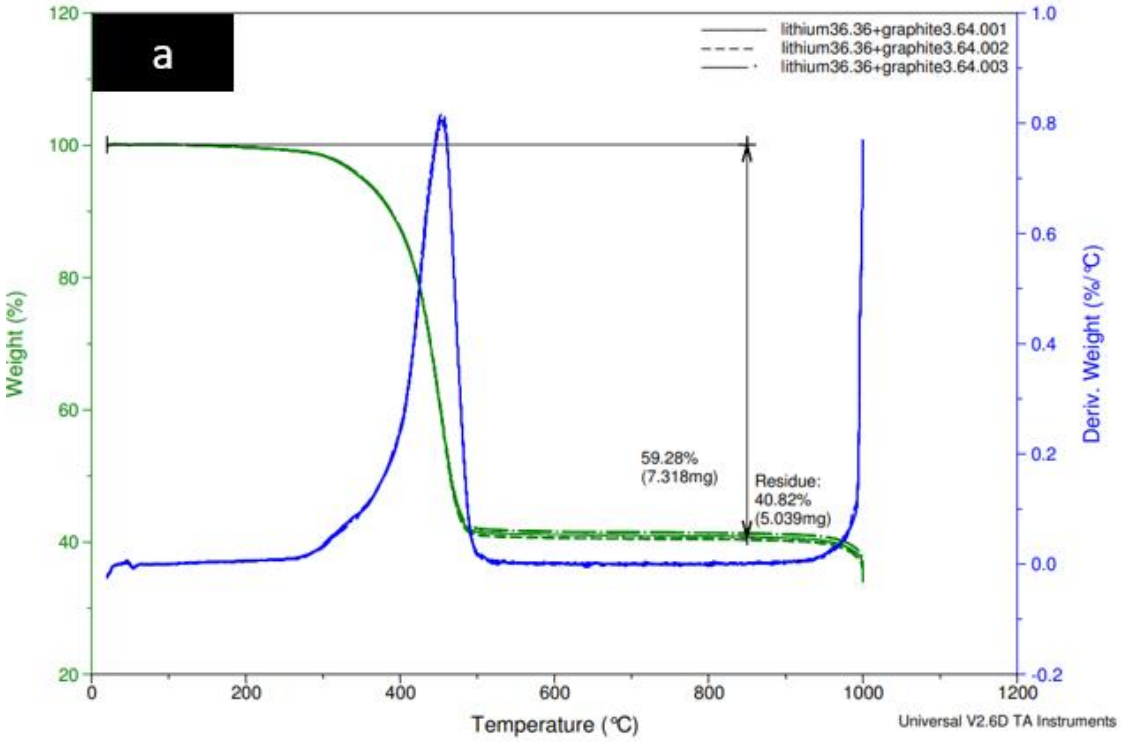

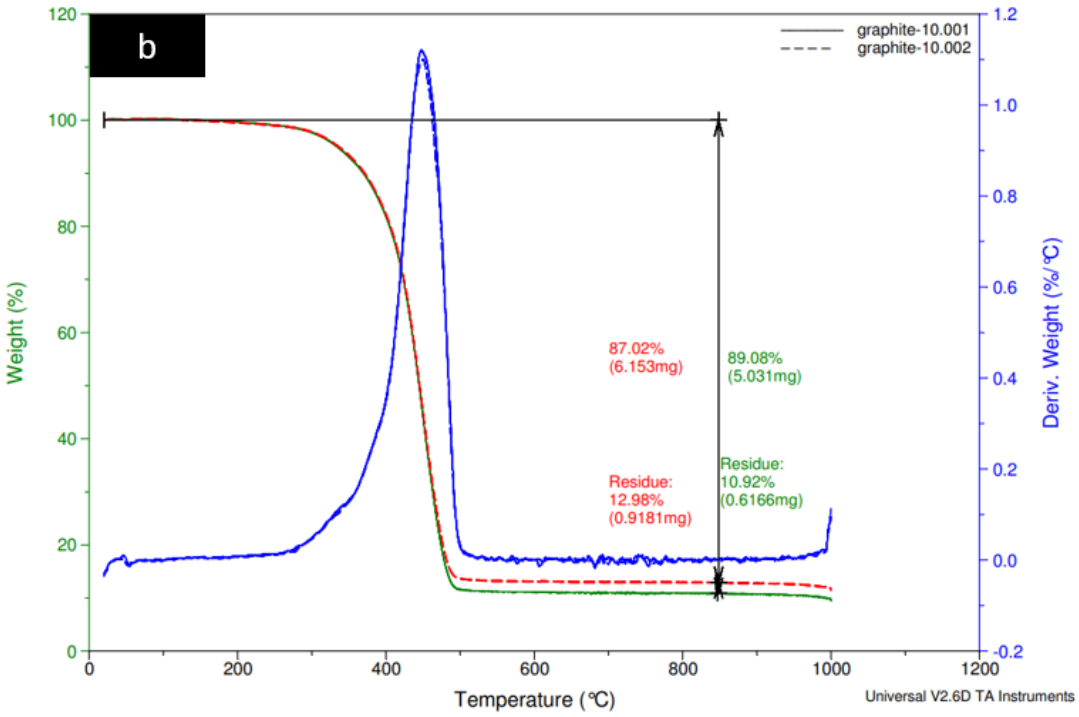

Figure 4-12: TGA analysis of (a) LiFePO4, and (b) graphite with Genesis resin composites.

4.2.4 SEM

An SEM analysis was carried out on the sintered electrodes. In addition to the aforementioned cracks, it was found that the LiFePO4 particles are mostly fused (see figure 4-13 a-c). The graphite (anode) also shows cracks as well as a considerable amount of fused particles (see figure 4-13 f)

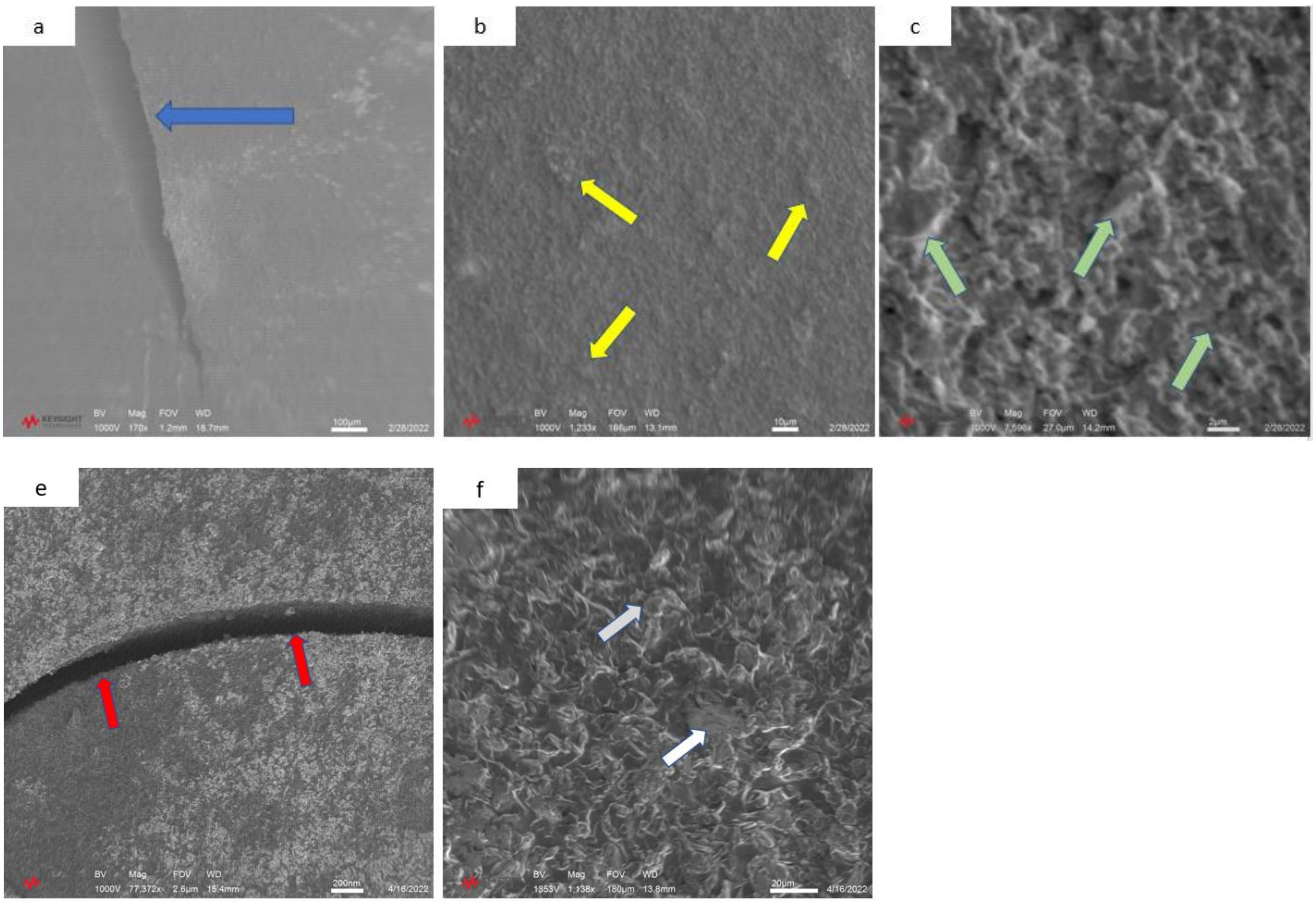

Figure 4-13: SEM images for the sintered electrode.

4.2.5 XRD

The crystallinity of the composite of lithium iron phosphate and graphite electrode was examined by an X-ray diffraction technique (XRD) (see Figure 4-14). The received LiFePO4was also examined to compare and establish control. Comparing the sintered and the received material it seems that the XRD shows the presence of LiFePO4 as well as the peaks related to carbon. Comparable results have been observed by Xiaoli xi et al [114]. Indeed, the LiFePO4 and peaks seem to fit with those shown by the as-received control. Similarly, the graphite peaks appear to match those displayed by the as-received graphite material peaks.

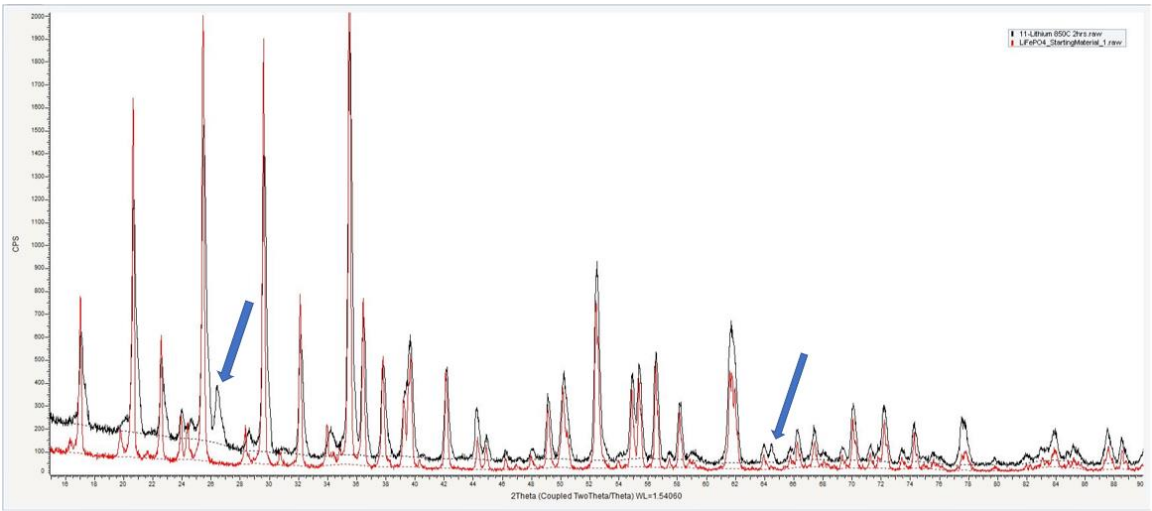

Figure 4-14: XRD analysis comparing both sintered and as-received material LiFePO4

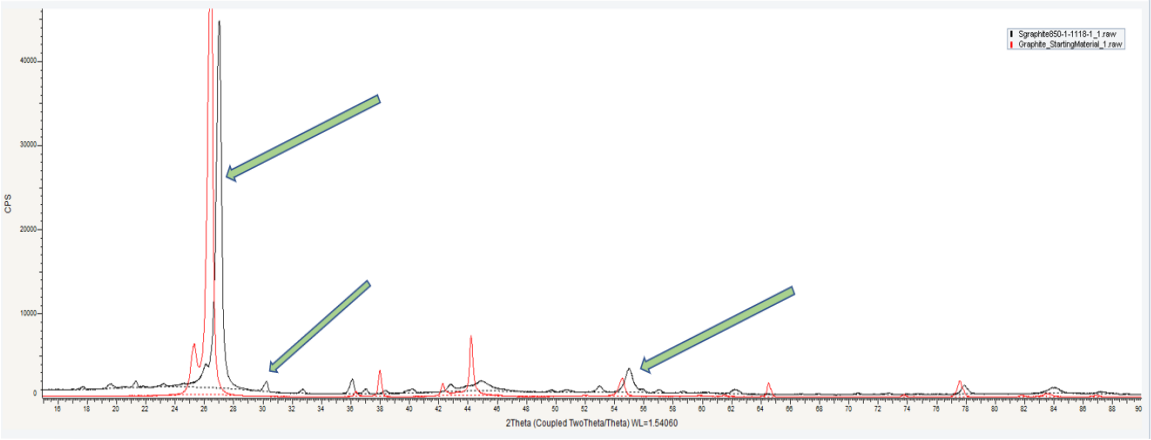

Figure 4-15: XRD analysis for conductive graphite, comparing both sintered and as-received material.

4.2.6 Electrochemical characterization

The battery was charged at a constant current rate of 500 µA. For a typical Lithium-ion battery, the voltage limits ranged from 3.0 V ≤ V ≤ 4.2 V. The computed charge capacity of the battery was determined to be 30 µA-hr. Figure 4-16a shows the charging curve of the battery.

Furthermore, the cell was discharged at 5 µA see figure 4-16b. As soon as the charging current was stopped, there was an instantaneous drop to 1.3V from the upper limit of the potential was observed. This massive drop is due to the structure change of the graphite anode during the sintering process (see Figure 4-15 XRD). Moreover, the computed capacity of the battery after discharge was found to be almost 7 nA-hr.

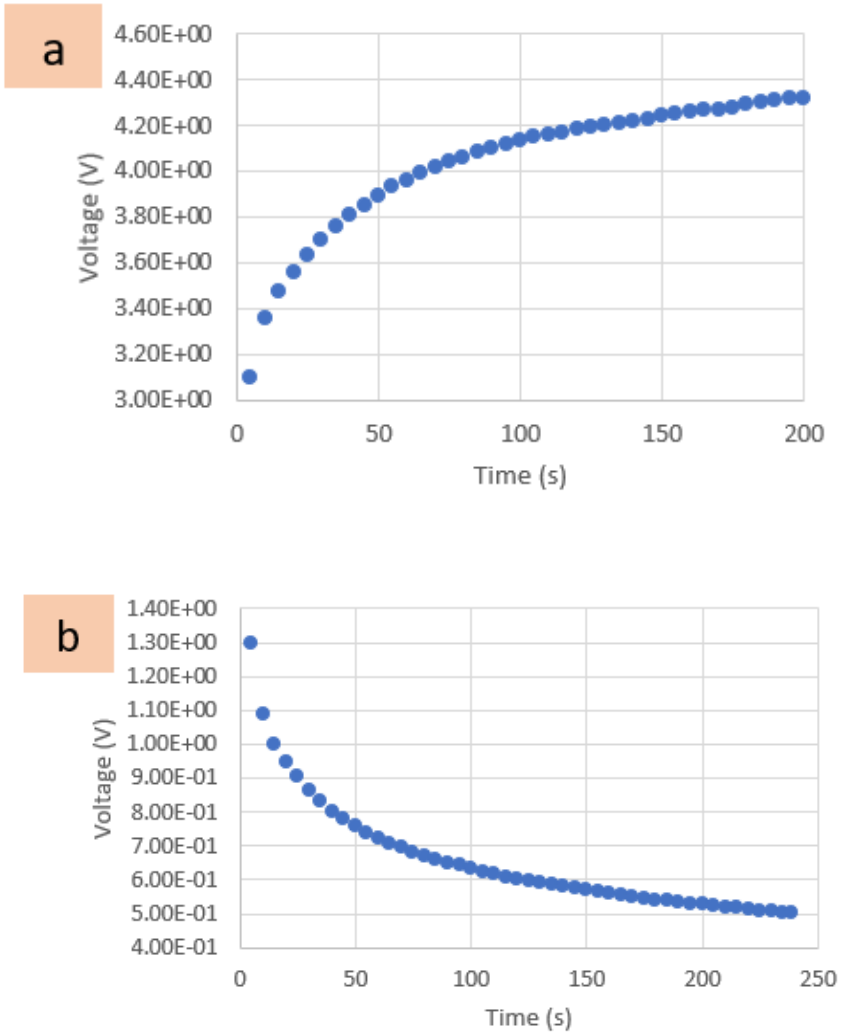

Figure 4-16: Charging and discharging profiles of the 3D printed LiFePO4 samples

5.0 Conclusions

This work presented the metallization of a shape memory polymer and the development of 3D printed lithium batteries. The first work investigated the electroplating of a 4D printed functional antenna via electrolysis technique. Additionally, electrical and chemical characterization methods were applied to quantify the metal coating. The second work investigated the creation of a 3D printed lithium battery component via DPL. The lithium battery components underwent various material characterization techniques.

The following points have been identified as the main outcomes of this work.

SMP:

1. The incorporation of a conductive graphite ink on the 3D printed parts acted as an efficient coating film for subsequent metallization stages.
2. The electrolysis technique showed a successful path for coating copper on printed SMPs while maintaining a morphological behavior.
3. The 4- Point probes technique yielded a sheet resistance of 0.2845 Ω/sq on the electroplated copper layer. In addition, copper layer thickness was found to be ~1μm using SEM cross-sectional images. Here, the SMPs exhibited a bulk resistivity of 2.845 x 10^{-7} Ω·m.
4. A helical antenna was printed as well as coated with copper, and it was observed that it displayed a clear shape memory effect. The antenna was subjected to VNA testing and an HFSS_simulation process. The results showed a relatively good simulation profile in the temporary and permanent stages of the SMP.

3D printed electrodes for batteries

The SEM analysis showed that although the sintered printed electrodes displayed some cracks on the parts, the particles seemed to have yielded a high degree of inter-diffusion. The TGA showed that they applied to the battery electrodes to measure the weight loss (%) of electrode material blend when exposed to a heat source. Lithium iron phosphate/carbon (cathode) had experienced a residue of 40.82% of solids, while

at 850°C which is the amount of active material that the cathode blend started with before sintering. Graphite (anode) exhibited 10.92% of carbon (solids) was determined on the sintered graphite printed anode. reside material which represents the amount of graphite active material.

5. The crystallinity of the sintered lithium iron phosphate/carbon using XRD resulted in good agreement with the spectra obtained from the as-received material.
6. The electrochemical profile of the printed anode and cathode showed that while the charging profile displayed a charging capacity of 30 μA-hr on the cathode, the anode experienced a sudden voltage drop from4.2V to 1.3V. The battery was discharged at 5 μA, and the computed capacity was found to be 7 nA-hr.
7. This project was the initial step towards the printing process of LiFePO4 via DLP. A considerable number of modifications, optimization, and studies need to be performed to provide a proper 3D printed battery.

References

1. Su M, Song Y. Printable Smart Materials and Devices: Strategies and Applications. Chem Rev. 2021. doi:10.1021/acs.chemrev.1c00303

2. Mrinalini M, Prasanthkumar S. Recent Advances on Stimuli-Responsive Smart Materials and their Applications. Chempluschem. 2019;84: 1103–1121.

3. Leo DJ. Engineering Analysis of Smart Material Systems. John Wiley & Sons; 2007.

4. Melly SK, Liu L, Liu Y, Leng J. Active composites based on shape memory polymers: overview, fabrication methods, applications, and future prospects. J Mater Sci. 2020;55: 10975–11051.

5. Leng J, Lan X, Liu Y, Du S. Shape-memory polymers and their composites: Stimulus methods and applications. Prog Mater Sci. 2011;56: 1077–1135.

6. Kamila S. Introduction, classification and applications of smart materials: an overview. American Journal of Applied Sciences. 2013;10: 876.

7. Zarek M, Layani M, Cooperstein I, Sachyani E, Cohn D, Magdassi S. 3D Printing of Shape Memory Polymers for Flexible Electronic Devices. Adv Mater. 2016;28: 4449–4454.

8. Brennan M. Suite of shape-memory polymers. Chem Eng News. 2001;79: 5–5.

9. Monkman GJ, Taylor PM. Memory foams for robot grippers. Fifth International Conference on Advanced Robotics 'Robots in Unstructured Environments. 1991. pp. 339–342 vol.1.

10. Takashima K, Rossiter J, Mukai T. McKibben artificial muscle using shape-memory polymer. Sens Actuators A Phys. 2010;164: 116–124.

11. Callister WD. (WCS)Materials Science and Engineering: An Introduction, 7th Edition Binder Ready Version. John Wiley & Sons Canada, Limited; 2007.

12. Liu Y, Du H, Liu L, Leng J. Shape memory polymers and their composites in aerospace applications: a review. Smart Mater Struct. 2014;23: 023001.

13. Santo L, Quadrini F, Accettura A, Villadei W. Shape Memory Composites for Self-deployable Structures in Aerospace Applications. Procedia Engineering. 2014;88: 42–47.

14. Lin C, Lv J, Li Y, Zhang F, Li J, Liu Y, et al. 4D-printed biodegradable and remotely controllable shape memory occlusion devices. Adv Funct Mater. 2019;29: 1906569.

15. Daver F, Baez E, Shanks RA, Brandt M. Conductive polyolefin–rubber nanocomposites with carbon nanotubes. Composites Part A: Applied Science and Manufacturing. 2016. pp. 13–20. doi:10.1016/j.compositesa.2015.10.002

16. Chizari K, Arjmand M, Liu Z, Sundararaj U, Therriault D. Three-dimensional printing of highly conductive polymer nanocomposites for EMI shielding applications. Materials Today Communications. 2017;11: 112–118.

17. Gnanasekaran K, Heijmans T, van Bennekom S, Woldhuis H, Wijnia S, de With G, et al. 3D printing of CNT- and graphene-based conductive polymer nanocomposites by fused deposition modeling. Applied Materials Today. 2017;9: 21–28.

18. Su X, Li X, Ong CYA, Herng TS, Wang Y, Peng E, et al. Metallization of 3D Printed Polymers and Their Application as a Fully Functional Water-Splitting System. Adv Sci Lett. 2019;6: 1801670.

19. Bernasconi R, Credi C, Tironi M, Levi M, Magagnin L. Electroless Metallization of Stereolithographic Photocurable Resins for 3D Printing of Functional Microdevices. J Electrochem Soc. 2017;164: B3059.

20. Zhan J, Tamura T, Li X, Ma Z, Sone M, Yoshino M, et al. Metal-plastic hybrid 3D printing using catalyst-loaded filament and electroless plating. Additive Manufacturing. 2020;36: 101556.

21. Lee S, Wajahat M, Kim JH, Pyo J, Chang WS, Cho SH, et al. Electroless Deposition-Assisted 3D Printing of Micro Circuitries for Structural Electronics. ACS Appl Mater Interfaces. 2019;11: 7123–7130.

22. Angel K, Tsang HH, Bedair SS, Smith GL, Lazarus N. Selective electroplating of 3D printed parts. Additive Manufacturing. 2018. pp. 164–172. doi:10.1016/j.addma.2018.01.006

23. Shape Memory Polymers: Properties, production, types, uses, examples. In: Nanografi Nano Technology [Internet]. [cited 24 Jan 2022]. Available: https://nanografi.com/blog/shape-memory-polymers-properties-production-types-uses-examples/

24. Hyun WJ, Thomas CM, Hersam MC. Nanocomposite ionogel electrolytes for solid-state rechargeable batteries. Adv Energy Mater. 2020;10: 2002135.

25. Li M, Lu J, Chen Z, Amine K. 30 years of lithium-ion batteries. Adv Mater. 2018;30: e1800561.

26. The Four Components of a Li-ion Battery. [cited 12 Apr 2022]. Available: https://www.samsungsdi.com/column/technology/detail/55272.html

27. Diouf B, Pode R. Potential of lithium-ion batteries in renewable energy. Renewable Energy. 2015;76: 375–380.

28. Saevarsdottir G, Tao P-C, Stefansson H, Harvey W. Potential use of geothermal energy sources for the production of lithium-ion batteries. Renewable Energy. 2014. pp. 17–22. doi:10.1016/j.renene.2012.04.028

29. Pollard T. Electric car batteries: everything you need to know. Carmagazine. co. uk. 2020. Available: https://www.carmagazine.co.uk/electric/ev-car-battery-capacity-tech/

30. Marsh RA, Vukson S, Surampudi S, Ratnakumar BV, Smart MC, Manzo M, et al. Li-ion batteries for aerospace applications. J Power Sources. 2001;97–98: 25–27.

31. Bruce GC, Marcoux L. Large lithium ion batteries for aerospace and aircraft applications. Sixteenth Annual Battery Conference on Applications and Advances Proceedings of the Conference (Cat No01TH8533). 2001. pp. 147–151.

32. Haskew M, Hardy J. A Mini-Review of Shape-Memory Polymer-Based Materials:Stimuli-responsive shape-memory polymers. Johnson Matthey Technology Review. 2020;64. doi:10.1595/205651319x15754757916993

33. Mbeh DA, do Nascimento RO. Biocompatibility of shape-memory polymers for biomedical applications. Shape Memory Polymers for Biomedical Applications. 2015. pp. 77–95. doi:10.1016/b978-0-85709-698-2.00005-2

34. Xie T. Tunable polymer multi-shape memory effect. Nature. 2010;464: 267–270.

35. Shape memory medical, inc. In: Shape Memory Medical, Inc [Internet]. [cited 31 Jan 2022]. Available: https://www.shapemem.com/

36. Zhao Q, Qi HJ, Xie T. Recent progress in shape memory polymer: New behavior, enabling materials, and mechanistic understanding. Prog Polym Sci. 2015;49–50: 79–120.

37. Liu C, Qin H, Mather PT. Review of progress in shape-memory polymers. J Mater Chem. 2007;17: 1543–1558.

38. Lai H-Y, Wang H-Q, Lai J-C, Li C-H. A Self-Healing and Shape Memory Polymer that Functions at Body Temperature. Molecules. 2019;24. doi:10.3390/molecules24183224

39. Havens E, Snyder EA, Tong TH. Light-activated shape memory polymers and associated applications. Smart Structures and Materials 2005: Industrial and Commercial Applications of Smart Structures Technologies. SPIE; 2005. pp. 48–55.

40. Yuan Z, Muliana A, Rajagopal KR. Modeling the response of light-activated shape memory polymers. Math Mech Solids. 2017;22: 1116–1143.

41. Zhou G, Zhang H, Xu S, Gui X, Wei H, Leng J, et al. Fast Triggering of Shape Memory Polymers using an Embedded Carbon Nanotube Sponge Network. Sci Rep. 2016;6: 24148.

42. Gilbert HB, Webster RJ. Rapid, Reliable Shape Setting of Superelastic Nitinol for Prototyping Robots. IEEE Robotics and Automation Letters. 2016;1: 98–105.

43. Zhou J, Li H, Tian R, Dugnani R, Lu H, Chen Y, et al. Fabricating fast triggered electro-active shape memory graphite/silver nanowires/epoxy resin composite from polymer template. Sci Rep. 2017;7: 5535.

44. Luo H, Li Z, Yi G, Zu X, Wang H, Wang Y, et al. Electro-responsive silver nanowire-shape memory polymer composites. Mater Lett. 2014;134: 172–175.

45. Gong C, Liang J, Hu W, Niu X, Ma S, Thomas Hahn H, et al. A Healable, Semitransparent Silver Nanowire-Polymer Composite Conductor. Advanced Materials. 2013. pp. 4186–4191. doi:10.1002/adma.201301069

46. Sun J, Liu Y, Leng J. Mechanical properties of shape memory polymer composites enhanced by elastic fibers and their application in variable stiffness morphing skins. J Intell Mater Syst Struct. 2015;26: 2020–2027.

47. Lendlein A, Langer R. Biodegradable, elastic shape-memory polymers for potential biomedical applications. Science. 2002;296: 1673–1676.

48. Klinkmann H, Wolf H, Schmitt E. Definition of biocompatibility. Contrib Nephrol. 1984;37: 70–77.

49. Williams D. Revisiting the definition of biocompatibility. Med Device Technol. 2003;14: 10–13.

50. Metcalfe A, Desfaits A-C, Salazkin I, Yahia L, Sokolowski WM, Raymond J. Cold hibernated elastic memory foams for endovascular interventions. Biomaterials. 2003;24: 491–497.

51. Lendlein A, Behl M, Hiebl B, Wischke C. Shape-memory polymers as a technology platform for biomedical applications. Expert Rev Med Devices. 2010;7: 357–379.

52. De Nardo L, Alberti R, Cigada A, Yahia L, Tanzi MC, Farè S. Shape memory polymer foams for cerebral aneurysm reparation: effects of plasma sterilization on physical properties and cytocompatibility. Acta Biomater. 2009;5: 1508–1518.

53. Kai D, Tan MJ, Prabhakaran MP, Chan BQY, Liow SS, Ramakrishna S, et al. Biocompatible electrically conductive nanofibers from inorganic-organic shape memory polymers. Colloids Surf B Biointerfaces. 2016;148: 557–565.

54. Sabahi N, Chen W, Wang C-H, Kruzic JJ, Li X. A Review on Additive Manufacturing of Shape-Memory Materials for Biomedical Applications. JOM. 2020;72: 1229–1253.

55. Thomas DS, Gilbert SW, Others. Costs and cost effectiveness of additive manufacturing. NIST Spec Pub. 2014;1176: 12.

56. Mehrpouya M, Vahabi H, Janbaz S, Darafsheh A, Mazur TR, Ramakrishna S. 4D printing of shape memory polylactic acid (PLA). Polymer . 2021;230: 124080.

57. Lee J-Y, An J, Chua CK. Fundamentals and applications of 3D printing for novel materials. Applied Materials Today. 2017;7: 120–133.

58. Revilla-León M, Özcan M. Additive manufacturing technologies used for processing polymers: Current status and potential application in prosthetic dentistry. J Prosthodont. 2019;28: 146–158.

59. Business Wire. Services home. [cited 5 Feb 2022]. Available: https://services.businesswire.com/?hsLang=en

60. Hull CW. Apparatus for production of three-dimensional objects by stereolithography. United States Patent, Appl., No. 638905, Filed. 1984. Available: https://ci.nii.ac.jp/naid/10007148184/

61. Touri M, Kabirian F, Saadati M, Ramakrishna S, Mozafari M. Additive manufacturing of biomaterials − the evolution of rapid prototyping. Adv Eng Mater. 2019;21: 1800511.

62. Lille M, Nurmela A, Nordlund E, Metsä-Kortelainen S, Sozer N. Applicability of protein and fiber-rich food materials in extrusion-based 3D printing. J Food Eng. 2018;220: 20–27.

63. Trenfield SJ, Awad A, Goyanes A, Gaisford S, Basit AW. 3D Printing Pharmaceuticals: Drug Development to Frontline Care. Trends Pharmacol Sci. 2018;39: 440–451.

64. Trenfield SJ, Awad A, Madla CM, Hatton GB, Firth J, Goyanes A, et al. Shaping the future: recent advances of 3D printing in drug delivery and healthcare. Expert Opin Drug Deliv. 2019;16: 1081–1094.

65. Xu X, Awad A, Robles-Martinez P, Gaisford S, Goyanes A, Basit AW. Vat photopolymerization 3D printing for advanced drug delivery and medical device applications. J Control Release. 2021;329: 743–757.

66. Ehrmann G, Ehrmann A. 3D printing of shape memory polymers. J Appl Polym Sci. 2021;138: 50847.

67. Mohamed OA, Masood SH, Bhowmik JL. Optimization of fused deposition modeling process parameters for dimensional accuracy using I-optimality criterion. Measurement. 2016;81: 174–196.

68. The main differences between FFF and FDM explained. [cited 11 Feb 2022]. Available: https://www.3dprintingspot.com/post/the-main-differences-between-fff-and-fdm-explained

69. The history of 3D printing. In: MakerBot [Internet]. 19 Mar 2019 [cited 12 Feb 2022]. Available: https://www.makerbot.com/stories/engineering/history-of-3d-printing/

70. Masood SH. Advances in fused deposition modeling. 2014.

71. Chua CK, Leong KF. Rapid Prototyping: Principles And Applications In Manufacturing (With Cd-rom). World Scientific; 2000.

72. Walker JL, Santoro M. 9 - Processing and production of bioresorbable polymer scaffolds for tissue engineering. In: Perale G, Hilborn J, editors. Bioresorbable Polymers for Biomedical Applications. Woodhead Publishing; 2017. pp. 181–203.

73. Palermo E. Fused deposition modeling: most common 3d printing method. Livest Sci. 2013;19.

74. Singh R, Singh S, Hashmi MSJ. Implant materials and their processing technologies. 2016.

75. Yue C, Li M, Liu Y, Fang Y, Song Y, Xu M, et al. Three-dimensional printing of cellulose nanofibers reinforced PHB/PCL/Fe3O4 magneto-responsive shape memory polymer composites with excellent mechanical properties. Additive Manufacturing. 2021;46: 102146.

76. Wei H, Zhang Q, Yao Y, Liu L, Liu Y, Leng J. Direct-Write Fabrication of 4D Active Shape-Changing Structures Based on a Shape Memory Polymer and Its Nanocomposite. ACS Appl Mater Interfaces. 2017;9: 876–883.

77. Lewis NS, Nocera DG. Powering the planet: chemical challenges in solar energy utilization. Proc Natl Acad Sci U S A. 2006;103: 15729–15735.

78. Chen F, Duic N, Manuel Alves L, da Graça Carvalho M. Renewislands—Renewable energy solutions for islands. Renewable Sustainable Energy Rev. 2007;11: 1888–1902.

79. Dunn B, Kamath H, Tarascon J-M. Electrical energy storage for the grid: a battery of choices. Science. 2011;334: 928–935.

80. Energy storage. In: Clarke Energy [Internet]. 3 Jun 2020 [cited 11 Mar 2022]. Available: https://www.clarke-energy.com/energy-storage/

81. Garche J, Dyer C, Moseley PT, Ogumi Z, Rand D, Scrosati B. Encyclopedia of Electrochemical Power Sources. Newnes; 2013.

82. Arfwedson A. Untersuchung einiger bei der Eisen-Grube von Utö vorkommenden Fossilien und von einem darin gefundenen neuen feuerfesten Alkali. J Chem Phys. 1818;22: 93–117.

83. Brande WT. A Manual of Chemistry. J.W. Parker; 1841.

84. Lewis GN, Keyes FG. THE POTENTIAL OF THE LITHIUM ELECTRODE. J Am Chem Soc. 1913;35: 340–344.

85. Harris WS. Electrochemical Studies in Cyclic Esters. University of California Radiation Laboratory; 1958.

86. Meyers WF, Simmons JW. Electric current-producing cell with anhydrous organic liquid electrolyte. US Patent. 3423242, 1969. Available: https://patentimages.storage.googleapis.com/40/99/eb/3c98805f8c4cdb/US3423242.pdf

87. Goodenough JB. Battery Components, Active Materials for. In: Brodd RJ, editor. Batteries for Sustainability: Selected Entries from the Encyclopedia of Sustainability Science and Technology. New York, NY: Springer New York; 2013. pp. 51–92.

88. Holmes C. The Lithium/Iodine-Polyvinylpyridine Pacemaker Battery - 35 years of Successful Clinical Use. ECS Trans. 2007;6: 1.

89. Whittingham MS. Chalcogenide battery. US Patent 4,009,052. 1977. Available: https://patents.google.com/patent/US4009052A/en

90. Whittingham MS. Electrical energy storage and intercalation chemistry. Science. 1976;192: 1126–1127.

91. Yamauchi T, Mizushima K, Satoh Y, Yamada S. Development of a simulator for both property and safety of a lithium secondary battery. J Power Sources. 2004;136: 99–107.

92. Saleh MS, Li J, Park J, Panat R. 3D printed hierarchically-porous microlattice electrode materials for exceptionally high specific capacity and areal capacity lithium ion batteries. Additive Manufacturing. 2018;23: 70–78.

93. Bao Y, Liu Y, Kuang Y, Fang D, Li T. 3D-printed highly deformable electrodes for flexible lithium ion batteries. Energy Storage Materials. 2020;33: 55–61.

94. Ragones H, Menkin S, Kamir Y, Gladkikh A, Mukra T, Kosa G, et al. Towards smart free form-factor 3D printable batteries. Sustainable Energy & Fuels. 2018;2: 1542–1549.

95. What are the Advantages and Disadvantages of 3D Printing? [cited 16 Mar 2022]. Available: https://www.twi-global.com/technical-knowledge/faqs/what-is-3d-printing/pros-and-cons

96. Cheng M, Deivanayagam R, Shahbazian-Yassar R. 3D printing of electrochemical energy storage devices: A review of printing techniques and electrode/electrolyte architectures. Batter supercaps. 2020;3: 130–146.

97. Lyu Z, Lim GJH, Koh JJ, Li Y, Ma Y, Ding J, et al. Design and Manufacture of 3D-Printed Batteries. Joule. 2021;5: 89–114.

98. Zeng L, Li P, Yao Y, Niu B, Niu S, Xu B. Recent progresses of 3D printing technologies for structural energy storage devices. Materials Today Nano. 2020;12: 100094.

99. Benefits and disadvantages to 3D printing in manufacturing. In: SEACOMP [Internet]. [cited 17 Mar 2022]. Available: https://www.seacomp.com/resources/benefits-and-drawbacks-to-3d-printing-in-manufacturing

100. Chen C, Jiang J, He W, Lei W, Hao Q, Zhang X. 3D printed high-loading lithium-sulfur battery toward wearable energy storage. Adv Funct Mater. 2020;30: 1909469.

101. He W, Chen C, Jiang J, Chen Z, Liao H, Dou H, et al. 3D Printed Multilayer Graphite@SiO Structural Anode for High-Loading Lithium-Ion Battery. Batteries & Supercaps. 2022. doi:10.1002/batt.202100258

102. Cersoli T, Barnawi M, Johnson K, Burden E, Li F, MacDonald E, et al. 4D Printed Shape Memory Polymers: Morphology and Fabrication of a Functional Antenna. Recent Progress in Materials. 2022;4: 1–17.

103. Inverardi N, Pandini S, Bignotti F, Scalet G, Marconi S, Auricchio F. Sequential motion of 4D printed photopolymers with broad glass transition. Macromol Mater Eng. 2020;305: 1900370.

104. Shop. In: Working Ink [Internet]. [cited 23 Mar 2022]. Available: https://secure.workingink.co.uk/working-ink-shop/

105. Genesis Development Resin Base – liter. In: Tethon 3D | Ceramic Materials / 3d Printer [Internet]. 16 Nov 2016 [cited 24 Mar 2022]. Available: https://tethon3d.com/product/genesis/

106. 100g conductive Synthetic Graphite (TIMCAL TIMREX® KS6) powder for battery research. In: MSE Supplies LLC [Internet]. [cited 24 Mar 2022]. Available: https://www.msesupplies.com/products/100g-timcal-ks-6-conductive-graphite-powder-for-battery-research?variant=32213390819386

107. Lithium iron phosphate $LiFePO_4$ LFP cathode powder 500g. In: MSE Supplies LLC [Internet]. [cited 24 Mar 2022]. Available: https://www.msesupplies.com/products/lithium-iron-phosphate-lifepo4-powder-500g?variant=7127289092

108. Technical Info. In: The pioneer for Sheet Resistance / Resistivity Measurement NAPSON CORPORATION [Internet]. [cited 26 Mar 2022]. Available: https://en.napson.co.jp/technique/

109. Scanning electron microscope. [cited 3 Apr 2022]. Available: https://www.purdue.edu/ehps/rem/laboratory/equipment%20safety/Research%20Equipment/sem.html

110. Gibson LT. ARCHAEOMETRY AND ANTIQUE ANALYSIS | Metallic and Ceramic Objects. Encyclopedia of Analytical Science. 2005. pp. 117–123. doi:10.1016/b0-12-369397-7/00020-0

111. Schuster CE, Vangel MG, Schafft HA. Improved estimation of the resistivity of pure copper and electrical determination of thin copper film dimensions. Microelectron Reliab. 2001;41: 239–252.

112. Djodi H, Kartini E, Others. The improving conductivity of LiFePO4 by optimizing the calendaring process. IOP Conference Series: Materials Science and Engineering. IOP Publishing; 2018. p. 012059.

113. Elert G. Resistivity of carbon, graphite. [cited 18 Apr 2022]. Available: https://hypertextbook.com/facts/2004/AfricaBelgrave.shtml

114. Xiaoli Xi, Guanglei Chen, Zuoren Nie ∗, Shan He, Xiong Pi, Xiaoguang Zhu, Jianjian Zhu, Tieyong Zuo. Preparation and performance of LiFePO4and LiFePO4/C

cathodes by freeze-drying. Journal of Alloys and Compounds. Available: https://www.researchgate.net/publication/257359329_Preparation_and_performance_of_LiFePO4_and_LiFePO4C_cathodes_by_freeze-drying